Jagiellonian University
Faculty of Physics, Astronomy and Applied Computer Science

TOPOLOGICAL COLD ATOM MODELS IN OPTICAL LATTICES

Doctoral thesis prepared by
Krzysztof Biedroń

under the supervision of
Prof. Jakub Zakrzewski

Kraków, December 2018

Wydział Fizyki, Astronomii i Informatyki Stosowanej
Uniwersytet Jagielloński

Oświadczenie

Ja, niżej podpisany Krzysztof Biedroń (nr indeksu: 1052070), doktorant Wydziału Fizyki, Astronomii i Informatyki Stosowanej Uniwersytetu Jagiellońskiego oświadczam, że przedłożona przeze mnie rozprawa doktorska pt. „Topological cold atom models in optical lattices" jest oryginalna i przedstawia wyniki badań wykonanych przeze mnie osobiście, pod kierunkiem prof. dr hab. Jakuba Zakrzewskiego. Pracę napisałem samodzielnie.

Oświadczam, że moja rozprawa doktorska została opracowana zgodnie z Ustawą o prawie autorskim i prawach pokrewnych z dnia 4 lutego 1994 r. (Dziennik Ustaw 1994 nr 24 poz. 83 wraz z późniejszymi zmianami).

Jestem świadom, że niezgodność niniejszego oświadczenia z prawdą ujawniona w dowolnym czasie, niezależnie od skutków prawnych wynikających z ww. ustawy, może spowodować unieważnienie stopnia nabytego na podstawie tej rozprawy.

data	podpis doktoranta

Abstract

The aim of this thesis is the investigation of a few theoretical propositions of realizing various interesting topological states of matter using cold atomic systems. The topological order in quantum mechanics has been given much attention in the recent years as this concept, previously known mostly from the observation of the fractional quantum Hall effect, has been generalized for a broader range of physical systems, where it can manifest itself in the form of non-local topological invariants. The search for new topological models and their implementations is undertaken not only because it is an exciting opportunity to study unique quantum mechanical effects, but also because they may be useful in some emerging technologies, such as quantum computing. Optical lattices are naturally a popular choice for such considerations due to an ease with which they can be modified and fine-tuned. The present thesis fits in this general scheme, as it focuses on a proper numerical evaluation of selected topological lattice models, paying great attention to their experimental feasibility.

In a natural way the results presented here are related to other, earlier works. After Chapter 1 containing preliminaries introducing the reader into specific features of cold atom settings and the topological order, in consecutive chapters we give a short summary of the main results published in 3 research articles forming the main part of the thesis. Chapter 2 discusses a realization of the emergent Rice-Mele model in a one-dimensional optical lattice. This paradigmatic model has already been realized experimentally in I. Bloch group using different techniques. On the other hand, the proposition we consider benefits from the ease of formation of defects, which is a consequence of its emergent nature. Moving on to systems with interactions, Chapter 3 focuses on the one-dimensional extended Bose-Hubbard model for filling $\nu = 3/2$ and $U = 2V$, which for zero tunneling corresponds to the thin-torus limit of the topological system. We investigate whether this equivalence is still valid for non-negligible tunneling and take a closer look at the quantum phase transition in the system. Chapter 4 contains the analysis of the extended Bose-Hubbard model in the context of an experimentally plausible realization in a one-dimensional optical lattice of dipolar particles, with the emphasis on the topological Haldane insulator phase and on the pair-superfluid phenomena that arise as an effect of long-range interactions. The two appendices are technical and describe shortly the numerical tools used, namely the exact diagonalization and the density matrix renormalization group. Here the aim is to provide some useful, in the author's opinion, hints for the interested reader rather than a precise introduction to the techniques which are more comprehensively discussed already in the references given.

Streszczenie

Głównym tematem niniejszej rozprawy jest analiza kilku teoretycznych propozycji tego, jak zrealizować ciekawe topologiczne stany materii przy użyciu układów zimnych atomów. Dużo uwagi zostało w ostatnich latach poświęcone topologicznemu porządkowi, ponieważ to pojęcie, pierwotnie znane głównie z obserwacji ułamkowego efektu Halla, udało się uogólnić na szerszą klasę fizycznych układów, w których objawia się w postaci nielokalnych niezmienników topologicznych. Poszukiwania nowych topologicznych modeli i sposobów ich implementacji są podejmowanie nie tylko jako ekscytująca możliwość badania wyjątkowych efektów mechaniki kwantowej, ale także ze względu na korzyści z ich potencjalnego wykorzystania w pewnych nowo powstających technologiach, takich jak informatyka kwantowa. Sieci optyczne, dzięki łatwości i dokładności z jaką można je modyfikować, są często wykorzystywane w tego typu rozważaniach. W te działania wpisuje się też obecna rozprawa, jako że przedstawiona została tu analiza wybranych topologicznych modeli przy użyciu metod numerycznych, ze szczególnym naciskiem na określenie wykonalności eksperymentalnej realizacji tych modeli.

Wyniki tutaj przedstawione są naturalnie powiązane z pewnymi wcześniejszymi pracami. Po krótkim zapoznaniu czytelnika z charakterystyką układów zimnych atomów i pojęciem porządku topologicznego w rozdziale 1, kolejne rozdziały stanowią zwięzłe podsumowanie wyników 3 prac badawczych, na których oparta jest ta rozprawa. Rozdział 2 zawiera dyskusję na temat realizacji emergentnego modelu Rice'a-Melego w jednowymiarowej sieci optycznej. Ten szeroko znany model został już zrealizowany w grupie I. Blocha przy wykorzystaniu innej metody. Propozycja tutaj rozważana ma w odniesieniu do niej pewne zalety, takie jak ułatwione formowanie defektów sieci, co jest konsekwencją jej emergentnej natury. Przechodząc do oddziałujących układów, rozdział 3 skupia się na jednowymiarowym, rozszerzonym modelu Hubbarda dla wypełnienia $\nu = 3/2$ i $U = 2V$, który przy zerowym tunelowaniu odpowiada pewnemu topologicznego układowi w granicy cienkiego torusa. Sprawdzamy, czy ta równoważność jest spełniona także w przypadku niezaniedbywalnego tunelowania i przyglądamy się uważniej kwantowemu przejściu fazowemu, które jest obecne w tym układzie. Rozdział 4 przedstawia analizę rozszerzonego modelu Bosego-Hubbarda w kontekście eksperymentalnej realizacji w jednowymiarowej sieci optycznej zawierającej dipolowe cząstki, ze szczególnym uwzględnieniem topologicznej fazy izolatora Haldane'a i zjawiska superciekłości par, które są konsekwencją dalekozasięgowych oddziaływań. Dwa załączniki stanowią krótkie przedstawienie użytych w rozprawie metod numerycznych, czyli dokładnej diagonalizacji i grupy renormalizacji dla macierzy gęstości (ang. density matrix renormalization group). Celem tutaj jest jedynie krótkie zarysowanie kilku użytecznych, zdaniem autora, właściwości tych technik, bardziej szczegółową ich analizę można znaleźć w przytoczonych referencjach.

Acknowledgements

First of all, I would like to thank my advisor, Prof. Jakub Zakrzewski, for giving me the opportunity to work under his guidance. Without his invaluable help, finishing this thesis would not be possible. I would also like to thank all of my Colleagues in the Atomic Optics Department, whom I had the pleasure of metting during my doctoral work, and whose company was both enjoyable and scientifically enlightening. Special thanks go to Dr. Omjyoti Dutta, Dr. Tanja Đurić and Dr. Mateusz Łącki, whose work has been indispensable in the research I have been a part of. I am also grateful to my dear Agnieszka and all of my Friends, as well as my Parents and the rest of my family for the constant support they have been giving me. The work was supported by Polish National Science Centre (Grant No. DEC-2012/04/A/ST2/00088 and Grant No. 2015/19/B/ST2/01028) and by PL-Grid Infrastructure.

Contents

Chapter 1

Preliminaries

1.1 Optical lattices

The theoretical physics rarely stops and waits for its experimental counterpart to catch up. With an ever-growing number of physicists trying to explain every bit of universe's inner workings, devising new ways of examining and constraining these theories became a job of an utmost importance. At the same time, the field of atomic physics saw great progress in areas of developing sophisticated techniques of cooling dilute atomic gases and constructing lasers, bringing unprecedented control of physical systems, allowing not only precise measurements of fundamental constants, but also engineering complex interacting systems which realize given theoretical models with great precision.

These two independent developments naturally aligned with each other actualizing the idea of quantum simulators, proposed by Richard Feynman [22] — to use carefully assembled quantum systems in order to simulate physics, which are otherwise hard to observe. The examples of which include various tight-binding models, lattice models with enormous magnetic fields and, more recently, even quantum chromodynamics and other gauge theories. One particular area of physics that benefited greatly from this kind of simulations is the field of topological insulators, which is the topic of Sec. 1.3. In this section I will present the main ideas behind using ultra cold-atoms as quantum simulators with a focus on optical lattice settings.

1.1.1 Atom-light interactions

The study of lattices has always been inseparably connected with solid state physics. Recent advances in atom cooling and trapping, however, brought them into experimental spotlight in the field of atomic, molecular and optical (AMO) physics. Using carefully set up lasers and atoms cooled to temperatures near absolute zero, different kinds of possible artificial lattices are being explored, collectively known as optical lattices. The main ingredient is the laser light [with intensity $I(\mathbf{r})$] acting on the atoms with the dipole force: [29]

$$\mathbf{F}(\mathbf{r}) = \frac{1}{2\varepsilon_0 c}\mathrm{Re}(\alpha)\nabla I(\mathbf{r}). \tag{1.1}$$

The polarizability of the atoms, α, which depends on both the frequency of the laser ω and the resonant frequency in the model ω_0, can be derived using a simplified two-level model

and the rotating wave approximation. In the regime of small detuning, $\Delta = \omega - \omega_0 \ll w_0$, and even smaller excited state decay rate, $\Gamma \ll \Delta$, the effective potential and the scattering length of the excited state are given by: [29]

$$V(\mathbf{r}) = \frac{3\pi c^2}{2\omega_0^3}\frac{\Gamma}{\Delta}I(\mathbf{r}), \qquad (1.2) \qquad \Gamma_{sc}(\mathbf{r}) = \frac{\Gamma}{\hbar\Delta}U(\mathbf{r}). \qquad (1.3)$$

Because $U(\mathbf{r}) \sim I(\mathbf{r})\Delta^{-1}$ and $\Gamma_{sc}(\mathbf{r}) \sim I(\mathbf{r})\Delta^{-2}$, it is possible to reduce the effects of the scattering by having large detuning and high laser light intensity. Furthermore, there are two classes of trapping potentials, depending on the sign of Δ: atoms are drawn to either maxima ($\Delta < 0$, red detuning) or minima ($\Delta > 0$, blue detuning) of the light intensity.

1.1.2 Laser light geometry

In the following description, it is assumed that a single laser beam of a total power P has a Gaussian profile with a width $w(z)$ that increases with the distance from the beam focal point (z): [29]

$$I(r,z) = \frac{2P}{\pi w^2(z)}e^{-2r^2/w^2(z)}. \qquad (1.4)$$

The beam divergence function is $w(z) = w_0\sqrt{1 + z^2/z_R^2}$ and so in the vicinity of the focus both r and z dependence be approximated by a quadratic function. Typical value of w_0 is around 100 μm, while z_R ranges between millimeters and centimeters. [13]

Two overlapping counter-propagating laser beams of the same wavelength ($k = 2\pi/\lambda$) and intensity produce periodic potential:

$$V(r,z) = -V_0 e^{-2r^2/w^2(z)} sin^2(kz), \qquad (1.5)$$

where the value of V_0 can be found by using (1.2) and (1.4). The potential (1.5) is a lattice of planes (constrained by the beam profile) with a lattice constant $a = \pi/k = \lambda/2$. Adding additional pairs of counter-propagating lasers in perpendicular directions leads to more refined systems: 2D array of potential tubes (in the case of 2 laser pairs) and 3D lattice of well-localized potential wells (in the case of 3 laser pairs). The last example is of particular interest in relation to this work, as it allows creating effective 1D, 2D or 3D synthetic lattices, depending on the depths of the lattice potential in each of the directions (as high potential barrier between neighboring wells effectively restricts the movement in that direction).

1.2 Bose-Hubbard model

Exact description of a physical system containing a large number of interacting particles, even if they are confined to a regular lattice, is a problem that lacks an analytical solution except for a few special cases. In order to get a valuable insight into the behavior of such systems, some kind of simplification is needed. For the lattice systems it is usually done through tight-binding approximation, where one introduces an effective cutoff for the interaction length, allowing only particles which are close to each other to affect each other. [6] This simple idea is a basis of multiple models, amongst which is the Bose-Hubbard model (BHM).

1.2.1 Basic model

Hamiltonian of BHM has the form:

$$\hat{H} = -t \sum_{\langle i,j \rangle} \hat{b}_i^\dagger b_j + \frac{U}{2} \sum_i \hat{n}_i(\hat{n}_i - 1) - \mu \sum_i \hat{n}_i, \tag{1.6}$$

where the parameters are: t – the tunneling between the nearest neighbors, U – the interaction between two particles residing on the same site and μ – the chemical potential, while $\hat{b}_i$ is the creation operator for a particle at site i, $\hat{n}_i = \hat{b}_i^\dagger \hat{b}_i$ is the corresponding number of particles operator and $\langle i,j \rangle$ denotes a sum over the nearest neighbors. The main feature of the model is the celebrated superfluid (SF) to Mott insulator (MI) quantum phase transition [23], where the ground state of the system changes from the extended, highly correlated state (SF) to the one with a fixed number of isolated particles localized on each site of the lattice (MI).

This simple model is commonly used to describe a behavior of ultracold particles trapped inside an optical lattice (one of the most famous, early examples of this correspondence is the observation of SF to MI transition [26] in a lattice of ^{87}Rb atoms). In such systems the BHM arises naturally from the general, many-body Hamiltonian in its second quantization form:

$$\hat{H} = \int d\mathbf{r}\, \hat{\Psi}(\mathbf{r})^\dagger \left(-\frac{\hbar^2}{2m}\nabla^2 + V_{\text{ext}} \right) \hat{\Psi}(\mathbf{r}) + \frac{1}{2} \int d\mathbf{r}\, d\mathbf{r}' \hat{\Psi}^\dagger(\mathbf{r}) \hat{\Psi}^\dagger(\mathbf{r}) V(\mathbf{r} - \mathbf{r}') \hat{\Psi}(\mathbf{r}) \hat{\Psi}(\mathbf{r}) \tag{1.7}$$

after taking into account few reasonable assumptions [V_{ext} is the trapping potential, in the form of Gaussian envelope of (1.5)]. First, since the optical lattice potential is periodic, one can describe the field operators ($\hat{\psi}$) using orthogonal Bloch functions $\varphi_{\alpha,k}(\mathbf{r})$ (with α being a band number and k being quasi-momentum). For deep lattices the separation between the lowest and the first excited band is large and so it is enough to consider only the lowest band, $\alpha = 0$, provided that the temperature is sufficiently low. In such cases it is convenient to use Wannier functions as the basis, giving the field operators the form:

$$\hat{\Psi}(\mathbf{r}) = \sum_i \hat{b}_i w_i(\mathbf{r}). \tag{1.8}$$

Inserting (1.8) into (1.6) gives:

$$\hat{H} = -\sum_{i \neq j} t_{i,j} \hat{b}_i^\dagger \hat{b}_j + \sum_{i,j,k,l} \frac{U_{ijkl}}{2} \hat{b}_i^\dagger \hat{b}_j^\dagger \hat{b}_k \hat{b}_l - \sum_i \epsilon_i n_i, \tag{1.9}$$

where:

$$t_{i,j} = \int d\mathbf{r}\, w_i^*(\mathbf{r}) \left(-\frac{\hbar^2}{2m}\nabla^2 + V_{\text{ext}} \right) w_j(\mathbf{r}), \tag{1.10}$$

$$U_{i,j,k,l} = \int d\mathbf{r}\, d\mathbf{r}'\, w_i^*(\mathbf{r}) w_j^*(\mathbf{r}') V(\mathbf{r} - \mathbf{r}') w_k(\mathbf{r}) w_l(\mathbf{r}'). \tag{1.11}$$

$$\epsilon_i = \int d\mathbf{r}\, |w_i(\mathbf{r})|^2 V_{\text{ext}}. \tag{1.12}$$

From (1.10) one can recover $t_{i,i+1} = t_{i+1,i} = t$ (for isotropic potential and while approximating $V_{\text{ext}} \approx$ const in the middle of the trap) and set $t_{i,j} \approx 0$ for $|i - j| > 1$ (which is

justifiable for deep enough lattices). As for (1.11), in cold, neutral atoms it is usually enough to consider only the short-range s-wave scattering, which, provided that Ψ is not singular, has the form: [13]

$$V(\mathbf{r}-\mathbf{r}') = \frac{4\pi\hbar^2 a_s}{m}\delta(\mathbf{r}-\mathbf{r}') = g\delta(\mathbf{r}-\mathbf{r}'), \tag{1.13}$$

where a_s is the scattering length. With this assumption the only non-zero term arising from the interactions is $U_{iiii} = U$. The only thing needed to recover (1.6) is the addition of a chemical potential μ, which is a standard procedure when describing system in the grand canonical ensemble. This results in term $\mu_i\hat{n}_i = (\mu + \epsilon_i)\hat{n}_i$, unless one again chooses to ignore the edges of the trap, in which case $\epsilon_i = \epsilon$ can be incorporated into chemical potential: $\mu + \epsilon \to \mu$, giving (1.6) as a result.

Working with an optical lattice it is straightforward to manipulate relative strengths of tunneling and interactions, t/U, as increasing the lattice depth drastically reduces t, while at the same time brings atoms residing on the same lattice sites closer (narrowing their Wannier functions), amplifying U [41]. Another popular method of modifying parameters of (1.6) employs so called Feshbach resonances — coupling of atoms' scattering state to higher energy molecular bound states through a magnetic field — which can modify effective a_s for atoms to the point of nullifying it or changing its sign [15].

1.2.2 Extended Bose Hubbard model

While standard BHM is a great tool to analyze simple optical lattices, there are many lattice arrangements which require us to go beyond this simple approximation. Probably the most notable such case are lattices filled with dipolar atoms, where interactions decay with distance as r^{-3}[48]:

$$V_{\text{dipole}}(\mathbf{r}) = \frac{C_{\text{dipole}}}{4\pi}\frac{1-3\cos^2\theta}{r^3}. \tag{1.14}$$

Here, C_{dipole} is equal to $\mu_0\mu^2$ for particles with magnetic dipole moment μ and μ_e^2/ε_0 for particles with electric dipole moment ε_0, while θ is the angle between $\mathbf{r}$ and the polarization direction. Experiments with multiple species of dipolar particles have been done in recent years, with a clear progress towards atoms possessing larger dipole momenta [2, 16, 28, 49], while also demonstrating the possibility of tuning the contact interactions in such systems using Feshbach resonances [50].

Due to long range interactions introduced through (1.14), an dditional term resulting from (1.11), namely $V = U_{i(i+1)i(i+1)} + U_{i(i+1)(i+1)i}$, needs to be added to the Hamiltonian (1.6), resulting in:

$$\hat{H} = -\sum_{\langle i,j\rangle} t\hat{b}_i^\dagger b_j + V\sum_{\langle i,j\rangle} n_i n_j + \frac{U}{2}\sum_i \hat{n}_i(\hat{n}_i - 1) - \mu\sum_i \hat{n}_i. \tag{1.15}$$

The Hamiltonian (1.15) is commonly referred to as the extended Bose-Hubbard model (EBHM) and has been a topic of numerous theoretical [57, 59] and some preliminary experimental [8] works.

Introducing nearest neighbor interaction, V, enriches the phase diagram by multiple phases. For large values of V, the system finds itself in checkerboard/density wave (DW) phases, which are insulating phases characterized by a specific pattern of particle density (for

every two nearest neighboring sites, one of them is empty and the other one is filled). For intermediate values of V a peculiar insulating phase called Haldane insulator (HI) manifests[17]. It is analogous to Haldane phase introduced for spin-1 Heisenberg chains [32, 34] and is notable for being a symmetry protected topological state [31] (see also Sec. 1.3). Based on numerical calculations the existence of yet another class of supersolid phases (where both superfluid and density wave order coexist) has been postulated [9, 59].

1.2.3 Further extensions

If the assumptions used to derive BHM and EBHM are even more relaxed, the Hamiltonian of an optical lattice gains additional terms, which come mostly from the inclusion of next biggest (1.11) interactions. Most prominent of those are density-dependent (density-induced) tunnelings [$T = -0.5(V_{ii(i+1)i} + V_{iii(i+1)})$] and pair tunnelings ($P = 0.5V_{iijj}$) [21]:

$$\hat{H} = -\sum_{\langle i,j\rangle} t\,\hat{b}_i^\dagger b_j + \frac{V}{2}\sum_{\langle i,j\rangle} n_i n_j + \frac{U}{2}\sum_i \hat{n}_i(\hat{n}_i - 1) - T\sum_{\langle i,j\rangle} b_i^\dagger(\hat{n}_j + \hat{n}_j)\hat{b}_j + P\sum_{\langle i,j\rangle} \hat{b}_i^{\dagger 2}\hat{b}_j^2 - \mu\sum_i \hat{n}_i. \quad (1.16)$$

Since these terms are generally much smaller than the ones present in BHM the main effects of their presence in (1.16) is a shift of phase boundaries, most noticeable in systems with high densities (large μ). It is however expected that in the future it will be possible to engineer systems with comparably large values of V, T and P with respect to t and U (enabled by trapping particles with large dipole momenta and/or precise arrangement of lattice geometry) in which case many more exotic phases, e.g. phases manifesting pair-superfluidity, are expected to be found therein [63].

1.3 Topological phenomena in quantum systems

Present-day theory of topological insulators arose as an aftermath of the experimental observation of integer [44] and fractional quantum Hall effect [67] (IQH and FQH respectively). These inherently many-body phenomena manifest in (effectively) two-dimensional electronic system subject to large magnetic fields (of the order of a few teslas) and lead to an exact quantization of a resulting Hall conductivity in a measured samples. While enlightening phenomenological descriptions of electron wavefunction in such systems were quickly presented (most notably by Laughlin [47]), recently these effects are viewed upon in the context of much broader classification of topological systems [65, 71]. These systems are characterized by particle-like excitations, which are nevertheless resistant to local perturbations and depend only on global invariants, which are topological in nature. These properties make them promising candidates for quantum computation, as they can help circumvent one of the biggest problems of conventional quantum computers, i.e. the decoherence due to the interactions with the environment, which leads to unaccounted errors (correcting this errors requires a tremendous effort for typical quantum computer realizations).

1.3.1 Berry phase and Chern numbers

The phase of a complex quantum mechanical wavefunction, whose evolution in time is determined by the Schrödinger equation, is a key ingredient in understanding some of the most strikingly non-classical quantum effects, such as the double-slit experiment [19] and Anderson localization [4]. If a system being studied is isolated from the outside world, the phase has no bearing on the physical state and is thus arbitrary. With that said, it may come as a surprise that a system evolving over a closed (that is, having the same initial and final state) path C may acquire a nontrivial phase factor, which depends only on the topology of a related Hilbert space. This geometric phase, observed already in the 1950s by Aharonov and Bohm [1], is known as Berry phase [10] and can be calculated as (if the evolution is over some parameter called ϕ):

$$\gamma(C) = -i \int_C \langle \psi(\phi) | \nabla_\phi | \psi(\phi) \rangle \, d\phi \equiv \int_C \mathbf{A}(\phi) d\phi, \tag{1.17}$$

where $\mathbf{A}$ is called Berry connection. (1.17) can be expressed as a surface integral of a Berry flux: $\mathbf{F} = \nabla \times \mathbf{A}$. In two-dimensional spaces the integral of $\mathbf{F}$ over the whole space Ω_ϕ gives another topological invariant called the first Chern number:

$$C = \frac{1}{2\pi} \int_{\Omega_\phi} \mathbf{F} d^2\phi, \tag{1.18}$$

which must necessarily be an integer [35].

1.3.2 Simple one-dimensional topological models

Simple models in one dimension provide a great way to illustrate the basic notions of topological order in quantum systems. One of such models is the spinless fermion Rice-Mele model:

$$H = -\sum_{j=1}^{N} \left(t_1 c_j^\dagger d_j + t_2 c_j^\dagger d_{j-1} + \text{h.c.} \right) + \Delta \sum_{j=1}^{N} (c_j^\dagger c_j - d_j^\dagger d_j) \tag{1.19}$$

where $c_i^\dagger$ ($d_i^\dagger$) are the creation operators on odd (even) sites of the lattice. Su-Schrieffer-Heeger (SSH) model is a special case of (1.19) with Δ set to 0. In SSH case, we can rewrite (1.19) in momentum space as $H = \sum_k \psi_k^\dagger H_k \psi_k$ where H_k is a 2×2, getting as a result [7]:

$$\mathbf{u}_{\mp,k} = \frac{1}{\sqrt{2}} \begin{pmatrix} \pm 1 \\ e^{-i\theta_k} \end{pmatrix}, \tag{1.20}$$

where $t_1 e^{ika/2} + t_2 e^{-ika/2} = |\varepsilon_k| e^{i\theta_k}$ and a is a lattice constant. Calculating Zak phase (Berry phase over whole 1D Brillouin zone) [75] gives two different results depending on whether $t_1 > t_2$ (D1 configuration) or $t_1 < t_2$ (D2 configuration), which, while not being uniquely defined, are related by a topological invariant:

$$\phi_{\text{Zak}}^{\text{D1}} - \phi_{\text{Zak}}^{\text{D2}} = \pi \tag{1.21}$$

The existence of such invariant tells us that these two configurations are topologically different and there must exist a topological critical point where their energies are degenerated ($t_1 = t_2$). This property is universal for all topological phases and leads to the presence of localized edge states on the boundaries between topologically non-equal phases [36]. As these edge states are linked to intrinsic properties of the topological phase, they survive in the presence of local disturbances.

1.3.3 Anyon statistics

While models similar to the ones presented in Subsection 1.3.2 are expected to allow formation of quasiparticles behaving as Majorana fermions [25, 43] (sought after as an essential step towards topological quantum computation), they are not enough to construct a universal quantum computer. In order to fulfill that task more robust quasiparticles are needed [42]. It turns out that the class of particles behaving in an appropriate way behave neither as bosons nor fermions, and are collectively called anyons.

Both bosonic and fermionic behavior result from two simple facts — first, in three dimensions, the path of wrapping one particle all the way around the other can be continuously deformed to a trivial transformation, where both particles do not move at all and second, exchanging the positions of the identical particles only once may only lead to a change of phase (as the particles are indistinguishable). This reasoning however does not apply to two-dimensional systems, like a sample in a large magnetic field in FQH effect, and indeed some of the observations are believed (yet without the definitive proof) to be explained by anyonic excitations.

Apart from "trivial" anyons, which upon winding of one anyon around the other provide a change of phase, there exist more sophisticated particles called non-Abelian anyons. The name comes from the fact that the result of braiding (exchanging the positions of) pairs of such particles depends on the order of these operations. In order for anyons to be non-Abelian there has to exist a degenerate energy manifold in which those states live [52]. In such a case the Berry phase is not enough to describe the evolution of the state, which is governed by a matrix, $\psi_a \to M_{ab}\psi_b$, such that:

$$M_{ab} = \mathcal{P}e^{i\int d\mathbf{R}\cdot\mathbf{m}}, \quad \mathbf{m}_{ab} = \langle\psi_a(\mathbf{R})|\nabla_{\mathbf{R}}|\psi_b(\mathbf{R})\rangle, \tag{1.22}$$

where $\mathcal{P}$ stands for path ordering. The anyons present in such a system can be labeled (ϕ_i) based on a set of properties related to braiding. The behavior of two quasiparticles brought close to each other may either produce a single quasiparticle (or a lack thereof in case they were each other's antiparticle) or a nontrivial final state being a superposition of multiple quasiparticles. The equations governing the results of bringing quasiparticles together are called fusion rules:

$$\phi_a \times \phi_b = \sum_c N_{ab}^c \phi_c. \tag{1.23}$$

To fully characterize a non-Abelian anyonic system it is also necessary to provide the F-matrix (F_l^{ijk}) and R-matrix (R_c^{ab}) which relate different orders of braiding with each other and are themselves subject to the so called pentagon and hexagon identities [52, 66].

1.3.4 Fibonacci Anyons

In the case of Fibonacci anyons there are two particle types: $\mathbf{1}$ and τ, characterized by the fusion rules: $\mathbf{1}\otimes\mathbf{1} = \mathbf{1}$, $\mathbf{1}\otimes\tau = \tau$, $\tau\otimes\mathbf{1} = \tau$, $\tau\otimes\tau = \mathbf{1}\oplus\tau$, which correspond to $N_{11}^1 = N_{1\tau}^\tau = N_{\tau 1}^\tau = N_{\tau\tau}^1 = N_{\tau\tau}^\tau = 1$ with the rest $N_{ab}^c = 0$. The name comes from the dependence of the dimension of the fusion Hilbert space $\mathcal{M}_{(n)}$ on the number of fused particles n, which follows Fibonacci series: $\dim \mathcal{M}_{(n)} = F_{n-1}$, where $F_0 = 0$, $F_1 = 1$ and $F_i = F_{i-1} + F_{i-2}$.

The significance of this type of non-Abelian anyons is related to the fact that not only are they enough to construct a universal quantum computer [24], but they have been postulated

to explain already observed FQH effect at filling $\nu = \frac{12}{5}$ [61]. Fibonacci anyons were also related to the low tunneling limit of BH model with $\nu = \frac{3}{2}$ filling [5], which may point to a possible realization of such physics in optical lattices [20].

1.4 Quantum phase transitions

The phase of a classical system is characterized by a specific macroscopic order parameter and depends on its temperature, T, or some other intensive property. One of the biggest achievement of modern physics was the development of the phase transition theory (first proposed by Landau), which allowed a categorization of phase transitions into a set of classes of similarities, depending on how various parameters scale with the distance from the critical temperature, $T - T_c$ (or other parameter driving the transition).

Similar concept exists in quantum mechanics, quantum phase transitions (QPT) however are defined for a ground state at $T = 0$ and the transitions between different phases correspond to either an actual or an avoided level crossing in the lowest states' energies[58]. As in the classical theory, QPTs fall into few categories, each of which defines a specific critical behavior observable in the vicinity of the transition.

The following sections contain descriptions of a few physical quantities which are commonly used to differentiate between quantum phases and detect QPTs in bosonic optical lattice systems.

1.4.1 Fidelity

QPTs usually involve a dramatic change of some order in the ground state of the physical system. It is therefore possible to think of a simple quantity which measures such changes without relying on the specific details of the phases involved. One such measure is the fidelity, a term coming from the field of quantum information, which is simply an overlap between the two wavefunctions. In case of a QPT, one can select a parameter driving said transition (denoted g here), and define the ground state fidelity related to changes in that parameter [76]:

$$F(g, \delta) = |\langle \Psi_0(g - \delta/2) | \Psi_0(g + \delta/2) \rangle|. \tag{1.24}$$

(Note that some authors choose to use square of the modulus in the definition of the fidelity). Here, $\psi_0(g)$ is the ground state of the system for the parameter value g.

The most important feature that may be identified here is whether the ground state undergoes a gradual change, or there is an energy level crossing at the critical parameter value (g_c). In the second case, the fidelity will be close to 0 near the transition point regardless of the system size or other considerations and the discussion that follows assumes that this is not the case

While studying thermodynamical properties of the system, the limit of $N \to \infty$ (where N is the lattice size) is taken, however in that limit the value of F goes to 0 regardless of the values of g and δ (Anderson orthogonality catastrophe). It is therefore useful to consider other limiting behavior first, $\delta \to 0$, as we can expand F in Taylor series with respect to δ to its first nonzero-term [18, 74]:

$$F \approx 1 - \chi_F \frac{\delta^2}{2}. \tag{1.25}$$

(Linear term must vanish because of the ground state normalization, which ensures that $F \leq 1$). The prefactor χ_F, called fidelity susceptibility, provides a valuable insight into the nature of the phase transition without being dependent on the value of δ. χ_F scaling with respect to $|g - g_c|$ and N has been shown to follow certain relations including the critical exponent of the transition (ν) [30].

1.4.2 Correlation functions

Having an order parameter dependent on space and/or time [$\phi(\mathbf{r}, t)$], one can define a correlation function as:

$$C_\phi(\mathbf{r}, \mathbf{r}', t, t') = \langle \phi(\mathbf{r}, t)\phi(\mathbf{r}', t') \rangle . \tag{1.26}$$

Away from a criticality, the spatial part of these correlations typically follow an exponential law [58]:

$$C_\phi(\mathbf{r}, \mathbf{r}') \propto \exp(|\mathbf{r} - \mathbf{r}'|/\xi), \tag{1.27}$$

where ξ is a characteristic correlation length.

Inside a critical region on the other hand, in thermodynamical limit the value of $\xi \to \infty$, and instead of (1.27) there is a power law:

$$C_\phi(\mathbf{r}, \mathbf{r}') \propto |r|^{-K/2}, \tag{1.28}$$

where the value of K is dependent on the universality class of the transition/phase. For example, the values of K are well known for a transitions between superfluid and isolating phases in one-dimensional bosonic and fermionic chains [33], such as QPT between MI and SF phases and between DW and SF phases [46].

1.4.3 Structure factor

In condensed matter physics, the (static) structure factor is an essential tool in analyzing the spatial structure of a material, as it is manifested through scattering patterns obtained by bombarding a sample with X-ray radiation or neutrons/electrons. In the field of QPT and quantum topology, the structure factor is used as a characterization of a phase, which breaks translational invariance, most notably charge density wave (CDW) or other density wave (DW) phases. The precise definition of the structure factor for the one-dimensional lattice of length L and with N particles has the form:

$$S(q) = \frac{1}{N} \sum_{j,k=1}^{L} \langle \hat{n}_j \hat{n}_k \rangle \, e^{-iq(j-k)}, \tag{1.29}$$

where $\hat{n}_i$ is the particle density at i^{th} site. As such, it can be regarded as a Fourier transform of density correlations.

If a phase exhibits a regular spatial modulation, then $S(q)$ has a local maximum for q corresponding to a given symmetry. As an example, state $|X0X0...\rangle$ (with $X = \frac{N}{2L}$, i^{th} number corresponds to occupation of i^{th} site here), having $\mathbb{Z}_2$ symmetry, has a maximum for $q = \pi$.

1.4.4 Entanglement entropy and central charge

Entanglement entropy (EE) is a measure of entanglement of a given quantum state and as such has no equivalent in classical physics. The definition requires a division of a system into two separated parts (A and B), such that the total Hilbert space of the system can be expressed as their product: $\mathcal{H} = \mathcal{H}_A \otimes \mathcal{H}_B$. The state can be in general represented by a density matrix ρ (which for a pure state is $\rho = |\psi\rangle\langle\psi|$). The reduced density matrix of ρ in subsystem A is defined as the result of the partial trace over B: $\psi_A = \mathrm{tr}_B\,\rho$ (where partial trace is defined as $\mathrm{tr}_B = \sum_{i=0}^{\dim\mathcal{H}_B} \langle\psi_i^B|\,\rho\,|\psi_i^B\rangle$, where $|\psi_i^B\rangle$ is i^{th} state from a basis spanning $\mathcal{H}_B$). EE is then defined as von Neumann entropy of a reduced density matrix:

$$S_A = -\,\mathrm{tr}\,\rho_A \log \rho_A. \tag{1.30}$$

As a measure of how much entanglement there is between two different subsystems, S_A is important for quantum information and computing perspective [69], but also for characterizing different highly correlated many body states [70] and for optimizing numerical simulations' performance and applicability [54]. There is a rather famous result coming from conformal field theory in 1+1 dimensions, for which case conformal transformations (i.e., the one that preserves the angles) map to all holomorphic (and anti-holomorphic) functions. For a 1D chain of the length L in the vicinity of a QPT (or, more generally, in any critical region), EE of the subsystem of length l is [38]:

$$S_L(l) = \frac{c}{3} \ln\left[\frac{L}{\pi}\sin\left(\frac{\pi l}{L}\right)\right] + s, \tag{1.31}$$

where s is some non-universal constant, and c is called the central charge. The value of c is a characteristic, universal constant that can be associated with a specific type of QPT. For example, for a system in a superfluid phase the value of the central charge is $c = 1$ [14].

Chapter 2

Emergent Rice-Mele model in a one-dimensional lattice

2.1 Introduction

2.1.1 Topological defects in optical lattices

As has been already mentioned in Sec. 1.3, systems able to accommodate non-trivial topological states are thought to be well suited candidates for engineering a reliable quantum computer. On the interface between two topologically distinct regions there must necessarily exist edge states, which are exponentially confined to said interface — and as the topological regions are protected by non-local topological invariants, they are resilient with respect to local perturbations. This is in a stark contrast to a typical quantum computer architecture, where the interactions with the environment quickly destroy the coherence, leading to errors propagating throughout computations and necessitating the use of a large redundancy in the form of quantum error correction codes. The edge states can be anyonic in nature (see Subsec. 1.3.3) which means that physically rearranging them can provide all the basic operations needed for quantum computation.

Using lattice shaking and two strongly interacting fermionic species (denoted as $\uparrow$ and $\downarrow$) it is possible to engineer an effective Rice-Mele model hosting topological edge states [56]. While some preliminary numerical results were presented in the original work, in this chapter a more thorough and precise (albeit constrained to a small system sizes) exact diagonalization (see App. A) treatment of the proposed system is presented, following the paper [11] reproduced in this thesis.

2.1.2 The system

The system Hamiltonian, in terms of composite bosons (pairs of different fermionic species, bound by their interaction) and leftover majority $\downarrow$ fermions (for each $\uparrow$ fermion there is more

than one ↓ fermion), has the form:

$$\begin{aligned}\hat{H} =&\widetilde{T}_{01}^{-}\sum_{i=1}^{N}(\hat{p}_i^\dagger \hat{n}_i^c \hat{s}_{i+1} + \text{h.c.}) - \widetilde{T}_{01}^{+}\sum_{i=1}^{N}(\hat{p}_i^\dagger \hat{n}_i^c \hat{s}_{i-1} + \text{h.c.})\\ &+ (2\widetilde{T}_0 - \tilde{J}_0)\sum_{i=1}^{N}(\hat{c}_i^\dagger \hat{s}_{i+1}^\dagger \hat{c}_{i+1}\hat{s}_i + \text{h.c.}) + (2\widetilde{T}_1 + \tilde{J}_1)\sum_{i=1}^{N}(\hat{p}_i^\dagger \hat{n}_i^c \hat{n}_{i+1}^c \hat{p}_{i+1} + \text{h.c})\\ &- \tilde{J}_0\sum_{i=1}^{N}\hat{s}_i^\dagger \hat{s}_{i+1} + \Delta\sum_{i=1}^{N}\hat{n}_i^p,\end{aligned} \tag{2.1}$$

where $\hat{c}_i, \hat{c}_i^\dagger, \hat{n}_i^c$ are composite annihilation, creation and number operators at i^{th} site, while $\hat{s}_i(\hat{s}_i^\dagger)$ and $\hat{p}_i(\hat{p}_i^\dagger)$ are ↓ fermion ground state (s) and first excited state (p) creation (annihilation) operators, and $\hat{n}_i^p$ is the number operator of ↓ fermions in p state. The shaking lasers frequency is chosen to be almost resonant with respect to the difference between p level energy and interactions with a small detuning Δ.

The tunnelings in (2.1) are changed (from their standard, non-tilde values) by the shaking such that:

$$\tilde{J}_l = \mathcal{J}_0(\widetilde{K})J_l, \quad \widetilde{T}_l = \mathcal{J}_0(\widetilde{K})T_l, \quad \widetilde{T}_{01}^{\pm} = \mathcal{J}_N(A^{\pm}/\omega)\,T_{01}, \tag{2.2}$$

where $A^{\pm} = \sqrt{(K \pm \delta E_1 \cos\varphi)^2 + K^2 \sin^2\varphi}$, φ is the phase shift between the horizontal shaking (of strength K) and the amplitude oscillatory changes (both of frequency ω), $\widetilde{K} = K/\omega$ and $\mathcal{J}_N$ is the N-th order Bessel function of the first kind. N comes from an almost resonant condition, $U_1 + E_1 = N\omega + \Delta$, where E_1 is the energy of the p state and U_1 is the energy of the interactions between p state ↓ fermions and ↑ fermions. N is set to 1 for the rest of the chapter.

2.2 Resonant case

In this subsection the condition $\Delta = 0$ is assumed and the system of length L is half-filled with both the composites and the leftover fermions (that is, the average fillings are: $n_c = n_\downarrow = \frac{1}{2}$). The system is assumed to have periodic boundary conditions (PBC) imposed and $\widetilde{K}$ is limited to $\widetilde{K} < \widetilde{K}_c \approx 2.405$, as in the considered range the Hamiltonian is almost symmetrical around K_c (which coincides with the zero of a $\mathcal{J}_0$ function, making all of the tunnelings except for $\widetilde{T}_{01}^{\pm}$ approximately proportional to $K - K_c$). The analysis of the system will mostly be focused on the properties of the boson composites in the system, which in the case of low effective tunnelings ($\tilde{J}_l$ and $\widetilde{T}_l$) form an effective lattice through which ↓ fermions can move (this lattice will be represented in the text as a chain of "0" and "C" characters, corresponding respectively to empty and filled lattice sites — note however, that this is only a simplified notation, while, due to PBC, the eigenstates of the system are actually superpositions of every possible translation of these configurations — see App. A).

As already established in [56], the system in the vicinity of $\widetilde{K}_c$ is in the DW phase (all the composites repel each other, 0C0C0C0C0C0C0C). For sufficiently big deviations from $\widetilde{K}_c$ the system enters clustered (CL) phase, where the composites stay close to each other (0000000CCCCCCC). In order to verify the correctness of this description one can first look at the fidelity susceptibility (1.25) for the ground state which should highlight the transition

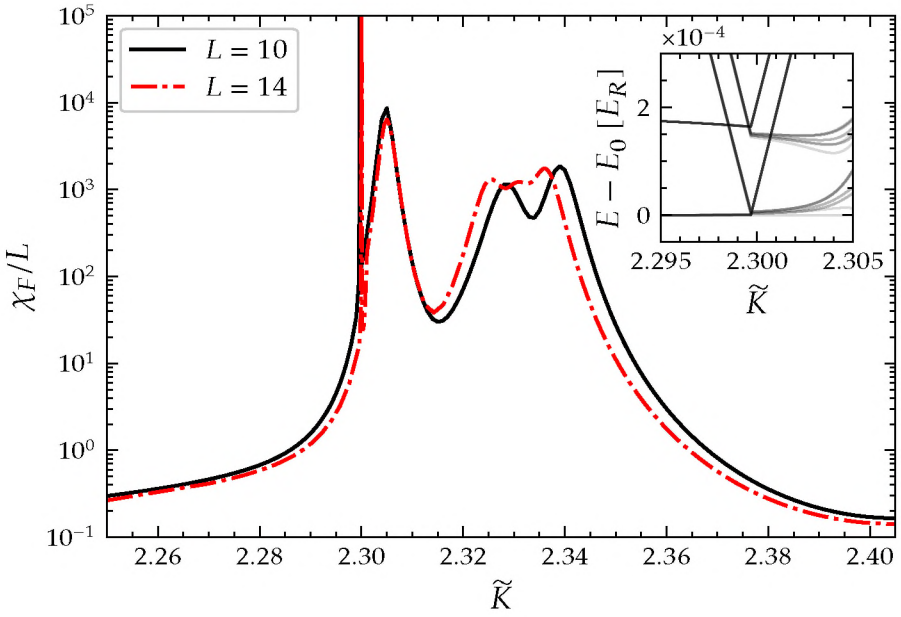

Figure 2.1: The fidelity susceptibility for system sizes $L = 10$ and $L = 14$. The sharpest peak (for $\widetilde{K} \approx 2.30$) is the result of the ground state energy crossing which marks the CL-MX phase transition, while other peaks signify transitions between different configurations in MX phase and MX-DW transition. The inset shows the energies of the lowest levels relative to the ground state energy in the vicinity of the energy crossing for $L = 10$ (lines are semi-transparent — opaqueness is proportional to the number of near-degenerate energies).

between different phases. The results, calculated for two system sizes: $L = 10$ and $L = 14$ are plotted in Fig. 2.1. The first, sharpest peak is the result of the ground state energy crossing. The presence of the other peaks hints at other phases and phase transitions present in the system.

Additional information about the phases present in the system can be acquired withe a help of the structure factor (1.29). It is easy to verify at which value of q there is a peak of $S(q)$ for both CL and DW phase, that is: $q_{\mathrm{CL}} = 2\pi/L$ and $q_{\mathrm{DW}} = \pi$. The values of $S(q)$ calculated for $L = 14$ [Fig. 2.2(a)] show that between the expected CL and DW phase exists a region where the density pattern changes multiple times. Thorough analysis of the ground state (as calculations are done by ED, full decomposition of the state into Fock basis is readily available) shows that the composites, which are uniformly spaced in the DW region, begin to merge together into clusters, whose size grows smaller the further away $\widetilde{K}$ is from $\widetilde{K}_c$, eventually forming single cluster after $\widetilde{K} \approx 2.30$ transition to CL phase. These phases, which correspond to configurations such as 00000CC00CCCCC and 000CC00CC00CCC [visible as peaks for respectively $q = 3\pi/7$ and $q = 4\pi/7$ in Fig. 2.2(a)] being the most significant component of the ground state, will be collectively labeled mixed phase (MX) throughout the text.

The results up to this point were restricted to small system sizes and one may wonder whether the appearance of MX is only a finite size effect, or if this phase persists for longer chains. In order to address this question, CL-MX and MX-DW transition points were obtained from χ_F calculated for $L = 10$, 14 and 18 (these values, along with linear fits for L^{-1} dependence are shown in Fig. 2.3).

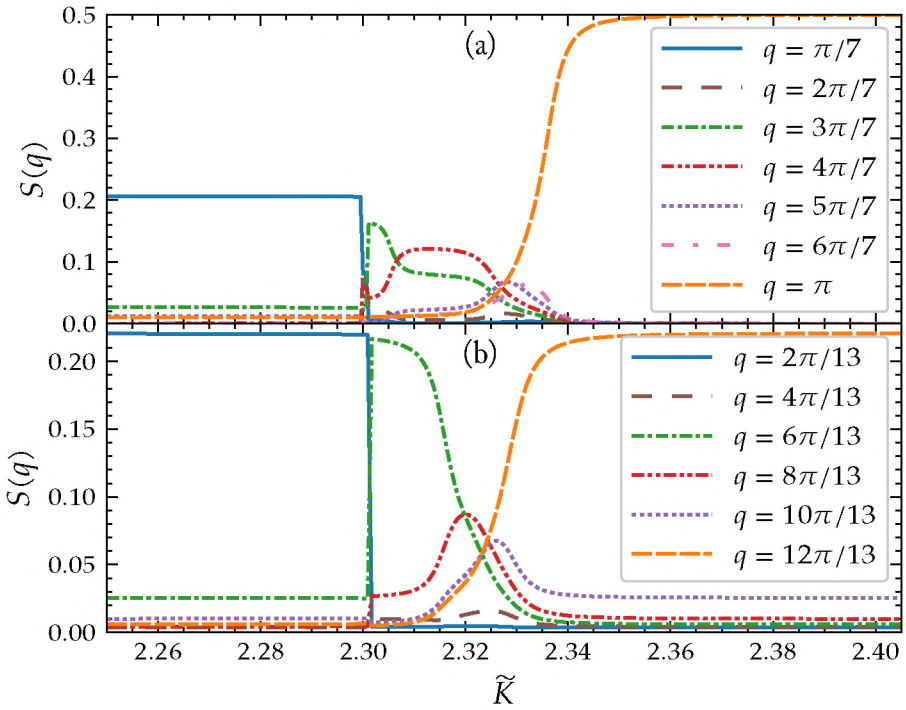

Figure 2.2: The ground state's structure factor calculated for $\Delta = 0$, $q = 2\pi z/L$ with $z \in 1, 2, \ldots L$ and: (a) $L = 14$, $n_c = n_\downarrow = \frac{1}{2}$, (b) $L = 13$, $n_c = 6/13$, $n_\downarrow = 7/13$. $S(q)$ is maximal for the smallest $q > 0$ in CL phase, for q closest to π in DW (a) or SHP (b), and for intermediate q values in MX phase.

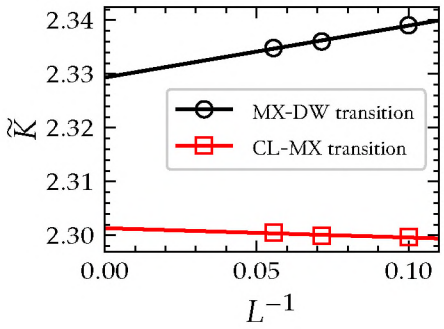

Figure 2.3: Extrapolation of MX-DW and CL-MX transitions for $\Delta = 0$ and $L \to \infty$, which suggests that MX phase is stable for arbitrarily long lattices.

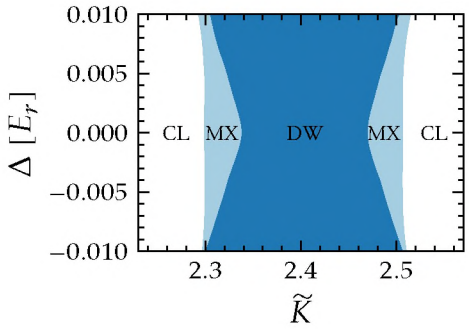

Figure 2.4: Phases of the system in $\widetilde{K}$–Δ plane based on χ_F calculated for $L = 10$. Similar results were also observed for $L = 14$ at selected points (See also Fig. 2.3).

2.3 Detuned and other cases

As the previous subsection dealt only with the resonant case, which is equivalent to SSH model, it is informative to find out if, and how, relaxing this condition may affect the behavior of the system. The results for moderate values of the detuning, $\Delta \in [-0.01, 0.01]$ (Fig. 2.4), show that with increasing $|\Delta|$ the MX phase spans over a smaller range of $\widetilde{K}$.

In order to make use of the topological properties of SSH/RM model, both topological and trivial phases must be present in the system, as localized, topological edge states appear

on the boundaries between them. Creating different domains is possible by slightly changing the filling of minority fermions/composites [creating holes (particles) for $n_c < \frac{1}{2}$ ($n_c > \frac{1}{2}$)] [56]. Such mechanism can be simulated with ED by setting the number of sites (L) to an odd number and the number of composites (N_c) to be close to $L/2$. In the case of $N_c = L/2 - 0.5$ [Fig. 2.2(b)] the DW phase is replaced with a single-hole phase (SHP), wherein the ground state contains a defect in the form of two neighboring, empty sites being present somewhere in the system. The value of q for which $S(q)$ is maximal correspondingly changes to $q = \pi(L-1)/L$ (from $q = \pi$ in DW). The CL-MX transition stays in approximately the same place, while the MX-SHP transitions shifts further away from $\widetilde{K}_c$ in comparison with $n_c = n_\downarrow = \frac{1}{2}$ case.

2.4 Conclusions

In the work presented in this chapter we used ED to perform an unbiased analysis of the periodically driven optical lattice system which resembles Rice-Mele model. The results show that in addition to DW and CL phases, transitory MX phase arises for intermediate $\widetilde{K}$ values. This phase is characterized by multiple defects present in the composite ordering which may prove to be beneficial in the context of hosting topological edge states in the system. We also checked cases of $\Delta \neq 0$ and composite filling away from $\frac{1}{2}$ which both result in similar phase structure (except for the fact that in the second case the DW necessarily contains some defects). Based on these results we conclude that Rice-Mele model should be a good description even for a realistic, non-ideal experimental setup, which in addition should provide a possibility of creating lattice defects, thus further increasing the viability of the setup in the context of manipulating topological edge states.

Chapter 3

Fibonacci anyons in a one-dimensional lattice

3.1 Introduction

As the topological systems with controlled non-Abelian anyons are desirable for their ability to perform universal quantum computations (see Sec. 1.3), many proposals of realizing such systems have been put forward. It has been shown that the one-dimensional extended Bose Hubbard model (1.15) for certain zero tunneling parameter sets is equivalent to an exactly solvable, thin-torus limit (i.e. $L_x \to 0$ while $L_x \cdot L_y = \text{const}$) of a two-dimensional theory resulting in topological Read-Rezayi states (which themselves are believed to explain some of the FQHE observations) [5]. In particular the case of filling $\nu = 3/2$ and $U = 2V$ seems to be interesting, as quasiparticles corresponding to the lowest energy domain walls between the degenerated ground state DW patterns resemble Fibonacci anyons and it had already received some mean field treatment [73]. In this section the problem is analyzed more comprehensively using ED and Density Matrix Renormalization Group (DMRG). The details are given in the accompanying paper [20].

The ground state of the system is fourfold degenerate and the basis of the degenerate manifold can be expressed in the Fock space as states: $[21] \equiv |2121...\rangle$, $[12] \equiv |1212...\rangle$, $[30] \equiv |3030...\rangle$, $[03] \equiv |0303...\rangle$. The lowest energy quasiparticles correspond to the following domain walls: [12][21], [21][30] and [03][12], which have the fractional charge $q/2$, and their counterparts of charge $-q/2$: [21][12], [30][21] and [12][03] (it is assumed here that a single boson has a charge q). The quasiparticle charge can be inferred from the number of bosons at a two-site boundary, which is 4 for $q/2$ domain walls and 2 for $-q/2$ ones (while in the ground state there are 3 bosons for every two neighboring sites).

A quick way to check that these domain walls show Fibonacci anyon-like behavior is to consider their adjacency matrix[5], defined for the ground states $|i\rangle$ as: $A_{ij} = 1$ if the domain wall between $|i\rangle$ and $|j\rangle$ is the quasiparticle of a given type and 0 otherwise, giving:

$$A = \begin{pmatrix} 0 & 1 & 1 & 0 \\ 1 & 0 & 0 & 1 \\ 1 & 0 & 0 & 0 \\ 0 & 1 & 0 & 0 \end{pmatrix}. \tag{3.1}$$

The quantum dimension D of the $\pm q/2$ quasiparticle corresponds to the dominant eigenvalue of A [68], and in this case is equal to $\left(1+\sqrt{5}\right)/2$, which is the value expected for Fibonacci anyons [66].

Another informative point of view is provided by the correspondence between hardcore bosonic systems and non-Abelian FQHE — k copies of hard-core bosonic system, projected and symmetrized onto k-hard-core [meaning: $(\hat{a}^\dagger)^k = 0$, where $\hat{a}^\dagger$ is the boson creation operator] bosons is analogous to Moore-Read Pfaffian state, while the excitations in a projected subspace show $SU(2)_k$ non-Abelian properties [55]. In our case, $k = 3$ ($SU(2)_3$ symmetry corresponds to Fibonacci anyons [66]) and the symmetrized projector has the form $\mathcal{P} = \bigotimes_i \mathcal{P}_i$, with:

$$\mathcal{P}_i = \begin{pmatrix} 1 & 0 & 0 & 0 & 0 & 0 & 0 & 0 \\ 0 & 1 & 1 & 1 & 0 & 0 & 0 & 0 \\ 0 & 0 & 0 & 0 & \sqrt{2} & \sqrt{2} & \sqrt{2} & 0 \\ 0 & 0 & 0 & 0 & 0 & 0 & 0 & \sqrt{6} \end{pmatrix}, \tag{3.2}$$

where the rows (columns) correspond to the basis states of 3-hard-core bosonic system (product of 3 copies of hard-core bosonic system) on i^{th} site, in the order of an increasing total number of bosons (in other words: $\mathcal{P}$, for each site, projects n bosons distributed among 3 hard-core copies to n bosons in a single 3-hard-core system).

3.2 Low tunneling behavior

While the correspondence explained in the introduction is exact for $t = 0$, typically in any experimental setup t is non-zero. In order to verify whether we can expect Fibonacci anyon-like behavior in realistic systems, we us the following procedure. First, we calculate the lowest energy eigenstates of the regular (that is, non-hard-core) EBHM. Then we do the same for the hard-core boson EBHM and create ansatz states by summing 3 copies of the obtained states and projecting them using $\mathcal{P}$ (the resulting states contain anyonic excitations by construction). The similarity between the ansatz states can be then measured as a simple overlap. In both of these cases we use ED with PBC to get the eigenstates, in the case of EBHM we impose an additional constraint: the number of particles on each site is at most 3 - which is fairly accurate for small values of t and enables us to reach bigger system sizes.

The energy level structure of the system for considered parameter range is split into two degenerate (semidegenerate for $t \neq 0$) manifolds, corresponding respectively to the ground states and the states containing two domain walls (states can not have only one domain wall because of PBC). As the projection $\mathcal{P}$ does not necessarily result in orthogonal states, we use a simple Gram-Schmidt orthonormalization procedure to get the basis. The overlap O of the i^{th} eigenstate of EBHM, $|i_{\text{EBH}}\rangle$, with the Hilbert subspace spanned by the projected and orthogonalized ansatz states, $|j_{\text{ansatz}}\rangle$, is calculated as:

$$O_i = \sqrt{\sum_j |\langle i_{\text{EBH}} | j_{\text{ansatz}} \rangle|^2}. \tag{3.3}$$

First, we take a look at the (semi-)degenerate ground state manifold for two cases: $U = 2V$ and $U = 1.99V$. (The motivation for the second case is following: the degeneracy between states [12], [21] and [03], [30] – which is necessary for non-Abelian anyons —

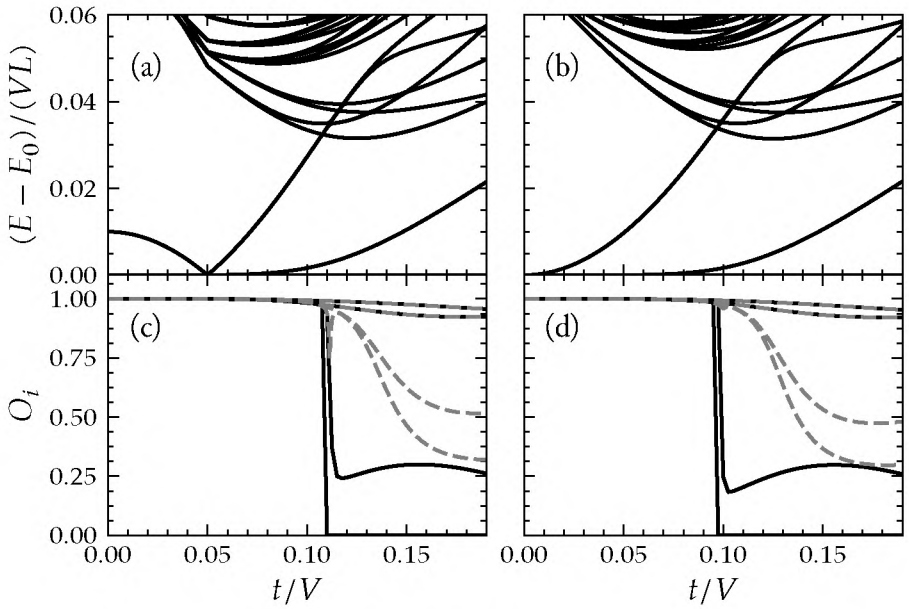

Figure 3.1: (a) and (b): the lowest energies relative to the ground state energy, (c) and (d): the overlap between the 4 lowest energy states (black, solid lines) / maximal overlap states(grey, dashed lines) of EBH Hamiltonian and 4 lowest ansatz states ($\mathcal{P}$ projection of 3 copies of hard-core boson systems) for $L = 14$, $U = 1.99V$ [(a) and (c)] and $U = 2V$ [(b) and (d)]. Drop in the overlap values in both of these cases coincides with first energy level crossings visible in (a) and (b).

is quickly removed with an increasing t/V. By introducing slight detuning in U, we get almost-degeneracy at some finite tunneling — $t/V \approx 0.05$ in this case — instead of an exact degeneracy at $t = 0$.) The overlap between the four lowest energy states of the EBH Hamiltonian and the ansatz states in these cases (for $L = 14$) is shown as black lines in the lower graphs in Fig. 3.1 — the overlaps between those states is approximately 1 up to $t/V \approx 0.1$, where an energy crossing in the lowest energy states (visible in the upper graphs) occurs and the overlaps fall dramatically, as these states are no longer related to the initial DW patterns. If, instead of using the lowest energy states, we use the states that resemble the initial DW patterns the most, we still see a visible drop in the overlap (gray, dashed lines).

Similar analysis can be performed for the states containing the lowest energy domain walls (2 of them, because of PBC as was mentioned earlier). The corresponding energy manifold accordingly contains $3L(L/2-1)$ states, whose overlaps with the ansatz states (which in these case correspond to 2 copies of the hardcore bosonic system being in the ground state and the other one in the excited state) are presented in Fig. 3.2. The drop of the overlap value, visible for $t/V \approx 0.55$ can be, similarly to the ground states case, traced to the energy level crossing, which in this case happens for higher energy eigenstates [Fig. 3.2(a)]. For $t/V < 0.5$ we have $O_i > 0.9$, which suggests that even for non-negligible tunneling the domain walls retain at least some of their original characteristics.

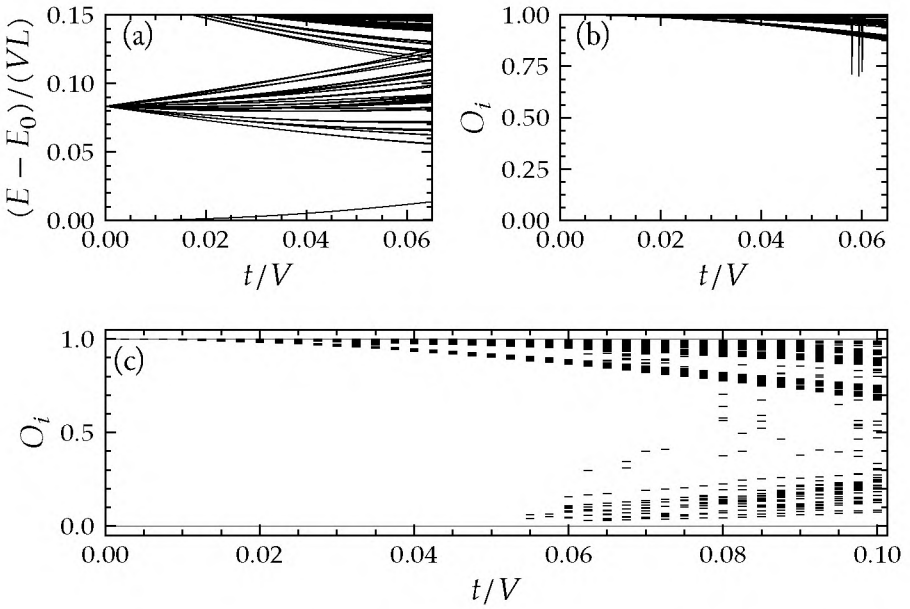

Figure 3.2: (a): energy levels relative to the ground state energy, (b): maximal overlaps of EBH states and ansatz states containing two $\pm q/2$ domain walls, (c) overlaps of the lowest (excluding 4 states from the ground states' manifold) EBH states and ansatz states containing two $\pm q/2$ domain walls. Data for $U = 2$ and: $L = 10$ [(a) and (b)] and $L = 12$ [(c)]. Decrease in the overlap in this case is due to energy level crossing in the higher energy manifold for $t/V \approx 0.055$.

3.3 Density wave to superfluid transition

In the previous section we showed that an energy level crossing of a semi-degenerate ground states manifold is related to a sharp drop in the overlaps between the EBH and ansatz states. This crossing marks the QPT between the DW phase and the SF phase. There exist conflicting characterizations of this QPT in the literature, as Gutzwiller-ansatz mean field approach suggests the appearance of an intermediate, supersolid phase between DW and SF phases [73], while DMRG and QMC calculations predict a direct DW-SF transition for a similar ($U/V = 4/3$) system [9]. We thus found it necessary to properly study the transition with the help of DMRG (see App. B).

We first look at the fidelity susceptibility (1.25) calculated for a wide range of system sizes (Fig. 3.3). The DMRG calculations were performed with PBC (same as ED in previous section) and for similar maximum particles per site cutoff: $N_{\max} = 3$ (the relative error introduced with this constraint for $L = 14$ is presented in the inset of Fig. 3.3), the bond dimension was up to 1200 (for $L = 124$). The single peak of fidelity is characteristic of a direct transition between two phases, and we can further compare the characteristics of the χ_F behavior to those of the Berezinskii-Kosterlitz-Thouless transition, for which [64]:

$$\chi_F(L) \simeq \chi_0 - \chi_1 \ln^{-1}(L/a) + O\left[\ln^{-2}(L/a)\right], \tag{3.4}$$

$$\max(\bar{t}) \simeq A + B \ln^{-2}(L/a) + \cdots, \tag{3.5}$$

where a is some lattice cutoff and $\bar{t} \equiv t/V$. The scaling (Fig. 3.4) gives the extrapolated location of the transition: $\bar{t}_c = 0.158 \pm 0.004$.

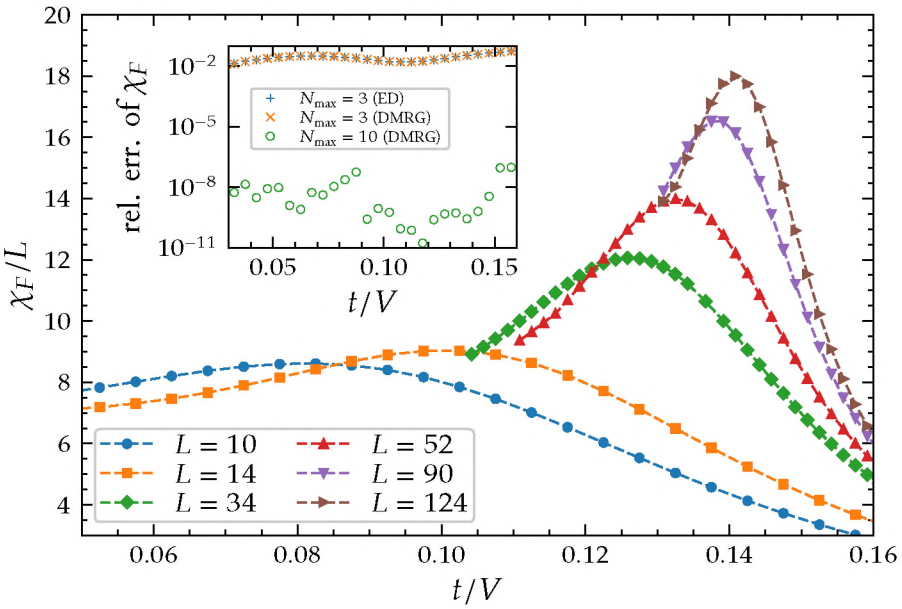

Figure 3.3: The fidelity susceptibility χ_F in the vicinity of DW-SF transition for different system sizes L. The inset shows the relative error of χ_F calculated for $L = 14$ and different $N_{\max}$ using either ED or DMRG, with respect to the value calculated for $N_{\max} = 15$ (DMRG).

Another method of determining the critical point of the QPT is based on the central charge, c (1.31) (in order to get the correct values of c the bond dimension of the DMRG was increased up to 2200; particle per site cutoff was also increased to $N_{\max} = 4$). As L is increased, the maximum of $c(\bar{t})$ gets closer to the value expected for SF, that is $c = 1$, and the position of this maximum gets closer to the critical point of the QPT [53]. While the biggest L which we were able to use was only $L = 70$, the position of the maximum does not vary much with size (see Fig. 3.5) and thus we conclude from the data that $\bar{t}_c \approx 0.162$, which is in agreement with the value obtained from χ_F scaling.

We define the correlation length for the system size L as:

$$\xi(L) = \sqrt{\frac{\sum_{i,j=1}^{L/2} (i-j)^2 \langle a_i^\dagger a_j \rangle}{\sum_{i,j=1}^{L/2} \langle a_i^\dagger a_j \rangle}}, \tag{3.6}$$

where summation is up to $L/2$ and not L because of the PBC. If the QPT between DW and SF is indeed a direct one, we should expect that the order parameter of DW phase, the structure factor at π (1.29) in the vicinity of $\bar{t}_c$ is a power-law function of ξ:

$$S(\pi) \sim \xi^{\gamma/\nu} \Phi(\xi/L), \tag{3.7}$$

where $\Phi(\xi/L)$ is some scaling function [45]. The values of $S(\pi)$ and ξ, calculated for different system sizes and for $\bar{t}_c$ obtained from χ_F (that is $\bar{t}_c \approx 0.158$) are shown in Fig. 3.6. The fitted line corresponds to $\gamma/\nu \approx -0.78$ and its near-perfect match to data strengthens the claim that there are no additional phases between DW and SF.

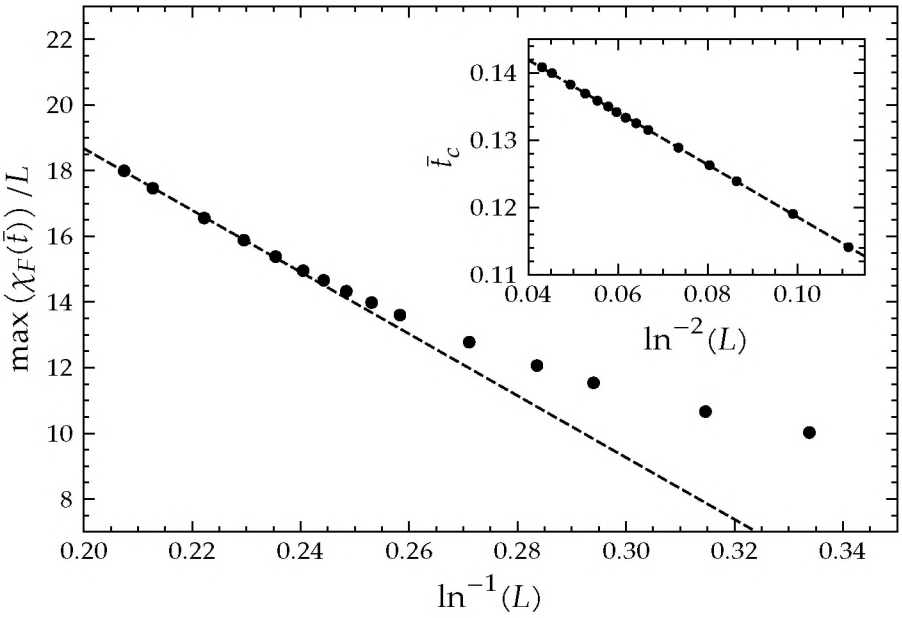

Figure 3.4: The scaling of the maximum of fidelity susceptibility, $\chi_F(\bar{t}_c)/L$, and its position ($\bar{t}_c$) on L for $U = 2V$. Dashed lines are fits to eqs. (3.4) and (3.5) with $A \approx 0.158$, $B \approx -0.39$, $\chi_0 \approx 37.5$ and $\chi_1 \approx -94.2$. For the χ_F fit only the values for 5 largest Ls were used.

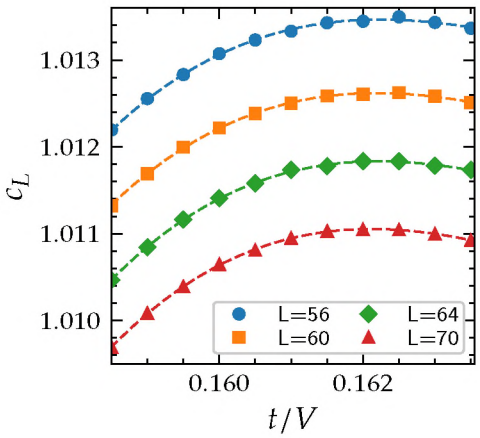

Figure 3.5: Central charge obtained with DMRG (PBC). The maxima for pictured Ls are all located slightly above $t/V = 0.162$ and linear (with respect to $1/L$) extrapolation yields $\lim_{L\to\infty} \bar{t}_c \approx 1.617$, while $\lim_{L\to\infty} c_L \approx 1.001$.

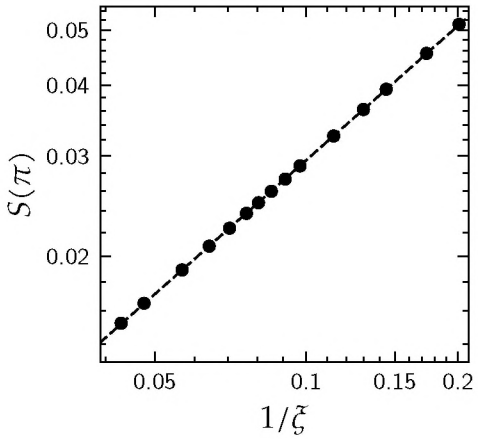

Figure 3.6: The relation between the structure factor $S(\pi)$ and the inverse correlation length $1/\xi$ at $\bar{t}_c \approx 0.158$. The dashed line is the power-law fit (3.7) with $\gamma/\nu \approx -0.78$ and $\Phi(\xi/L) = 1$.

3.4 Further remarks

The domain walls described in this chapter may be used in experiments or quantum computation only if there is a reliable method of their creation and manipulation. One of the proposed solutions is locally changing the chemical potential with a single site resolution — creating the domain walls with $q/2$ ($-q/2$) can be achieved by increasing (decreasing) the value of μ

on two neighboring sites. Another experimental problem is the inability to actually move the quasiparticles around each other in a one-dimensional lattice. The protocol for realizing this objective based on using so-called T-junctions has already been analyzed for Majorana fermions [3] and we believe that it should be also applicable to Fibonacci anyons in cold atomic systems. In the original scheme, three one-dimensional segments are connected at one point and by moving the quasiparticles through the segments (of which only two are in topological phase at the same time) in the right order it is possible to exchange the quasiparticles' positions.

To conclude, we studied a one-dimensional EBHM for filling $\nu = 3/2$ and close to $U = 2V$ with a focus on anyonic properties of its low energy excitations. By calculating the overlaps of these excitations and the ansatz wave functions, which by construction have non-Abelian topological order, we demonstrated the system in question supports Fibonacci anyon-like quasiparticles even for non-negligible tunnelings. We have also shown that according to DMRG results there is a direct DW-SF QPT and no supersolid phases are present on the boundary between these two phases.

Chapter 4

Extended Bose-Hubbard model in dipolar gases

4.1 Introduction

Using the model introduced in Sec. 1.2.3, this chapter presents a careful examination of the dipolar bosonic gas trapped in an effectively one-dimensional optical lattice and closely follows the accompanying paper [12]. Such systems have been given a reasonable amount of attention, mostly thanks to recent experimental efforts which resulted in trapping atoms of ever-bigger dipolar momenta, giving hope for realizing topological states of matter resulting from long-range interactions between particles (such as the Haldane insulator phase). The existing literature is, however, either limited to standard EBHM (ignoring terms such as next nearest neighbor interactions and density dependent tunneling) or very small system sizes (where ED is still applicable).

The system considered consists of a dipolar species of particles trapped in a 3D optical lattice with potential heights V_x, V_y and V_z such that $V_y = V_z = 50E_R$ and $V_x \ll V_y, V_z$ (effectively freezing the dynamics in y and z direction). We assume the Hamiltonian is similar to (1.16), however we also include next-nearest neighbor tunnelings and interactions (respectively t_{nnn} and V_{nnn}) and assume $P = 0$ (this term, being much smaller than the ones we include[21], does not bring any qualitative differences). The parameters arising from interactions between particles (U, V, V_{nnn} and T) have their origins in both the contact [which we assume in the form of $V_{\mathrm{contact}}(\mathbf{r}) = 4\pi\hbar^2 a_s/m\,\delta(\mathbf{r})$, with a_s being the effective scattering length and m mass of the particle] and the dipolar (1.14) interactions, such that $U = U_{\mathrm{contact}} + U_{\mathrm{dipolar}}$ and so on (where U_{contact} and U_{dipolar} are calculated using (1.11) for an appropriate potential).

As the proportion V/U is much smaller than 1 [see the inset of Fig. 4.1(a)] for the typical optical lattice setups, we propose using Feshbach resonance (which enables us to modify a_s using a magnetic field) in order to balance contact and dipolar interactions in such a way that V/U has the desired value. In our scheme we assume that we are able to change the values of a_s and V_x, which allows us to satisfy two chosen constraints on Hamiltonian parameter values, which we choose to relate t, U and V with each other (so we can work in a two-dimensional space of parameters, e.g. U/t and V/t). To obtain the exact values of a_s and V_x, the strength

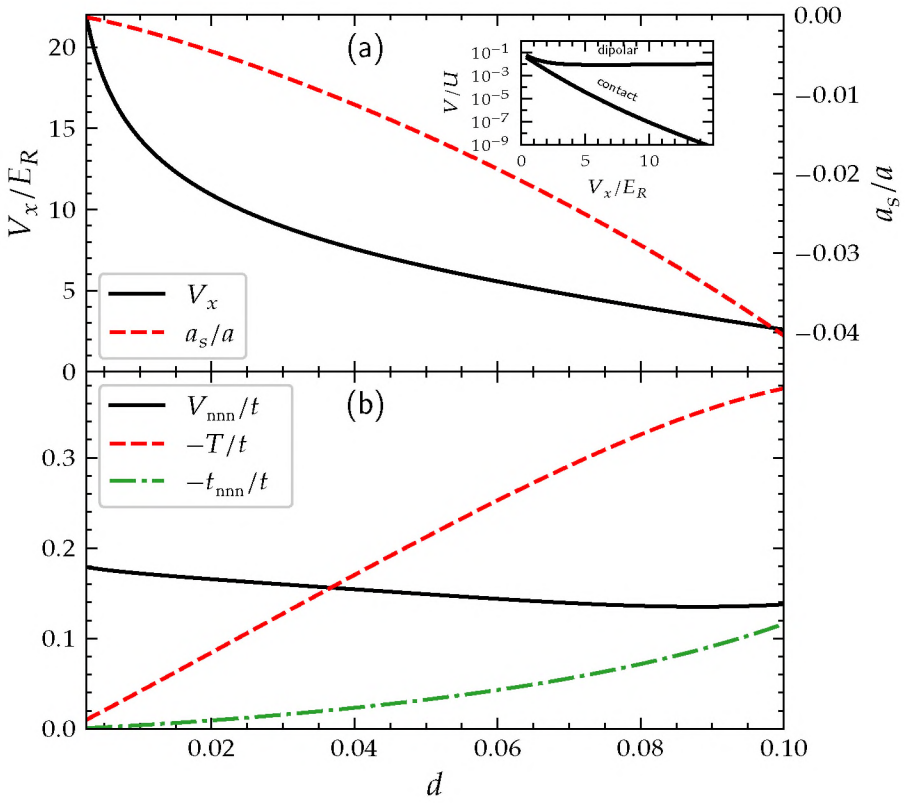

Figure 4.1: (a) The values of V_x/E_R and a_s/a necessary for $U/t = 2$ and $V/t = 1.5$ to hold true and (b) the values of the extra parameters added to EBH Hamiltonian in relation to the strength of the dipolar interactions, d. The inset of (a): the relative magnitude of V and U Hamiltonian parameters calculated separately for contact and dipolar interactions.

of the dipolar interactions, parametrized here using a dimensionless quantity:

$$d = mC_{\mathrm{dipole}}/(2\pi^3\hbar^2 a) \tag{4.1}$$

has to be known. The values of V_x and E_r needed to obtain $U/t = 2$ and $V/t = 1.5$ depending on d are shown in Fig. 4.1(a). The value of d ranges between 10^{-3} and 10^{-2} for recently trapped atoms, such as ^{52}Cr and ^{164}Dy (for molecules it can be much higher, e.g. $d \approx 0.1$ for $^{168}Er_2$). With the values of V_x, a_s and d known, all of the parameters in the Hamiltonian can be determined [see Fig. 4.1(b)].

All of the results presented in this chapter have been obtained using DMRG with open boundary conditions (unless stated otherwise). We thus typically exclude the chemical potential term from the Hamiltonian (as the DMRG works with the fixed number of particles). Furthermore, we impose additional Hamiltonian terms at the boundaries, equal to the effect the ideal DW configuration (for appropriate lattice filling) would have, whose main purpose is to break the DW degeneracy (e.g., for $\rho = 2$, where the density wave has the form $|0202\ldots\rangle$ in the Fock space, these terms would be $2V\hat{n}_1 + 2V_{\mathrm{nnn}}(\hat{n}_2 + \hat{n}_L)$).

4.2 Phase transitions at ρ=1

The case of $\rho = 1$ filling is particularly interesting, as in this case the EBHM hosts the HI phase. Because of that, the problem of determining the phases in this case has already been given considerable attention and the phase diagram can be found in multiple works. Here I will only provide a brief summary and afterwards I will present in which way the inclusion of V_{nnn}, T and t_{nnn} (which are evaluated for the practical realization of EBH in cold atoms, as explained in the introduction) changes the already established picture. The phases of the system are:

- MI for large values of U/t and small values of V/t,
- SF for small values of both U/t and V/t,
- DW for large values of U/t and V/t,
- HI for an intermediate values of U/t and V/t.

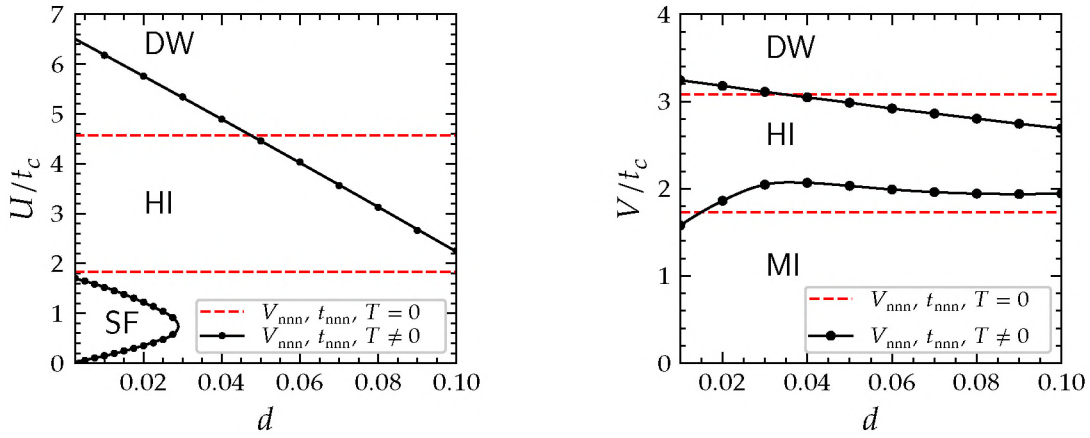

Figure 4.2: Critical values of U/t (a) and V/t (b) for the QPTs between the phases present in the system. The values for a regular EBHM are marked with red dashed lines, while points mark the results obtained for the model including additional terms (black solid lines are interpolations between these). In each case some constraint between the values of t, U and V is assumed: $V/U = 3/4$ for (a) and $U/t = 3$ for (b).

In order to provide somewhat clear picture of the effect that the dipolar interactions have on the extent of the HI phase, we restrict ourselves to two cuts of U/t-V/t plane. The first of these is $V/U = 3/4$ and the phases in this case are (in the order of decreasing tunneling): SF, HI and DW (so that there are two QPTs: SF-HI and HI-DW). The other one is $U/t = 3$, in which case for large tunnelings the system is in the MI phase instead of the SF phase. The phase boundaries obtained here (the method is described in more detail in following paragraphs) are compared with their locations for the case of simple EBHM (that is, $V_{\mathrm{nnn}} = T = t_{\mathrm{nnn}} = 0$) which can be found in the literature (we additionally verified those using our DMRG code). For the comparison, see Fig. 4.2.

While qualitatively the picture does not change much with the inclusion of additional terms in the Hamiltonian, one can see that in the case of $V/U = 3/4$ the changes can be

pretty drastic - as the value of d increases, the boundaries shift heavily to larger values of the tunneling. A curious effect is the appearance of the boundary between SF and HI for large values of tunnelings, which seems counterintuitive. Take note, however, that the lower part of Fig. 4.2(a) ($U/t \approx 0$) is the regime where our model does not hold — the bigger d is and t should be, the lower V_x/E_R must be [see also Fig. 4.1(a)] and at some point the lattice becomes too shallow to be described correctly without including longer range tunnelings (which is the reason for including t_{nnn} terms in our Hamiltonian).

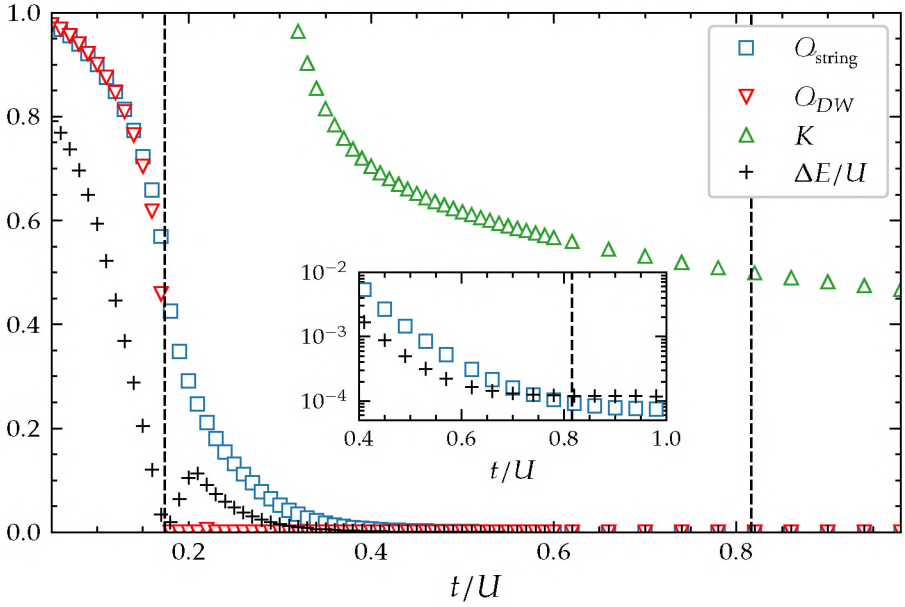

Figure 4.3: The string and DW order parameters, the energy gap and the critical exponent K calculated for $V/U = 3/4$ and $d = 0.02$ using DMRG. Black dashed lines mark the positions of the QPTs. The location of DW-HI transition ($t_c/U \approx 0.175$) was determined using ΔE (which must be 0 at the transition, as HI is a topological phase) and O_{DW} (which has a finite value in DW phase and is 0 otherwise). HI-SF transition ($t_c/U \approx 0.82$) is located using a fact that $K = 0.5$ at the transition (see text). The inset shows the decay of O_{string} and ΔE on the logarithmic scale.

To determine QPTs locations, we used the following quantities: the energy gap between the ground and the excited state (ΔE) and the order parameters $O_p \equiv \lim_{r\to\infty} C_p(r)$ with:

$$C_{\mathrm{SF}(r)} = \langle b_j^\dagger b_{j+r}\rangle\,, \tag{4.2}$$

$$C_{\mathrm{DW}(r)} = (-1)^r \langle \delta n_j \delta n_{j+r}\rangle \text{ and} \tag{4.3}$$

$$C_{\mathrm{string}(r)} = \langle \delta n_j e^{i\pi \sum_{j\le k\le j+r} \delta n_k} \delta n_{j+r}\rangle\,. \tag{4.4}$$

In order to properly determine the phase boundaries, all of these parameters were extrapolated in the thermodynamical limit, $L \to \infty$, based on the data obtained for $L = 100$, 200, 300 and 400.

The exemplary values used in the determination of phase boundaries are shown in Fig. 4.3 ($d = 0.02$, $V/U = 3/4$) and Fig. 4.4 ($d = 0.09$, $U/t = 3$). In the case of $V/U = 3/4$, we were unable to determine the location of HI-SF transition based on the order parameters mentioned before — even though both ΔE and O_{string} are non-zero in HI phase and must be

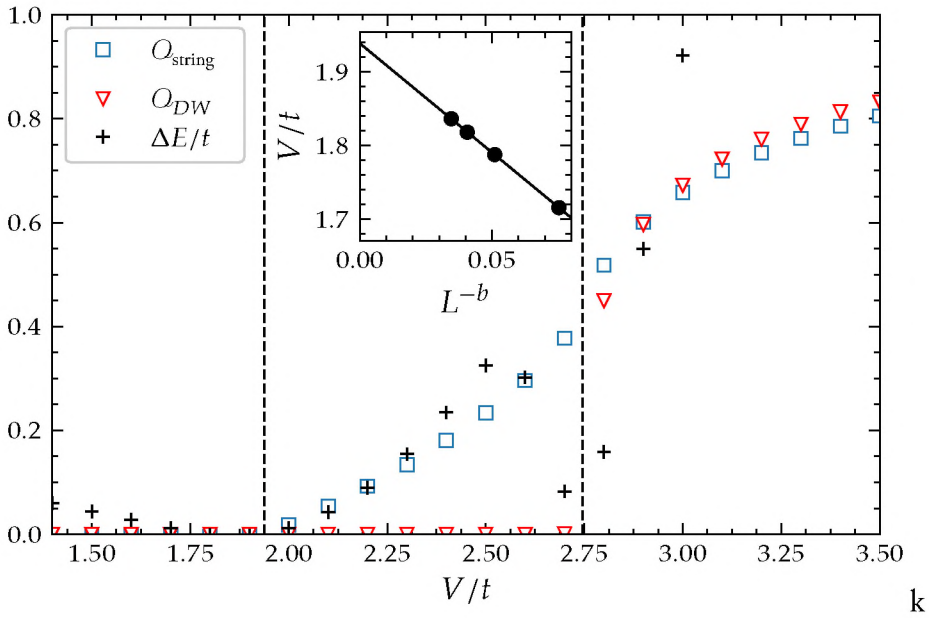

Figure 4.4: The string and DW order parameters and the energy gap calculated for $U/t = 3$ and $d = 0.09$ using DMRG. Black dashed lines mark the positions of the QPTs. DW-HI location ($V/t_c \approx 2.74$) is determined in the same way as described in the caption of Fig. 4.3. The energy gap closes at the HI-MI transition, however the extrapolated values of ΔE do not provide a clear-cut location of this closing. We resort to a different method: we extrapolate the position of the minimum of ΔE using a function: $V/t = V/t_c + aL^{-b}$. The result of this fit is shown in the inset ($V/t_c = 1.94$, $a \approx -2.96$, $b \approx 0.56$).

0 when the system is in SF phase, our results do not show clearly where does this transition take place [see the inset of Fig. 4.3]. To circumvent this problem we resort to (1.28) which describes C_{SF} behavior in the SF phase — it is known that the parameter K on the boundary of the superfluid phase for $\nu = 1$ filling is equal to 0.5 [46].

4.3 Phases for $d = 0.1$

Haldane insulator phase is not the only interesting aspect of EBHM. The model supports the formation of supersolid phases, which manifests non-zero DW order simultaneously with SF-like power-law decay of correlation functions. Including additional terms arising from dipolar interaction (such as density induced tunnelings and pair tunneling) leads to pair-correlated phases [63]. In order to address the question of which of these phases are to be expected in a realistic system with large dipolar interactions, we present the phase diagram of the system with unconstrained lattice density for $V/U = 3/4$ and $d = 0.1$ (Fig. 4.5).

4.3.1 Density wave phases

The ground states of the system in DW phases have a form of alternating empty and filled sites, which for lattice density $\rho = n/2$, $n \in \mathbb{N}$ is representable in Fock space as $|0n0n...\rangle$. The inclusion of V_{nnn} in our model gives rise to additional DW phases for density $\rho = (2m+1)/4$, $m \in \mathbb{N}$, namely $|0m0(m+1)...\rangle$. The boundaries of DW phases can be calculated

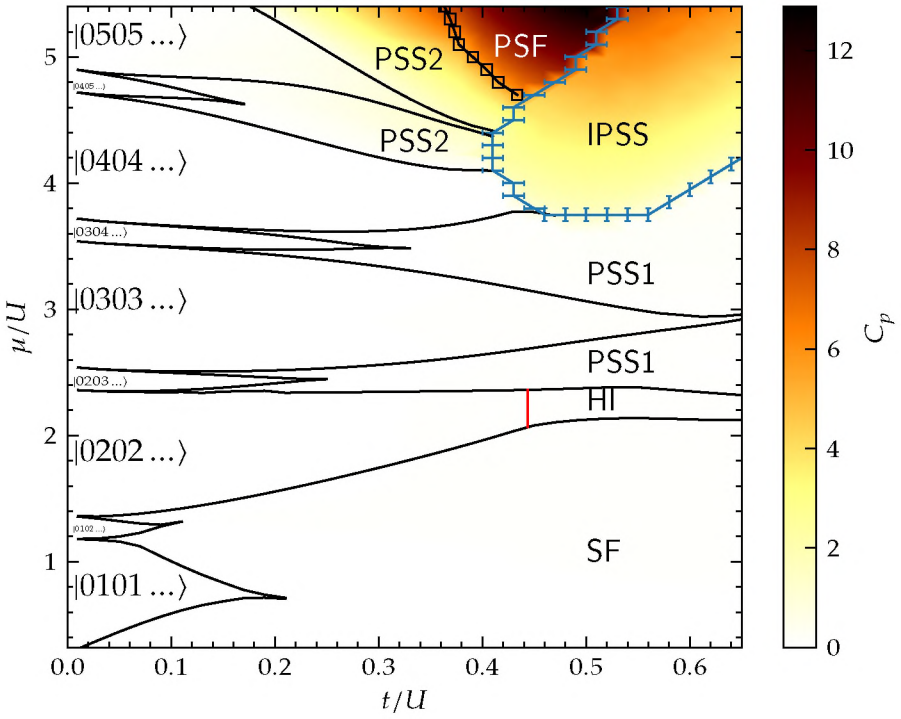

Figure 4.5: Phase diagram of the system for $V/U = 3/4$ and $d = 0.1$. Data for phases other than IPSS are obtained using OBC DMRG for $L = 200$ sites. Black lines showing transitions from DW phases were obtained from the dependence of the energy on the number of particles in the simulation (see text). Most of the pair-superfluid phases (PSS1, PSS2, IPSS and PSF) are distinguished by non-zero value of pair-tunneling correlations C_p, in the case of PSS1 however nearest-neighbor correlations are insufficient to infer its pair-superfluidity (see Fig. 4.6). Supersolid (PSS1, PSS2 and IPSS) phases are distinguished by non-zero DW order, for IPSS this order is incommensurate.

as $\mu_\pm = lim_{N=(N_{\mathrm{DW}})^\pm} \partial E(N)/\partial N$ (where N_{DW} is a total number of particles in a lattice corresponding to a given DW pattern) using DMRG results. Although this values depend on the system size, we set the system size $L = 200$ in our calculations which is sufficiently big to get reasonable value of the chemical potential. Another justifiable approximation we employ is $\mu_\pm \approx \pm[E(N_{\mathrm{DW}} \pm 1) - E(N_{\mathrm{DW}})]$ instead of a proper derivative, although to get μ values for the lobes we also take into account $E(N_{\mathrm{DW}} \pm 2)$ values, performing a quadratic interpolation of $E(N)$ on each side of N_{DW} and calculating a proper derivatives.

4.3.2 Superfluid and pair-superfluid phases

Superfluidity is manifested through the behavior of the correlation function (4.3), which then shows a power-law decay. A simpler approach would be to consider only the next-nearest neighbors, resulting in the quantity $\sum_i \langle b_i^\dagger b_{i+1} \rangle / L$, which is directly related to the tunneling term in the BH-like models. Here we will also consider similar correlation function associated

with pair-tunneling and a simplified quantity in the form of the pair-tunneling correlation:

$$C_p = \frac{1}{L}\sum_i \langle (b_i^\dagger)^2 (b_{i+1})^2 \rangle . \tag{4.5}$$

The values of C_p calculated for different densities (as indicated by the value of μ) and tunneling strengths are shown in Fig. 4.5.

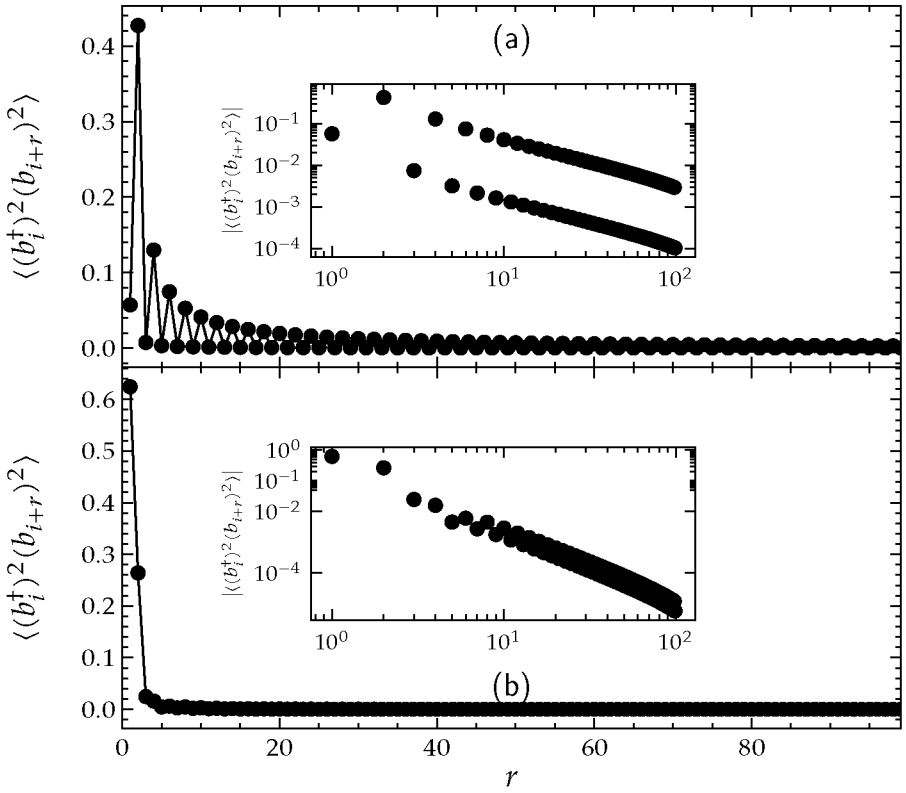

Figure 4.6: OBC DMRG results of $\langle (b_i^\dagger b_{i+r}) \rangle$ correlations averaged in the middle (half of the sites) of an $L = 200$ lattice for (a) PSS1 phase at $\rho = 1.25$, $t/U = 0.59$ and (b) PSS2 phase at $\rho = 2.25$, $t/U = 0.37$, both of them showing power-like decay. Log-log plots of the respective correlations are shown in the insets.

For $\rho < 1$ only DW and SF (power-law C_{SF} decay and no finite order parameters) phases are present in the system. Interestingly, the system supports pair-superfluidity for high densities of particles in the system even though the Hamiltonian of the model considered in this work does not contain pair-tunneling terms (note however the inclusion of density-dependent tunneling terms, $b_i^\dagger(\hat{n}_{i+1} + \hat{n}_{i+1})\hat{b}_{i+1}$, in the Hamiltonian). Large tunneling leads to pair-superfluid phases (PSS1 and PSS2), for which both DW order and pair-superfluidity is present, while there is also pair-superfluid (PSF) regime (pair-superfluidity without DW order) and a region where the system is in the phase we dub incommensurate pair-supersolid (IPSS, expanded upon in the next subsection). While pair-superfluidity for PSS1 phase is not clear from the value of C_p (due to strong DW order present in the phase, which suppresses nearest neighbor correlations), it is evident if we consider the dependence of the pair-correlation function on the distance (Fig. 4.6).

4.3.3 Incommensurate pair-supersolid

The most basic characterization of the IPSS is its DW order, which in contrast to DW phases considered up to this point does not correspond to the structure factor (1.29) peaking at $q = \pi$, but instead the wavenumber this peak occurs for appears to be in general an irrational number (so that the density wave is incommensurate in relation to the lattice constant). This requirement forces us to adopt a different numerical method, as the DMRG used earlier assumes a fixed number of particles in a lattices of a fixed length which necessarily imposes rational values of wavenumber and density. To circumvent this limitation we did the simulations for the IPSS phase using a so called sine square deformation (SSD) DMRG: it differs from the regular DMRG in that the Hamiltonian is multiplied by a position-dependent sine square function $[\sin^2(i\pi/L)]$. This enables the lattice edges (which now contribute only negligible energy) to act as a reservoir of particles (or holes) for the system — the middle part of the lattice — to which the particle number constraints no longer apply (see App. B), allowing us to include the chemical potential term again.

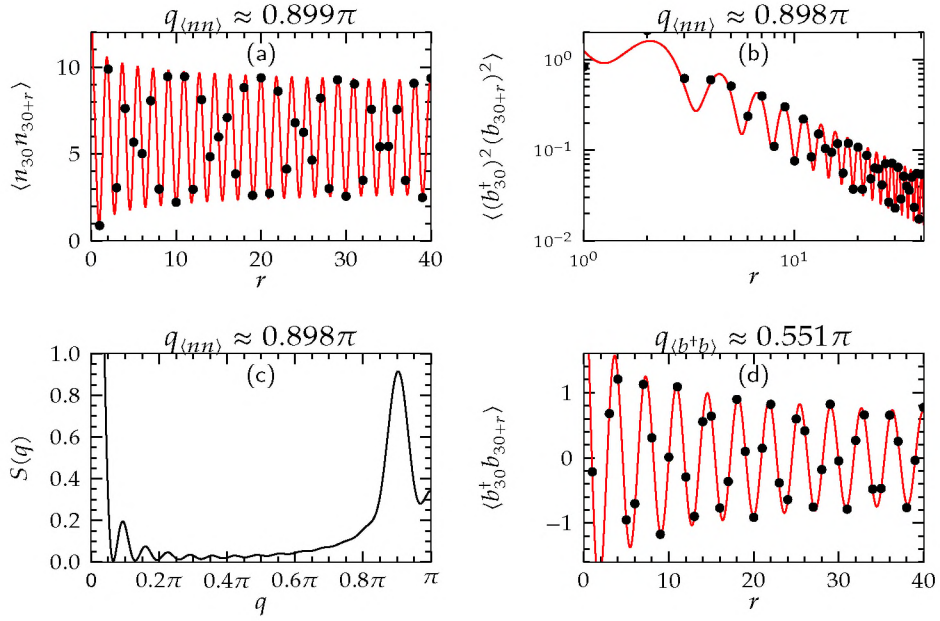

Figure 4.7: Fits of the SSD DMRG ($L = 100$) data to: (a) (4.7), (b) (4.8), (d) (4.9), and (c) values of $S(q)$ for $t/U = 0.48$ and $\mu = 3.7$. Wavenumber values obtained this way are written above each plot. Only the middle 40% of the lattice sites are considered.

The following formulas are valid for the ground states of the system in IPSS phase (and as such they are used to determine the extent of the phase in Fig. 4.5):

$$\langle n_i\rangle = \rho_{\text{bulk}} + \Delta\rho \sin\left(q_{\langle nn\rangle} i + \varphi_0\right), \tag{4.6}$$

$$\langle n_i n_{i+r}\rangle = C_1 + A_1 \sin\left(q_{\langle nn\rangle} r + \varphi_1\right) r^{-\alpha_1}, \tag{4.7}$$

$$\left\langle (b_i^\dagger)^2 (b_{i+r})^2\right\rangle = \left[C_2 + A_2 \sin\left(q_{\langle nn\rangle} r + \varphi_2\right)\right] r^{-\alpha_2}, \tag{4.8}$$

$$C_{\text{DW}}(r) = A_3 \sin\left(q_{\langle b^\dagger b\rangle} r + \varphi_3\right) r^{-\alpha_3}, \tag{4.9}$$

where we see that correlations decay as a power law, however there is an oscillatory modulation, whose wavenumber is $q_{\langle nn\rangle}$ for density, pair-correlations and density correlations [accordingly,

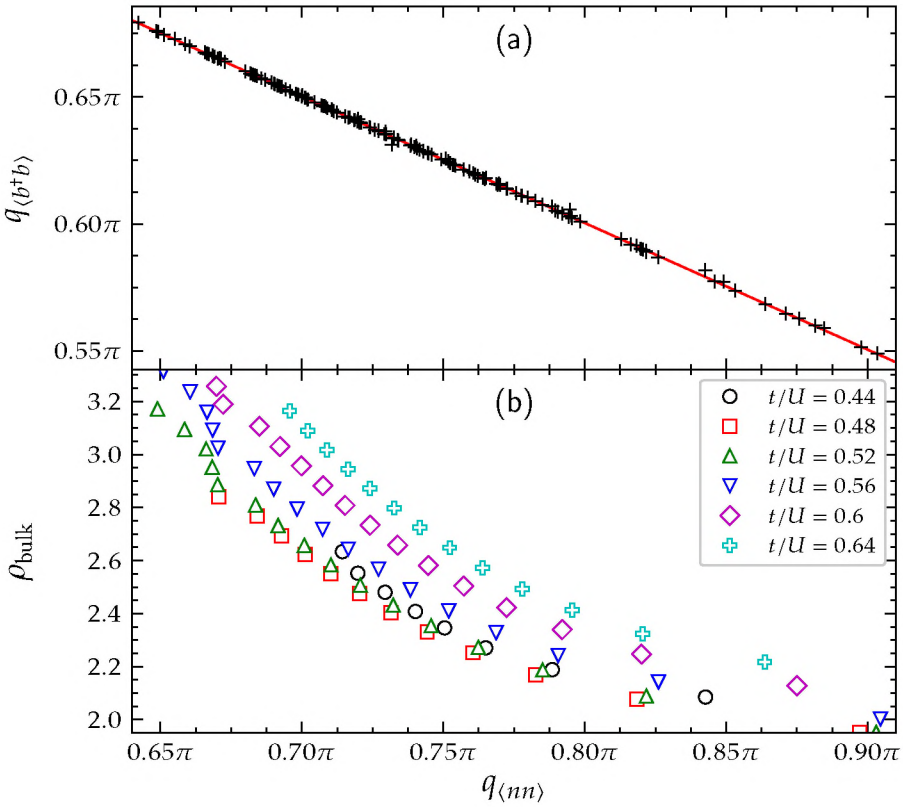

Figure 4.8: (a) black marks: collected values of qs showing a linear dependence (4.10), red line: linear regression $q_{\langle b^\dagger b\rangle} = 0.9991(6)\pi - 0.4984(7)q_{\langle nn\rangle}$. (b) relation between $q_{\langle nn\rangle}$ and ρ_{bulk} shown for different values of t/U.

it is also the location of the peak of the structure factor $S(q)$] and $q_{\langle b^\dagger b\rangle}$ for $C_{\text{DW}}(r)$. Examples of the fits of the SSD DMRG data to eqs. (4.6) to (4.9) are shown in Fig. 4.7.

A consideration of $q_{\langle nn\rangle}$ and $q_{\langle b^\dagger b\rangle}$ values obtained for multiple parameter sets corresponding to the domain of the IPSS phase reveals a simple relation between those two wavenumbers (see Fig. 4.8(a)):

$$q_{\langle b^\dagger b\rangle} = \pi - 0.5q_{\langle nn\rangle} \tag{4.10}$$

To further reinforce the claim that the wavenumbers $q_{\langle nn\rangle}$ and $q_{\langle b^\dagger b\rangle}$ are in fact irrational (unlike some other known cases of DW, e.g. and underdoped $\rho = 0.5$ DW where $q = 2\pi\rho$ [27]) we check how $q_{\langle nn\rangle}$ relates to the density and the Hamiltonian parameters [Fig. 4.8(b)] and conclude that there is no simple dependence of the wavenumber on the density.

4.4 Summary

We conducted a thorough analysis of a realistic (i.e. including next-nearest neighbor interactions and density-dependent tunnelings) extended Bose-Hubbard model using DMRG with up to $L = 400$ system sizes. We found that the phase diagram for $\rho = 1$ is qualitatively similar to the one obtained for standard EBHM, particularly the HI phase survives the inclusion of additional terms in the Hamiltonian and becomes even more pronounced for realistic, low values of dipolar interaction strength we considered, where additionally a suppression of SF

phase is observed. Moreover, strong dipolar interactions in the regime of high (> 1) densities give rise to pair-correlated phases — not only a pair-superfluid phase, but also additional pair-supersolid phases.

Especially interesting is a phase with incommensurate density wave order, to simulate which we resorted to an unorthodox DMRG method (i.e. sine square deformation DMRG), uncovering various characteristic properties of the ground state in the said phase. This phase, which is not present in the standard EBHM, is currently lacking a proper theoretical description explaining the aforementioned features. It is also unclear how this phase relates to other incommensurate DW phases, e.g. those found in spin systems [51, 62].

Conclusions

The idea of creating topological systems using optical lattices has generated much interest over the last few years. As experimental implementations face numerous challenges it is important to carefully examine the feasibility of proposed schemes. I believe the work presented in this thesis managed to fulfill this goal as I have shown, using reliable numerical methods, that the systems considered in Chapter 2 and Chapter 3 do have the postulated properties. Additionally, I have also established the domains of the relevant quantum phases, both in the context of aforementioned propositions and in the case of a generalization of EBH in Chapter 4, where the additional care was taken to be faithful to realistic physical parameters.

The analysis presented in Chapter 2 is constrained to small system sizes due to the memory requirements of the ED. While the problem of the validity of the obtained results has been addressed (in the form of the scaling of the boundaries with respect to the system size) it would be valuable to produce data for bigger system sizes, which would be possible using other numerical methods. Chapter 4 explores a rich landscape of phases enabled by the dipolar interactions in a realistically feasible experimental setup. Analyzing those of these phases, that are not present in a regular EBHM, in a more theoretical context could provide a clear description of how these complex phases emerge from additional terms added to EBH Hamiltonian.

DMRG method used extensively throughout the presented work is the de facto standard for one-dimensional quantum lattice calculations, however it is not devoid of biases and so a comparison with fundamentally different methods, like quantum Monte Carlo, would allow to better assess the correctness of the data. Using such methods would also make treatment in 2D possible, which is particularly important in the case of non-Abelian anyonic quasiparticles.

Appendix A

Exact diagonalization

Non-relativistic quantum mechanics are governed by the Schrödinger equation:

$$i\hbar\frac{\partial}{\partial t} = \hat{H}\,|\psi(t)\rangle\,, \tag{A.1}$$

where ψ and $\hat{H}$ are, respectively, the state of the system and the Hamiltonian representing some model used to describe that system. Equation (A.1) can be simplified if $\hat{H}$ is time independent. Then, the full solution boils down to finding the eigenvectors and the eigenvalues of $\hat{H}$, which correspond to stationary states in the system and their respective energies. For models in which the Hilbert space (which is spanned by all of the states of the system) is finite dimensional, $\hat{H}$ can be (after choosing orthogonal and complete basis) expressed as a matrix. This matrix, H, can be then diagonalized using standard algebraic tools.

Diagonalizing Hamiltonian matrix, other than being a natural method of solving small systems with only a few states (where it can be done by hand), turns out to be a popular choice for analyzing complicated systems with many body interactions which can not be solved analytically. This straightforward approach has severe limitations due to the fact that the size of a Hilbert space grows exponentially with the system size. For example, for Heisenberg model of L spin-$\frac{1}{2}$ particles, the size of the Hilbert space is 2^L – which for $L = 40$ is around 10^{12}, and is (after employing few tricks) the biggest size which can be exactly solved using present day computer technology. It is therefore hard to make precise predictions on the behavior of large systems based on the exact diagonalization alone. Due to the unbiased nature of this method, it is often used in conjunction with more efficient methods, which, however, rely on several approximations.

A.1 Basis creation

In order to uniquely determine Hamiltonian matrix, a basis needs to be chosen. There is, usually, a natural choice that depends on the model that is being considered and in the case of the BHM this natural choice is the Fock space. The basis vectors are chosen to be states with definite number of particles on each site, that is:

$$|n_1 n_2 \ldots n_L\rangle = (\hat{b}_1^\dagger)^{n_1}(\hat{b}_2^\dagger)^{n_2}\cdots(\hat{b}_L^\dagger)^{n_L}\,|0\rangle\,, \tag{A.2}$$

where n_i is the number of particles on i-th site, $\hat{b}_i$ is the creation operator on i^{th} site and $|0\rangle$ is the vacuum state.

In BHM the total number of particles (N) is conserved, and so this constraint must be taken into account when creating the basis. The simplest (and the fastest) solution is to just write L loops, where for i^{th} loop, if $i < L$ the variable n_i goes from 0 to $N_{\text{left}} = N - \sum_{j=1}^{i-1} n_j$, and $n_L = N_{\text{left}}$. While this method requires knowing in advance what L is, it can be generalized using recursion (with the depth of $L-1$). Another way to generate the basis is to create the states one-by-one using the following algorithm, which, given a state in the basis $\{n_i\}$, allows us to find the next one, $\{n'_i\}$[77]:

1. Find $k < L$, such that $n_k \neq 0$ and $n_i = 0$ for all $k < i < L$
2. $n'_i = \begin{cases} n_i, & i < k \\ n_k - 1, & i = k \\ N - \sum_{j=1}^{k} n_j + 1, & i = k+1 \\ 0, & i > k+1 \end{cases}$

Following this procedure beginning with state $|N00...0\rangle$ we get all of the states.

The procedure described above can be modified for the cases, where there is a set limit on the number of particles occupying each site ($N_{\max}$):

1. Find L' such that $n_j = N_{\max}$ for all $L' < j \leq L$.
2. Find $k < L$, such that $n_k \neq 0$ and $n_i = 0$ for all $k < i < L'$.
3. Let $N_k \equiv N - \sum_{j=1}^{k} + 1$ and $l \equiv k + 1 + \lfloor (N_k)/N_{\max} \rfloor$.
4. $n'_i = \begin{cases} n_i, & i < k \\ n_k - 1, & i = k \\ N_{\max}, & k+1 \leq i < l \\ N_k \bmod N_{\max}, & i = l \\ 0, & i > l \end{cases}$

A.2 Hamiltonian symmetries

As the Hilbert space grows exponentially with system size, it is important to make use of underlying symmetries of the Hamiltonian in order to reduce the memory requirements. If such symmetries exist, it is possible to introduce a basis in which the Hamiltonian matrix has a block diagonal form, each block corresponding to some conserved quantity. This of course reduces the memory and processing power requirements, as each block can be diagonalized separately, while also having a reduced dimensionality.

One of the most common symmetries is a translational symmetry in a lattice with periodic boundary conditions (PBC), that is $[\hat{H}, \hat{T}] = 0$ with $\hat{T}$ being the operator translating state by one lattice site. A conserved quantity introduced by this symmetry is the total quasi-momentum, k, and the associated basis states are (for a 1D lattice of length L):

$$|a(k)\rangle \equiv \frac{1}{\sqrt{N_a}} \sum_{r=0}^{L-1} e^{-ikr} \hat{T}^r |a\rangle , \tag{A.3}$$

where $|a\rangle$ is some state from the Fock basis and $k = m\ 2\pi/L$, $m = -L/2 + 1, ...L/2$. All translations of $|a\rangle$ correspond to the same $|a(k)\rangle$ states. The value of the normalization constant is $N_a = N^2/R_a$, where R_a is the smallest non-negative integer such that $\hat{T}^{R_a}|a\rangle = |a\rangle$. The definition (A.3) produces valid states only if $kR_a/(2\pi) \in \mathbb{Z}$.

This basis can be stored as a representative Fock basis vectors $|a\rangle$, such that $|a\rangle$ is the smallest (in the context of some order imposed on all Fock basis vectors) among the states for which (A.3) holds. The generation is similar to the one presented in the preceding section, but at each step one must check whether the currently considered state corresponds to a new $|a(k)\rangle$ by finding the smallest translation (that is, a representative) and seeing if it is already stored in the basis.

A.3 Matrix creation and diagonalization

In order to create the Hamiltonian matrix, $H_{ij} = \langle i|\hat{H}|j\rangle$ (here, i and j, correspond to the i^{th} and j^{th} states of the chosen basis), one could in principle iterate over both i and j, calculating H_{ij} directly. It is, however, computationally costly (scaling as the Hilbert space dimension squared, d_H^2) and a much better alternative is to do a single iteration over the basis states and for each of these calculate every possible $\hat{H}|i\rangle$ term by term. Furthermore, as the number of terms (in the usual models) scale linearly with the size of the system, the resulting Hamiltonian matrix will be sparse and so it may be stored efficiently (only non-zero terms have to be stored). Having some $|\phi\rangle$ obtained as a step of this iteration:

$$\hat{H}|i\rangle = h_{i,\phi}|\phi\rangle + ... \tag{A.4}$$

we then must find what is the position of this vector in the basis (find j, such that $|j\rangle = |\phi\rangle$). One of the simplest way is to have the basis vectors ordered (using some hash function, or simply by storing the vectors in such a way, that we can compare them, e.g. by doing a lexicographic comparison between Fock states' occupation numbers) and then use a binary search on this ordered set (which takes on average $\sim \log_2(d_H)$ steps).

The method described above is simple for BHM with a Fock basis, but for some other bases and their representations (such as the quasi-momentum basis $|a(k)\rangle$) calculationg H_{ij} is not as straightforward. If we use the quasi-momentum basis, $|a(k)\rangle$, and store the basis states as the representative Fock space states (see the previous section), calculating (A.4) ($|a\rangle \equiv |i\rangle$ will be used, where $|a\rangle$ is the representative of $|a(k)\rangle$) is only the first step. The $|\phi\rangle$ is not necessary a representative state itself, which we may denote as $|b\rangle = \hat{T}^l|\phi\rangle$. Knowing l and using (A.3) we finally arrive at the value of the matrix element in the quasi-momentum basis:

$$\langle b(k)|\hat{H}_{i,\phi}|a(k)\rangle = h_{i,\phi}e^{-ikl}\sqrt{N_b/N_a}, \tag{A.5}$$

where the indices of $\hat{H}_{i,\phi}$ are there to point out that (A.5) is only a part of the full term $\langle b(k)|\hat{H}|a(k)\rangle$, which is a sum of all $\langle b(k)|\hat{H}_{i,\phi}|a(k)\rangle$ such that $|\phi\rangle$ is a translation of $|b\rangle$.

As the Hilbert space of the problem is very large, the diagonalization can not be complete (in a reasonable time) and one must resort to algorithms that provide only a handful of eigenvectors/eigenvalues (examples of such methods are Lanczos method and Arnoldi method). Many implementations of these can be easily found in the form of libraries available for multiple programming languages (one of such libraries is ARPACK). The eigenvectors found using

ED provide a full picture of an underlying quantum states and so it is possible to calculate any quantum mechanical quantity.

Appendix B

Density Matrix Renormalization Group

In this appendix the DMRG method will be presented. Instead of a rigorous, complete description, the focus will be on the applications of this method in the works presented as a part of this thesis. The DMRG used in these works has been based on the ITensor library [40]. More details on the method can be found in the vast literature on the subject, which contains some excellent reviews (such as [60]).

B.1 Matrix product states formalism

In general, quantum state of the lattice of L sites, where the state on the i^{th} site is spanned spanned by the local d-dimensional basis σ_i, can be written as:

$$|\psi\rangle = \sum_{\sigma_1,\ldots,\sigma_L} c_{\sigma_1,\ldots,\sigma_L} |\sigma_1,\ldots,\sigma_L\rangle\,. \tag{B.1}$$

Equation (B.1) can be rewritten in the following form, named matrix product state(MPS):

$$|\psi\rangle = \sum_{\sigma_1,\ldots,\sigma_L} M_1^{\sigma_1} M_2^{\sigma_2} \cdots M_L^{\sigma_L} |\sigma_1,\ldots,\sigma_L\rangle\,, \tag{B.2}$$

where M^{σ_i} is a matrix of dimensions $d_{i-1} \times d_i$ (assuming the form (B.2), we must set $d_0 = d_L = 1$ for the matrix multiplication to be a scalar, making $M_1^{\sigma_1}$ and $M_L^{\sigma_L}$ effectively vectors).

(B.2) can be used to describe any kind of state, but the dimensions d_i of the matrices grow exponentially with system size (for even L, $d_i = d^{\min(i,L-i)}$). Fortunately, the relevant class of states, that is ground (and other low-lying) states of short-range Hamiltonians in 1D, can be effectively approximated by matrices of dimensions $d_i \leq \chi$, where χ (called the bond dimension) is in practice between 100 and 1000 (for lattices containing hundreds of sites). The approximation can be done directly on the lattices through singular value decomposition (SVD): every matrix M of dimensions $N_A \times N_B$ can be decomposed: $M = USV^\dagger$ in such a way, that $U^\dagger U = I$, $V^\dagger V = I$ and S is a square diagonal matrix of dimension $\min(N_A, N_B)$, which elements, called singular values, are non-negative. Reducing the dimensionality of M can be then done by discarding the smallest singular values.

The MPS representation is not unique, as for any invertible matrix X one can make a transformation of neighboring matrices: $M_i^{\sigma_i} \to M_i^{\sigma_i} X$ and $M_{i+1}^{\sigma_{i+1}} \to X^{-1} M_{i+1}^{\sigma_{i+1}}$ without changing the resulting state $|\psi\rangle$. This gauge freedom can be used to impose some convenient properties on the matrices $M_i^{\sigma_i}$, the most important of which are:

$$\sum_{\sigma_i} (M_i^{\sigma_i})^\dagger M_i^{\sigma_i} = I, \qquad \text{left-normalization} \tag{B.3}$$

$$\sum_{\sigma_i} M_i^{\sigma_i} (M_i^{\sigma_i})^\dagger = I, \qquad \text{right-normalization.} \tag{B.4}$$

Let us denote left-normalized matrices by $A_i^{\sigma_i}$ and right-normalized by $B_i^{\sigma_i}$. Then, we can decompose $|\psi\rangle$ into so-called mixed-canonical form as (the detailed scheme of arriving at this decomposition can be found in [60]):

$$|\psi\rangle = \sum_{\sigma_1,\ldots,\sigma_L} A_1^{\sigma_1} \cdots A_i^{\sigma_i} S B_{i+1}^{\sigma_{i+1}} \cdots B_L^{\sigma_L} |\sigma_1, \ldots, \sigma_L\rangle, \tag{B.5}$$

where S is a diagonal matrix of singular values obtained through SVD. This form can significantly simplify the calculations in which MPS is used (see Fig. B.1).

Similarly to MPS, we can define any operator, the Hamiltonian in particular, as a product of local matrices:

$$\hat{H} = \sum_{\sigma_1,\ldots,\sigma_L} W_1^{\sigma_1,\sigma_1'} \cdots W_L^{\sigma_L,\sigma_L'} |\sigma_1, \ldots, \sigma_L\rangle \langle \sigma_1, \ldots, \sigma_L|. \tag{B.6}$$

There exist a few recipes as well as automated tools (such as AutoMPO included with ITensor) for transforming given classes of Hamiltonians into MPS form. The matrices $M_i^{\sigma_i}$ and $W_i^{\sigma_i,\sigma_i'}$ can be thought of as tensors of rank 3 and 4 respectively. σ_i and σ_i' indices are referred to as physical indices, while the matrix indices of Ms and Ws matrices are link/dummy indices. This picture allows easy pictorial representation of MPS and MPO operations, example of which is presented in Fig. B.1.

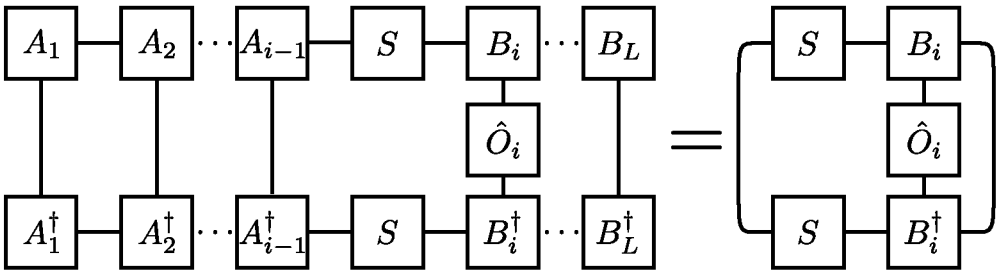

Figure B.1: Graphical representation of calculating the value of a single site operator, $\langle\psi|\hat{O}_i|\psi\rangle$ for $|\psi\rangle$ given by (B.5). Horizontal lines correspond to matrix multiplication, while vertical lines to the summation over possible local physical states, σ_i (both kinds of lines correspond to tensor contractions of tensor forms A_i and B_i). The form on the left of this figure is equivalent to the one on the right, as the properties (B.3) and (B.4) can be used to transform multiple contractions into an identity (a line).

B.2 DMRG Algorithm

The first step of the algorithm is to prepare an initial MPS. The simplest approaches are to simply take a random state (which for Bose-Hubbard models may be from Fock basis) or choose one resembling the final state (such as a DW state in the DW phase), in which case one must be careful, as the DMRG may become stuck in the local minimum. If some quantity (e.g. particle number) is conserved by the Hamiltonian, the initial MPS sets its value.

To find the ground state, instead of trying to diagonalize the whole $\hat{H}$ at once (which, while possible using MPO and MPS formalism, would still require resources comparable to full exact diagonalization), one can minimize the energy site-by-site. This is done by updating only one or just a few matrices $M_i^{\sigma_i}$ at a time (here, the matrices of sites i and $i+1$ were being updated in each minimization step). In order to do this local minimization, the non-variable parts of the Hamiltonian MPO and current trial MPS have to be contracted (which can be done efficiently if the MPS is in the mixed-canonical form (B.5) [60]), leaving only the indices of the local matrices. These indices can be combined in order to cast this problem in the form of a regular eigenequation, to which standard diagonalization methods (such as Jacobi-Davidson or Lanczos) can be applied.

The procedure described above is applied step-by-step to the MPS sites, from one end of the lattice to the other one and then back to the starting point. Each local minimization done throughout these so-called sweeps is followed by SVD decomposition, which at the same time ensures the correct mixed-canonical form and allows discarding the smallest singular values to keep the dimensions of MPS matrices below the required level. That is, the diagonalization and SVD steps done for i and $i+1$ site during j^{th} sweep (left-to-right, iterating i from 1 to $L-1$) change the tensors in a following way:

$$\begin{aligned}
&\cdots\ A_{i-1,j}\ \ M_{i,j-1}\ \ B_{i+1,j-1}\ \ B_{i+2,j-1}\ \ \cdots\\
\xrightarrow{\text{diag}}\ &\cdots\ A_{i-1,j}\ \ M'_{i,j-1}\ \ M'_{i+1,j-1}\ \ B_{i+2,j-1}\ \ \cdots\\
\xrightarrow{\text{SVD}}\ &\cdots\ A_{i-1,j}\ \ A_{i,j}\ \ M_{i+1,j-1}\ \ B_{i+2,j-1}\ \ \cdots,
\end{aligned}$$

where the first index denotes the site, second how many sweeps were done already, A are left-normalized matrices, B are right normalized matrices and M are matrices without any normalization properties imposed, primed matrices are the results of diagonalization procedure (matrices without primes are the results of SVD and approximation). The starting point is $M_{1,0}B_{2,0}B_{3,0}\cdots B_{L,0}$, the left-to-right sweeps end at $A_{1,1}\cdots A_{L-1,1}M_{L,1}$. The procedure for right-to-left sweep is analogous to the one described in (B.2) (matrices on the sites i and $i+1$ go from $A_{i,j}M_{i+1,j}$ to $M_{i,j}B_{i+1,j+1}$).

The sweeps are done until the energy converges to a stable value with a given accuracy (or until any other chosen criterion is met). The energy of the MPS updated using the DMRG procedure must necessarily be lowered (or stay the same) after each step, this does not, however, guarantee that the correct ground state is ever reached (as a consequence of using only local updates to the MPS state).

B.3 Sine-square deformation

The DMRG is the most efficient for open boundary conditions. These boundary conditions, however, introduce strong boundary effects (e.g. in the form of Friedel oscillations [72]) which effectively increase the system size necessary to obtain precise bulk properties of the system. It

is therefore advantageous to use methods which simulate PBC in system with OBC and with that goal in mind multiple smooth-edge DMRG variations were introduced, each of which consists of applying a smooth envelope to the Hamiltonian, such that the Hamiltonian stays approximately the same in the middle of the lattice and decays to 0 towards the edges.

One of such variations is the so-called sine-square deformation (SSD), wherein the envelope is the sine-square function [37]. If we denote by $\hat{H}_{i,i} \equiv \hat{H}_i$ all the terms acting on a single site i and by $\hat{H}_{i,i+j}$ all the terms of the Hamiltonian acting on sites i and $i+j$, then the SSD Hamiltonian has the form:

$$\hat{H}_{\mathrm{SSD}} = \sum_{j=0}^{r} \sum_{i=1}^{L-j} f_{i,j} H_{i,i+j}, \tag{B.7}$$

where r is the maximum range of the Hamiltonian terms (e.g. $r = 1$ for BHM and $r = 2$ for EBHM), and the envelope function $f(i,j)$ is:

$$f(i,j) = \sin^2\left[\frac{\pi}{L}\left(i + \frac{j-1}{2}\right)\right]. \tag{B.8}$$

The SSD DMRG, apart from being able to simulate PBC with OBC, allows for non-conservation of quantities otherwise conserved by the Hamiltonian. In the case of Bose-Hubbard model, this allows us to simulate the system in grand canonical ensemble-like situation[39], wherein the particles/holes on the edges of the lattice provide only negligible energy addition, and thus the edges function as a particle reservoir for the middle part of the lattice (which correspond to the bulk properties of the system). To control the density of the particles, one must then use the chemical potential term, $-\mu \sum_i \hat{n}_i$ (without any deformation of the particle-conserving Hamiltonian, this term only shifts the total energy and may be discarded). This method has an additional advantage when dealing with phases, where the density is incommensurate with respect to the lattice site (such as the IPSS phase from Chapter 4) — the number of particles does not have to be an integer (in contrast to the regular DMRG).

Bibliography

[1] Y. Aharonov and D. Bohm, "Significance of Electromagnetic Potentials in the Quantum Theory," Phys. Rev. **115**, 485–491 (1959).

[2] K. Aikawa, A. Frisch, M. Mark, S. Baier, A. Rietzler, R. Grimm, and F. Ferlaino, "Bose-Einstein Condensation of Erbium," Phys. Rev. Lett. **108**, 210401 (2012).

[3] J. Alicea, Y. Oreg, G. Refael, F. von Oppen, and M. P. A. Fisher, "Non-Abelian statistics and topological quantum information processing in 1D wire networks," Nature Physics **7**, 412–417 (2011).

[4] P. W. Anderson, "Absence of Diffusion in Certain Random Lattices," Phys. Rev. **109**, 1492–1505 (1958).

[5] E. Ardonne, E. J. Bergholtz, J. Kailasvuori, and E. Wikberg, "Degeneracy of non-Abelian quantum Hall states on the torus: domain walls and conformal field theory," Journal of Statistical Mechanics: Theory and Experiment **2008**, P04016 (2008).

[6] N. W. Ashcroft and N. D. Mermin, *Solid state physics* (Saunders College, 1976).

[7] M. Atala, M. Aidelsburger, J. T. Barreiro, D. Abanin, T. Kitagawa, E. Demler, and I. Bloch, "Direct measurement of the Zak phase in topological Bloch bands," Nature Physics **9**, 795–800 (2013).

[8] S. Baier, M. J. Mark, D. Petter, K. Aikawa, L. Chomaz, Z. Cai, M. Baranov, P. Zoller, and F. Ferlaino, "Extended Bose-Hubbard models with ultracold magnetic atoms," Science **352**, 201–205 (2016).

[9] G. G. Batrouni, V. G. Rousseau, R. T. Scalettar, and B. Grémaud, "Competing phases, phase separation, and coexistence in the extended one-dimensional bosonic Hubbard model," Phys. Rev. B **90**, 205123 (2014).

[10] M. V. Berry, "Quantal Phase Factors Accompanying Adiabatic Changes," Proceedings of the Royal Society of London. Series A, Mathematical and Physical Sciences **392**, 45–57 (1984).

[11] K. Biedroń, O. Dutta, and J. Zakrzewski, "Topological Rice-Mele model in an emergent lattice: Exact diagonalization approach," Phys. Rev. A **93**, 033631 (2016).

[12] K. Biedroń, M. Łącki, and J. Zakrzewski, "Extended Bose-Hubbard model with dipolar and contact interactions," Phys. Rev. B **97**, 245102 (2018).

[13] I. Bloch, J. Dalibard, and W. Zwerger, "Many-body physics with ultracold gases," Rev. Mod. Phys. **80**, 885–964 (2008).

[14] P. Calabrese and J. Cardy, "Entanglement entropy and quantum field theory," Journal of Statistical Mechanics: Theory and Experiment **2004**, P06002 (2004).

[15] C. Chin, R. Grimm, P. Julienne, and E. Tiesinga, "Feshbach resonances in ultracold gases," Rev. Mod. Phys. **82**, 1225–1286 (2010).

[16] L. Chomaz, R. M. W. van Bijnen, D. Petter, G. Faraoni, S. Baier, J. H. Becher, M. J. Mark, F. Wächtler, L. Santos, and F. Ferlaino, "Observation of roton mode population in a dipolar quantum gas," Nature Physics **14**, 442–446 (2018).

[17] E. G. Dalla Torre, E. Berg, and E. Altman, "Hidden Order in 1D Bose Insulators," Phys. Rev. Lett. **97**, 260401 (2006).

[18] B. Damski, "Fidelity susceptibility of the quantum Ising model in a transverse field: The exact solution," Phys. Rev. E **87**, 052131 (2013).

[19] C. Davisson and L. H. Germer, "Diffraction of Electrons by a Crystal of Nickel," Phys. Rev. **30**, 705–740 (1927).

[20] T. Đurić, K. Biedroń, and J. Zakrzewski, "Fibonacci anyon excitations of one-dimensional dipolar lattice bosons," Phys. Rev. B **95**, 085102 (2017).

[21] O. Dutta, M. Gajda, P. Hauke, M. Lewenstein, D.-S. Lühmann, B. A. Malomed, T. Sowiński, and J. Zakrzewski, "Non-standard Hubbard models in optical lattices: a review," Reports on Progress in Physics **78**, 066001 (2015).

[22] R. P. Feynman, "Simulating physics with computers," International journal of theoretical physics **21**, 467–488 (1982).

[23] M. P. A. Fisher, P. B. Weichman, G. Grinstein, and D. S. Fisher, "Boson localization and the superfluid-insulator transition," Phys. Rev. B **40**, 546–570 (1989).

[24] M. Freedman, A. Kitaev, M. Larsen, and Z. Wang, "Topological quantum computation," Bulletin of the American Mathematical Society **40**, 31–38 (2003).

[25] L. Fu and C. L. Kane, "Superconducting Proximity Effect and Majorana Fermions at the Surface of a Topological Insulator," Phys. Rev. Lett. **100**, 096407 (2008).

[26] M. Greiner, O. Mandel, T. Esslinger, T. W. Hänsch, and I. Bloch, "Quantum phase transition from a superfluid to a Mott insulator in a gas of ultracold atoms," Nature **415**, 39–44 (2002).

[27] B. Grémaud and G. G. Batrouni, "Excitation and dynamics in the extended Bose-Hubbard model," Phys. Rev. B **93**, 035108 (2016).

[28] A. Griesmaier, J. Werner, S. Hensler, J. Stuhler, and T. Pfau, "Bose-Einstein Condensation of Chromium," Phys. Rev. Lett. **94**, 160401 (2005).

[29] R. Grimm, M. Weidemüller, and Y. B. Ovchinnikov, "Optical Dipole Traps for Neutral Atoms," in *Advances in atomic, molecular, and optical physics*, Vol. 42, edited by B. Bederson and H. Walther (Academic Press, 2000), pp. 95–170.

[30] S.-J. Gu, H.-M. Kwok, W.-Q. Ning, and H.-Q. Lin, "Fidelity susceptibility, scaling, and universality in quantum critical phenomena," Phys. Rev. B **77**, 245109 (2008).

[31] Z.-C. Gu and X.-G. Wen, "Tensor-entanglement-filtering renormalization approach and symmetry-protected topological order," Phys. Rev. B **80**, 155131 (2009).

[32] F. D. M. Haldane, "Continuum dynamics of the 1-D Heisenberg antiferromagnet: Identification with the O(3) nonlinear sigma model," Physics Letters A **93**, 464–468 (1983).

[33] F. D. M. Haldane, "Effective Harmonic-Fluid Approach to Low-Energy Properties of One-Dimensional Quantum Fluids," Phys. Rev. Lett. **47**, 1840–1843 (1981).

[34] F. D. M. Haldane, "Nonlinear Field Theory of Large-Spin Heisenberg Antiferromagnets: Semiclassically Quantized Solitons of the One-Dimensional Easy-Axis Néel State," Phys. Rev. Lett. **50**, 1153–1156 (1983).

[35] M. Z. Hasan and C. L. Kane, "Colloquium: Topological insulators," Rev. Mod. Phys. **82**, 3045–3067 (2010).

[36] Y. Hatsugai, "Chern number and edge states in the integer quantum Hall effect," Phys. Rev. Lett. **71**, 3697–3700 (1993).

[37] T. Hikihara and T. Nishino, "Connecting distant ends of one-dimensional critical systems by a sine-square deformation," Phys. Rev. B **83**, 060414 (2011).

[38] C. Holzhey, F. Larsen, and F. Wilczek, "Geometric and renormalized entropy in conformal field theory," Nuclear Physics B **424**, 443–467 (1994).

[39] C. Hotta and N. Shibata, "Grand canonical finite-size numerical approaches: A route to measuring bulk properties in an applied field," Phys. Rev. B **86**, 041108 (2012).

[40] ITensor, *Itensor library*, `http://itensor.org`.

[41] D. Jaksch and P. Zoller, "The cold atom Hubbard toolbox," Annals of Physics **315**, Special Issue, 52–79 (2005).

[42] A. Y. Kitaev, "Fault-tolerant quantum computation by anyons," Annals of Physics **303**, 2–30 (2003).

[43] A. Y. Kitaev, "Unpaired Majorana fermions in quantum wires," Physics-Uspekhi **44**, 131–136 (2001).

[44] K. v. Klitzing, G. Dorda, and M. Pepper, "New Method for High-Accuracy Determination of the Fine-Structure Constant Based on Quantized Hall Resistance," Phys. Rev. Lett. **45**, 494–497 (1980).

[45] T. D. Kühner and H. Monien, "Phases of the one-dimensional Bose-Hubbard model," Phys. Rev. B **58**, R14741–R14744 (1998).

[46] T. D. Kühner, S. R. White, and H. Monien, "One-dimensional Bose-Hubbard model with nearest-neighbor interaction," Phys. Rev. B **61**, 12474–12489 (2000).

[47] R. B. Laughlin, "Anomalous Quantum Hall Effect: An Incompressible Quantum Fluid with Fractionally Charged Excitations," Phys. Rev. Lett. **50**, 1395–1398 (1983).

[48] M. Lewenstein, A. Sanpera, and V. Ahufinger, *Ultracold Atoms in Optical Lattices: Simulating quantum many-body systems* (Oxford University Press, Oxford, 2012).

[49] M. Lu, N. Q. Burdick, S. H. Youn, and B. L. Lev, "Strongly Dipolar Bose-Einstein Condensate of Dysprosium," Phys. Rev. Lett. **107**, 190401 (2011).

[50] E. Lucioni, L. Tanzi, A. Fregosi, J. Catani, S. Gozzini, M. Inguscio, A. Fioretti, C. Gabbanini, and G. Modugno, "Dysprosium dipolar Bose-Einstein condensate with broad Feshbach resonances," Phys. Rev. A **97**, 060701 (2018).

[51] T. Murashima, K. Hijii, K. Nomura, and T. Tonegawa, "Phase Diagram of $S = 1$ XXZ Chain with Next-Nearest-Neighbor Interaction," Journal of the Physical Society of Japan **74**, 1544–1551 (2005).

[52] C. Nayak, S. H. Simon, A. Stern, M. Freedman, and S. Das Sarma, "Non-Abelian anyons and topological quantum computation," Rev. Mod. Phys. **80**, 1083–1159 (2008).

[53] S. Nishimoto, "Tomonaga-Luttinger-liquid criticality: Numerical entanglement entropy approach," Phys. Rev. B **84**, 195108 (2011).

[54] R. Orús, "A practical introduction to tensor networks: Matrix product states and projected entangled pair states," Annals of Physics **349**, 117–158 (2014).

[55] B. Paredes, "Non-Abelian fractional quantum Hall states for hard-core bosons in one dimension," Phys. Rev. B **85**, 195150 (2012).

[56] A. Przysiężna, O. Dutta, and J. Zakrzewski, "Rice–Mele model with topological solitons in an optical lattice," New Journal of Physics **17**, 013018 (2015).

[57] D. Rossini and R. Fazio, "Phase diagram of the extended Bose–Hubbard model," New Journal of Physics **14**, 065012 (2012).

[58] S. Sachdev, *Quantum Phase Transitions* (Cambridge University Press, Apr. 2011).

[59] V. W. Scarola and S. Das Sarma, "Quantum Phases of the Extended Bose-Hubbard Hamiltonian: Possibility of a Supersolid State of Cold Atoms in Optical Lattices," Phys. Rev. Lett. **95**, 033003 (2005).

[60] U. Schollwöck, "The density-matrix renormalization group in the age of matrix product states," Annals of Physics **326**, January 2011 Special Issue, 96–192 (2011).

[61] J. K. Slingerland and F. A. Bais, "Quantum groups and non-Abelian braiding in quantum Hall systems," Nuclear Physics B **612**, 229–290 (2001).

[62] Z. G. Soos, A. Parvej, and M. Kumar, "Numerical study of incommensurate and decoupled phases of spin-1/2 chains with isotropic exchange J_1, J_2 between first and second neighbors," Journal of Physics: Condensed Matter **28**, 175603 (2016).

[63] T. Sowiński, O. Dutta, P. Hauke, L. Tagliacozzo, and M. Lewenstein, "Dipolar Molecules in Optical Lattices," Phys. Rev. Lett. **108**, 115301 (2012).

[64] G. Sun, A. K. Kolezhuk, and T. Vekua, "Fidelity at Berezinskii-Kosterlitz-Thouless quantum phase transitions," Phys. Rev. B **91**, 014418 (2015).

[65] D. J. Thouless, M. Kohmoto, M. P. Nightingale, and M. den Nijs, "Quantized Hall Conductance in a Two-Dimensional Periodic Potential," Phys. Rev. Lett. **49**, 405–408 (1982).

[66] S. Trebst, M. Troyer, Z. Wang, and A. W. W. Ludwig, "A Short Introduction to Fibonacci Anyon Models," Progress of Theoretical Physics Supplement **176**, 384–407 (2008).

[67] D. C. Tsui, H. L. Stormer, and A. C. Gossard, "Two-Dimensional Magnetotransport in the Extreme Quantum Limit," Phys. Rev. Lett. **48**, 1559–1562 (1982).

[68] A. Vaezi and M. Barkeshli, "Fibonacci Anyons From Abelian Bilayer Quantum Hall States," Phys. Rev. Lett. **113**, 236804 (2014).

[69] V. Vedral, "The role of relative entropy in quantum information theory," Rev. Mod. Phys. **74**, 197–234 (2002).

[70] G. Vidal, J. I. Latorre, E. Rico, and A. Y. Kitaev, "Entanglement in Quantum Critical Phenomena," Phys. Rev. Lett. **90**, 227902 (2003).

[71] X.-G. Wen, "Topological orders and edge excitations in fractional quantum Hall states," Advances in Physics **44**, 405–473 (1995).

[72] S. R. White, I. Affleck, and D. J. Scalapino, "Friedel oscillations and charge density waves in chains and ladders," Phys. Rev. B **65**, 165122 (2002).

[73] E. Wikberg, J. Larson, E. J. Bergholtz, and A. Karlhede, "Fractional domain walls from on-site softening in dipolar bosons," Phys. Rev. A **85**, 033607 (2012).

[74] W.-L. You, Y.-W. Li, and S.-J. Gu, "Fidelity, dynamic structure factor, and susceptibility in critical phenomena," Phys. Rev. E **76**, 022101 (2007).

[75] J. Zak, "Berry's phase for energy bands in solids," Phys. Rev. Lett. **62**, 2747–2750 (1989).

[76] P. Zanardi and N. Paunković, "Ground state overlap and quantum phase transitions," Phys. Rev. E **74**, 031123 (2006).

[77] J. M. Zhang and R. X. Dong, "Exact diagonalization: the Bose–Hubbard model as an example," European Journal of Physics **31**, 591 (2010).

Author's publications

Topological Rice-Mele model in an emergent lattice: Exact diagonalization approach

Krzysztof Biedroń,[1] Omjyoti Dutta,[1] and Jakub Zakrzewski[1,2]
[1]*Instytut Fizyki imienia Mariana Smoluchowskiego, Uniwersytet Jagielloński, Łojasiewicza 11, 30-048 Kraków, Poland*
[2]*Mark Kac Complex Systems Research Center, Jagiellonian University, Łojasiewicza 11, 30-348 Kraków, Poland*
(Received 30 September 2015; published 16 March 2016)

Using exact diagonalization methods we study possible phases in a one-dimensional model of two differently populated fermionic species in a periodically driven optical lattice. The shaking amplitude and frequency are chosen to resonantly drive s-p transition while minimizing the standard intraband tunnelings. We verify numerically the presence of an emergent density wave configuration of composites for appropriate filling fraction and minimized intraband tunnelings. The majority fermions moving in such a lattice mimic the celebrated Rice-Mele model. Far away from that region, the structure changes to a clustered phase, with the intermediate phase abundantly populated by defects of the density wave. These defects lead to localized modes carrying fractional particle charge. The results obtained are compared with earlier approximate predictions.

DOI: 10.1103/PhysRevA.93.033631

I. INTRODUCTION

Ultracold atoms trapped in optical lattices provide systems characterized by an unprecedented control over various parameters, enabling a simulation of a wide array of exotic solid-state models. One example of such phenomena are topological insulators [1,2], which are of particular interest in the field of quantum information and spintronics due to their inherent stability and transport properties [3–5]. Lattices hosting systems showing topological properties have been realized experimentally, both for two-dimensional (2D) [6–11] and one-dimensional (1D) models (e.g., Su-Schrieffer-Heeger [12] and Rice-Mele [13] dimer models in Ref. [14] or Thouless pump in Refs. [15,16]). Optical lattices by themselves do not allow for generation of impurities on which boundary localized modes may appear—the lattices are necessarily perfect. In two dimensions, the localized defect—a vortex—may be created by a vortex wave [17,18] leading to a well-placed dislocation. In one dimension, the situation is not so simple, but a recent proposition [19] suggests that topologically nontrivial states may emerge in systems consisting of two subspecies of strongly attracting fermions. There, the topological structure is not encoded in the underlying lattice geometry, but rather is an emergent feature arising from atomic interactions, enabling creation of defects with less constraints. For high enough values of the interaction strength, fermions of different species tend to bind together forming composites, and if there is some imbalance in a number of atoms of both species, excess fermions stay unbound. To extract essential properties of the system, one has to take into account higher bands (p band at least, as in the model studied below) and the effects of strong interactions, such as the density-induced tunnelings [20–23]. The lattice shaking is employed with the shaking frequency such that the interband density-induced s to p tunneling is resonantly enhanced. As a result, in a 1D chain, the emergent system is proposed to be described by the Rice-Mele model [20]. For a triangular lattice geometry, similar processes lead to the creation of synthetic non-Abelian fields in an emergent dice lattice [24].

Let us note, parenthetically, that physics of p-orbital fermions is very rich, leading to a possible creation of Fulde-Ferrell-Larkin-Ovchinnikov (FFLO) states [25] as well as density stripes at appropriate fillings due to nested Fermi surfaces [26,27] even in the absence of any periodic driving (for a review of these effects see [28]). Those systems were studied using both two- and three-dimensional models. Here, we shall restrict ourselves to small 1D systems amenable to exact diagonalization.

Let us stress that the main approximation used in periodically driven models discussed in Refs. [20,24] is to neglect the tunneling of the minority components. As a result, one generates a modified Falicov-Kimball-like model with immobile composites (made out of strongly coupled pair of fermions) and mobile excess fermions. We test this assumption in the present paper. Namely, we are employing an exact diagonalization method to the system described in Ref. [20] in order to assess the validity of the results presented there. The fidelity and structure factor analysis allow us to classify the ground states for different values of parameters. We consider also explicitly possible configurations with a given number of defects.

II. SYSTEM

The system considered is a mixture of two species of unequally populated, strongly attractively interacting fermions in a 1D periodically shaken optical lattice. The Hamiltonian of the system is [20] $\hat{H} = \hat{H}_{\rm tun} + \hat{H}_{\rm dit} + \hat{H}_{\rm ons} + \hat{H}_{\rm sh}(t)$, where:

$$\begin{aligned}
\hat{H}_{\rm tun} &= -J_0 \sum_{\langle ij\rangle} [\hat{s}_i^\dagger \hat{s}_j + \hat{s}_{\uparrow i}^\dagger \hat{s}_{\uparrow j}] + J_1 \sum_{\langle ij\rangle} \hat{p}_i^\dagger \hat{p}_j, \\
\hat{H}_{\rm dit} &= \sum_{\langle ij\rangle} [T_0 \hat{s}_{\uparrow i}^\dagger (\hat{n}_i + \hat{n}_j)\hat{s}_{\uparrow j} + T_1 \hat{p}_i^\dagger (\hat{n}_i^\uparrow + \hat{n}_j^\uparrow)\hat{p}_j \\
&\quad + T_{01}((j-i)\hat{p}_i^\dagger \hat{n}_i^\uparrow \hat{s}_j + \text{H.c.})], \\
\hat{H}_{\rm ons} &= U_0 \sum_i \hat{n}_i^\uparrow \hat{n}_i + U_1 \sum_i \hat{p}_i^\dagger \hat{p}_i \hat{n}_i^\uparrow + E_1 \sum_i \hat{p}_i^\dagger \hat{p}_i, \\
\hat{H}_{\rm sh}(t) &= K \cos\omega t \sum_j j(\hat{n}_j^\uparrow + \hat{s}_j^\dagger \hat{s}_j + \hat{p}_j^\dagger \hat{p}_j) \\
&\quad + \delta E_1 \cos(\omega t + \varphi) \sum_i \hat{p}_i^\dagger \hat{p}_i . \qquad (1)
\end{aligned}$$

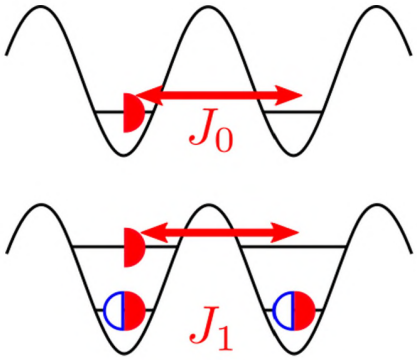

FIG. 1. Visualization of the kinetic tunneling processes present in the system. Blue (open) and red (filled) half circles denote the minority, ↑ fermions and the majority, ↓ fermions, respectively. Observe that the minority fermions appear paired in composites only.

Above and in the following, $\hat{s}_i^\dagger, \hat{s}_i$, $\hat{p}_i^\dagger, \hat{p}_i$ are creation and annihilation operators of ↓ fermions in the s and p bands respectively, while $\hat{s}_{\uparrow i}^\dagger, \hat{s}_{\uparrow i}$ are s-band creation and annihilation operators for ↑ fermions. Accordingly, $\hat{n}_i, \hat{n}_i^p$, and $\hat{n}_i^\uparrow$ are the corresponding number operators. Note that while we take into account s and p bands for ↓ fermions we consider only the s band for the↑ component. That is so because we assume that ↑ fermions form a minority component with filling close to 1/2. On the other hand, we assume a bigger density for ↓ fermions.

The single-particle tunneling part of the Hamiltonian is given by $\hat{H}_{\rm tun}$ (compare Fig. 1). We assume both species to have the same mass and feel the same optical lattice for simplicity. With the adopted sign convention $J_0, J_1 > 0$. The density-dependent tunneling part is denoted as $\hat{H}_{\rm dit}$. The tunneling coefficients T_0, T_1, T_{01} are given by appropriate integrals of Wannier functions [20,23]. Since the p-Wannier orbital is antisymmetric, the interorbital tunneling amplitudes have opposite signs in opposite directions as reflected by $(j\text{-}i)$ factor.

The basic assumption of the model is that attraction between different species dominates the problem energetically. Consider the on-site energy term $\hat{H}_{\rm ons}$. Under our assumption, U_0 is negative with $|U_0|$ giving the large energy scale. E_1, the energy of the p band, is another large energy. As tested by us with Wannier functions for different lattice depths, $|U_1|$, the energy of the interaction between a fermion in the p and in the s band, is smaller than $|U_0|$.

With that assumption, the lowest-energy manifold is filled with composites—pairs of ↑ and ↓ fermions—and the remaining ↓ fermions, leading to nontrivial dynamics. Note that, for example, if a minority ↑ fermion tunnels from a given site, it leads to breaking of the composite. It costs a huge amount of energy ($|U_0|$) unless the tunneling occurs to a site in which a majority ↓ fermion waits to form a composite with the ↑ particle. Only the latter process remains in the low-energy manifold. In effect, the simple tunneling of the minority fermion may be viewed as a tunneling of the composite, accompanied by a reverse direction tunneling of the majority fermion (compare Fig. 2) within this manifold. The system may be described by operators describing excess majority fermions (residing either in the s or p band) and the composites described

FIG. 2. Visualization of the direction-dependent interband density-dependent tunnelings in the dressed picture. The dressed tunneling amplitudes are direction dependent.

by annihilation (creation) operators $\hat{c}_i(\hat{c}_i^\dagger)$ obeying hard-core boson commutation relations. The corresponding composite number operator is $\hat{n}_i^c = \hat{c}_i^\dagger \hat{c}_i$. The presented intuitive picture is fully recovered on a more formal level by an appropriate construction of the effective Hamiltonian [19]. In effect, the excess majority fermions move in the emergent lattice created by the composites. To avoid excessive repetitions we refer the reader to Ref. [19] for details while Ref. [24] provides yet another example of a two-dimensional construction based on the idea described above.

The second important step is to derive the effective Hamiltonian valid for the high-frequency driving obeying the (almost) resonant condition

$$U_1 + E_1 = N\omega + \Delta \tag{2}$$

with N being an integer and a small detuning $|\Delta| \ll \omega$. Observe that the time-dependent part of the Hamiltonian, $\hat{H}_{\rm sh}(t)$, contains two time-periodic terms. The first one describes a standard horizontal lattice shaking (after an appropriate gauge transformation) as originally proposed in Ref. [29] and reviewed, e.g., in Ref. [30]. Such a horizontal shaking has been realized experimentally by several groups [31–33] and serves as a convenient knob on lattice system properties. The second term is due to the harmonic variation of the lattice depth. This translates into a periodic modulation of the p-band energy offset δE_1 [20]. The phase φ between the two harmonic modulations can be easily controlled in experiments. The procedure of averaging is fairly standard and is described in detail in Ref. [20]. We quote here the final effective Hamiltonian expressed in terms of composite and excess fermion operators:

$$\begin{aligned}\hat{H} = {} & \widetilde{T}_{01}^- \sum_{i=1}^{N} (\hat{p}_i^\dagger \hat{n}_i^c \hat{s}_{i+1} + \text{H.c.}) - \widetilde{T}_{01}^+ \sum_{i=1}^{N} (\hat{p}_i^\dagger \hat{n}_i^c \hat{s}_{i-1} + \text{H.c.}) \\ & + (2\widetilde{T}_0 - \widetilde{J}_0) \sum_{i=1}^{N} (\hat{c}_i^\dagger \hat{s}_{i+1}^\dagger \hat{c}_{i+1} \hat{s}_i + \text{H.c.}) \\ & + (2\widetilde{T}_1 + \widetilde{J}_1) \sum_{i=1}^{N} (\hat{p}_i^\dagger \hat{n}_i^c \hat{n}_{i+1}^c \hat{p}_{i+1} + \text{H.c}) \\ & - \widetilde{J}_0 \sum_{i=1}^{N} \hat{s}_i^\dagger \hat{s}_{i+1} + \Delta \sum_{i=1}^{N} \hat{n}_i^p, \end{aligned} \tag{3}$$

where the tilde sign over tunnelings and density-dependent tunnelings indicates their dressed character (after time averaging). Explicitly, $\widetilde{J}_l = \mathcal{J}_0(\frac{K}{\omega}) J_l$ with $l = 0, 1$ corresponding to s and p band respectively and $\mathcal{J}_0$ being the Bessel function [20,29]. A similar dressing takes place for intraband density-dependent tunnelings T_l. On the other hand, the interband

s-p tunneling amplitude value becomes direction dependent due to the phase difference between shaking amplitudes. We express that asymmetry by denoting the tunnelings between $p_i \leftrightarrow s_{i+1}$ as $\widetilde{T}_{01}^{+}$ and $p_i \leftrightarrow s_{i-1}$ as $\widetilde{T}_{01}^{-}$. These tunneling processes are visualized in Fig. 2 and read explicitly [20] $\tilde{T}_{01}^{\pm} = \mathcal{J}_N(A^{\pm}/\omega)T_{01}$, where $A^{\pm} = \sqrt{(K \pm \delta E_1 \cos\varphi)^2 + K^2 \sin^2\varphi}$.

While the frequency of the periodic drive is fixed by the resonance condition (2), the shaking amplitude K provides a convenient parameter to tune the properties of the system. In particular, K_c such that $K_c/\omega \approx 2.405$ corresponds to the zero of $\mathcal{J}_0$ Bessel function. For such a choice of K, the intraband tunnelings almost vanish and the interband density-dependent tunneling becomes the only mechanism of transferring the majority fermions (the composites becoming immobile in this limit). Then, as suggested in Ref. [20] for $n^{\uparrow} = 1/2$ (the filling for minority fermions), the composites form a density wave (DW) in the ground state while the excess majority fermions are described by a Rice-Mele topological dimer model. On the other hand, sufficiently far from K_c the standard tunneling mechanisms dominate—the system then organizes into a clustered phase (CL) with composites and empty sites separated in space [20].

To test this prediction, one has to carefully estimate various parameters appearing in the minimal Hamiltonian, (3). They depend on the details of the lattice potential and interactions between two species. We follow the assumptions of Ref. [20] and assume the optical lattice potential to take the form $V_{\text{latt}} = V_{\parallel}\sin^2(\pi x/a) + V_{\perp}[\sin^2(\pi y/a) + \sin^2(\pi z/a)]$, with a being the lattice constant. For $V_{\perp} \gg V_{\parallel}$ the system is effectively one dimensional. We take $V_{\perp} = 25$ while $V_{\parallel} = 8$ in the units of the recoil energy $E_R = h^2/(8Ma^2)$ (note that $a = \lambda/2$ with λ being the wavelength of the laser beams forming a standing wave pattern). As a dimensionless interaction strength we take a plausible value $\alpha = a_s/a = -0.1$ [with a_s being the (negative) scattering length]. That, together with lattice parameters, allows us to estimate all the tunneling and interaction parameters of the model using the Wannier functions appropriate for the lattice potential [20].

As far as the shaking is concerned, we obviously concentrate on the vicinity of $K/\omega = 2.4$ region, taking the vertical shaking to be in phase with the lateral one ($\varphi = 0$), which gives $\tilde{T}_{01}^{-} > T_{01}^{+}$. For simplicity, we assume first the exact driving resonance $\Delta = 0$. In Fig. 3 we show the dependencies of the different dressed tunnelings as a function of K/ω (we shall later assume a notation $\tilde{K} = K/\omega$) coming from Wannier function calculations.

To find the ground state of (3) we have yet to define the density of majority component, which is taken to be unity (thus we have a 1/2 filling of composites and 1/2 filling of excess fermions). Then, we use the exact diagonalization method based on Refs. [34,35]. Diagonalizations take place in the Fock space of all possible configurations of the system, assuming that each site i may be empty or occupied by a single composite or a $\downarrow$ fermion in s state, or both the composite and $\downarrow$ fermion, although the second one in p state (because there is already an s-state $\downarrow$ fermion in a composite). Therefore, the local Hilbert space consists of four states per site with no truncation. For an even number of fermions, a fermion tunneling between arbitrary edges (that is, between the first and the last site) leads to an additional phase (sign) change arising from the anticommutation relations. Because the number of fermions is half the number of sites, available numbers of sites are of the form of $L = 4l + 2, l \in \mathbb{Z}$.

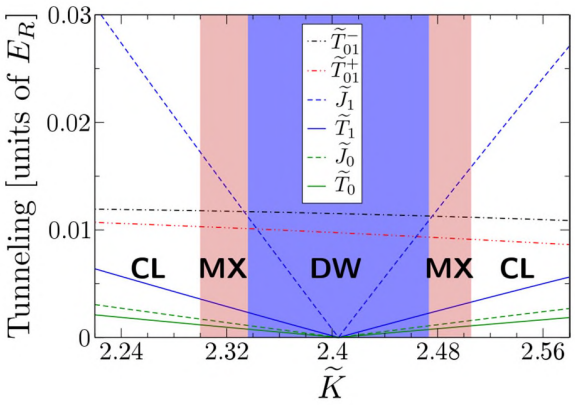

FIG. 3. $\widetilde{J}_i$, $\widetilde{T}_i$ and $\widetilde{T}_{01}^{\pm}$ tunnelings for $V_0 = 8$, $V_{\perp} = 25$, $\alpha = -0.1$, $N = 1$, and $\phi = 0$. For $\tilde{K} = K/\omega$ range shown in the figure there exist three phases: the density wave (DW) (blue), the clustered phase, CL (white), and the mixed phase, MX (pink). Boundaries of these phases were calculated using the fidelity susceptibility (see Fig. 4) and the structure factor (Fig. 5).

With periodic boundary conditions, the Hamiltonian in Eq. (3) commutes with the translation operator ($\hat{T}$), which allows us to use states with the conserved total momentum (k) as our basis: $T\,|a(k)\rangle = e^{ik}\,|a(k)\rangle$. States with different ks are orthogonal to each other, and $k \in \{(-L/2+1)\frac{2\pi}{L}, \ldots, (L/2)\frac{2\pi}{L}\}$ [because $T^L\,|a(k)\rangle = e^{ikL}\,|a(k)\rangle = |a(k)\rangle$] with L being the length of the chain. Diagonalization consists of creating states in the basis (for some or all values of k), calculating matrix elements of $\hat{H}$ in that basis, and using numerical algorithm to get eigenvalues and eigenvectors for the lowest-energy states. We would like to point out that the total momentum k serves only to split the large Hamiltonian matrix into smaller blocks.

III. RESULTS

We carry out exact diagonalizations typically on a chain of length $L = 14$ (leading to matrices of the rank ~840 000). For selected data we show the results for $L = 18$ (matrices of rank around 131×10^6). As tunnelings are nearly symmetric with respect to $\tilde{K}_c \approx 2.405$ (only $T_{01}^{\pm}$ are noticeably different, which leads to small, quantitative—but no qualitative—changes), we will only consider $\tilde{K} < 2.405$. In the interval of interest, the ground state corresponds to $k = \pi$. To characterize its properties and locate possible phase transitions we use the fidelity approach [36]. We calculate the fidelity, F, associated with a small parameter change δ [here $F(\tilde{K},\delta) = \langle\psi_0(\tilde{K} - \delta/2)|\psi_0(\tilde{K} + \delta/2)\rangle$] using the eigenvectors coming from the diagonalization. For $\delta \approx 0$, we get $F \approx 1 - \chi\frac{\delta^2}{2}$, which defines the fidelity susceptibility, χ [37,38]. It is commonly understood that the fidelity susceptibility diverges at phase transitions. For our finite system, the possible crossovers will be identified by the maxima of χ.

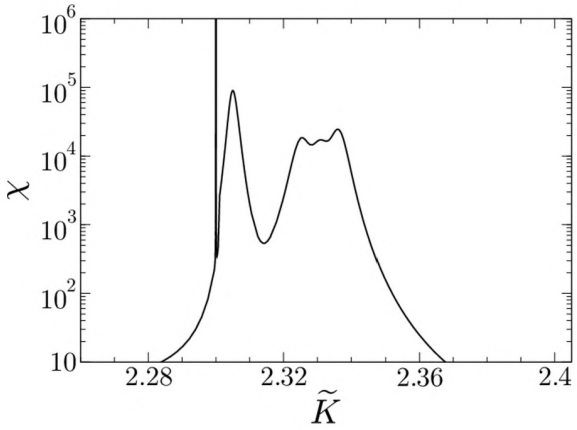

FIG. 4. Fidelity susceptibility, χ, for the ground state for $L = 14$. Observe a sharp peak at $\tilde{K} = 2.3$ and a rich structure of peaks up to about $\tilde{K} = 2.35$. The different phases are analyzed using the structure factor, see the text and Fig. 5.

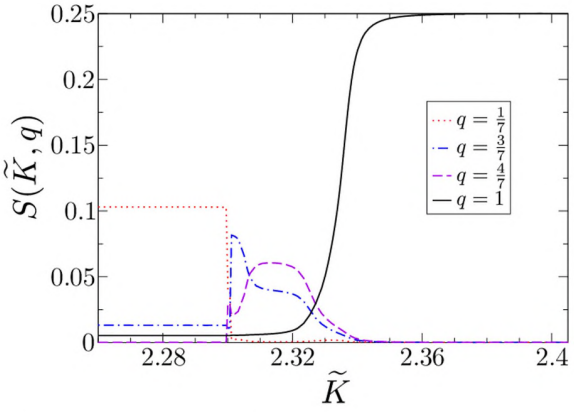

FIG. 5. Structure factor $S(\tilde{K},q)$ calculated for $L = 14$ sites and different q values as indicated in the figure. For $\tilde{K} > 2.35$ a single $q = 1$ value dominates indicating DW phase. Similarly, for $\tilde{K} < 2.29$ $q = 1/7$ dominates pointing out to the clustered phase (CL). Changes in the structure factor behavior nicely correlate with peaks in the fidelity susceptibility, compare Fig. 4).

A. Resonant case

As mentioned above, the simplified analysis [20] predicts the existence of two composite arrangements: the density wave (DW) close to $\tilde{K}_c = 2.405$, where intra-band tunnelings are effectively switched off, and the clustered phase (CL), where the composites group together. Thus, we should expect a single χ maximum for $\tilde{K} < \tilde{K}_c$ corresponding to the border between these two phases. The numerical results are, however, quite different (compare Fig. 4). There are indeed two regions of low-fidelity susceptibility for $\tilde{K} < 2.29$ (with a sharp peak of χ around $\tilde{K} = 2.3$) as well as for $\tilde{K}$ values close to $\tilde{K}_c$ (for $\tilde{K} \gtrsim 2.35$) indicating stable phases. On the other hand, the interval $\tilde{K} \in (2.29, 2.35)$ shows a structure of peaks with χ having significant values almost everywhere.

To understand that somewhat complicated behavior of χ we consider the structure factor here defined as

$$S(\tilde{K},q) = \frac{1}{L}\left\langle \sum_{|i-j|} \left(\hat{n}_i^c - \frac{1}{2}\right)\left(\hat{n}_j^c - \frac{1}{2}\right) e^{-iq\pi|i-j|} \right\rangle, \quad (4)$$

where $\hat{n}_i^c$ is the number of composite bosons (0 or 1 in our case) occupying ith site. Figure 5 shows three areas with different behavior of structure factor, each corresponding to different phase structure. For the CL phase, the structure factor $S(\tilde{K}, q = 2/L) \approx 0.1$, while values for different q are close to 0, which happens to be the case for $\tilde{K}$ sufficiently far from $\tilde{K}_c$. On the other hand, for DW, $S(\tilde{K}, q = 1) = 0.25$ and vanishes for other q values. Such a behavior is seen close to the resonance, $\tilde{K} > 2.35$. Thus, indeed the two phases obtained close to the resonance and far from it show the properties predicted in Ref. [20]. Note that since the number of particles is strictly conserved in exact diagonalization, we cannot use some mean-field order parameter to classify the phases observed. Still the identification based on the structure factor is unambiguous.

The behavior is more complicated in the intermediate interval of $\tilde{K}$ values. The structure factor for both $q = 2/L$ and $q = 1$ becomes small while intermediate q values $(4/L, 6/L, \ldots)$ become important. The situation seems somehow clearer close to the border of phase transitions. Around $\tilde{K} = 2.3$ the peak in fidelity susceptibility coincides with the change in ground-state structure [as seen in the $S(\tilde{K},q)$ plot]; instead of the fully separated phases of composites and empty sites we observe splitting of the composites cluster into two [in small $(\Delta\tilde{K} \approx 0.001)$ interval directly above $\tilde{K} = 2.3$] and three clusters (which corresponds to the dominant $S(\tilde{K}, 3/7)$ value). Let us denote the pure CL phase as a string 0000000CCCCCCC with C sites being filled by composites. Respective many-cluster phases can be traced back to 00000CC00CCCCC and 000CC00CC00CCC configurations as verified by a careful examination of the ground-state wave-function expansion in Fock space (possible due to the small size of our system). On the other hand, while in the vicinity of $\tilde{K}_c$ we observe a pure DW phase, close to $\tilde{K} = 2.35$ the inspection of the wave function reveals an addition of defected components, with two sites breaking the DW symmetry. The relative importance of a single defect component changes smoothly from practically zero close to $\tilde{K}_c$ [observe that above $K = 2.35$ all q components of $S(\tilde{K},q)$ vanish except $q = 1$] to become significant below $\tilde{K} = 2.35$. The subsequent peaks of the fidelity susceptibility, χ in Fig. 4 nicely coincide with different components of $S(\tilde{K},q)$ dominating the structure factor. That corresponds, as again confirmed by the inspection of the wave-function components, to successive defects of the partial DW leading to small clusters eventually merging as $\tilde{K}$ moves further away from $\tilde{K}_c$.

One may pose an important question whether the mixed phase observed is not really a finite-size effect, which will disappear in the thermodynamic limit and the mean-field analysis [20] will be recovered in that limit. To provide an answer, we have evaluated the borders between different phases for the longer chain with $L = 18$. Plotting the borders as a function of $1/L$ and extrapolating to the infinite chain one can see a clear indication that the mixed phase should not be purely a finite size effect (see Fig. 6). Let us note that this behavior is reminiscent of striped phases observed in the two-dimensional Falicov-Kimball model [39]. Importantly,

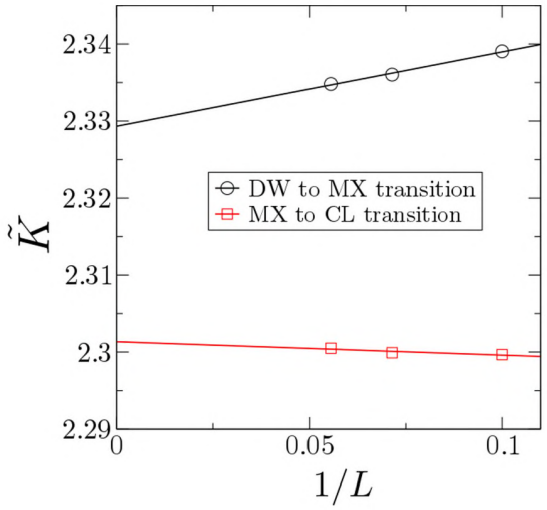

FIG. 6. Borders between DW and MX phase as well as MX and CL phase as a function of the inverse system size. Observe that the mixed phase persists in the extrapolated $L \to \infty$ limit.

considering the standard optical lattices systems, the typical lattice size is about 50 sites, thus the results obtained here are of a direct experimental relevance.

Using results from diagonalizations, one can easily calculate the correlation function of composite bosons, $\langle c_0^\dagger c_j \rangle$. When a system is in the DW phase, the correlation function decays exponentially with increasing $j|\langle c_0^\dagger c_j \rangle| \propto \exp(-j/l_c)$, compare Fig. 7. The correlation length l_c depends strongly on $\tilde{K}$, compare the correlation functions for $\tilde{K} = 2.36$ and $\tilde{K} = 2.40$. For other phases much slower decay, presumably powerlike, is observed but no definite conclusions may be drawn due to small sizes considered. To that end, one should perform a numerical study of a much larger chain, e.g., using density matrix renormalization group (DMRG), which is beyond the scope of the present work.

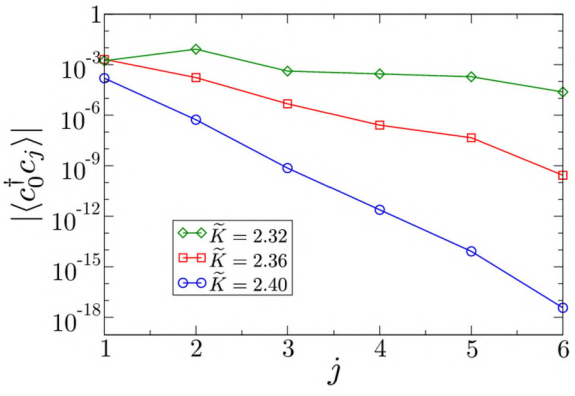

FIG. 7. Correlation function $\langle c_0^\dagger c_j \rangle$ of creation operators for boson composites in ground state calculated for $L = 14$ sites system for three values of parameter $\tilde{K} = K/\omega$, which are in the mixed ($\tilde{K} = 2.32$) and density wave ($\tilde{K} = 2.36, 2.40$) phases. The correlation function decays exponentially in the DW phase, for the MX and CL (not shown) phase the decay is much slower, presumably powerlike.

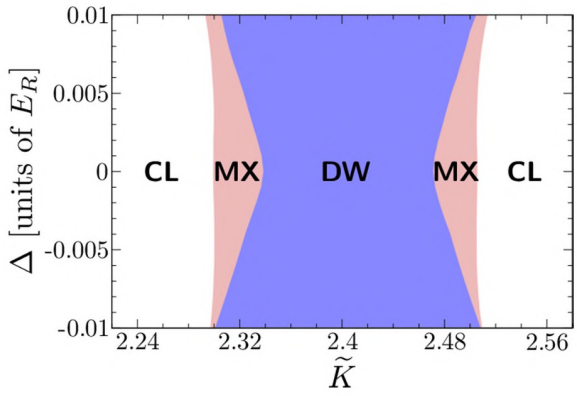

FIG. 8. Different phases in the $\tilde{K}$-Δ plane. Observe the shrinking of the intermediate mixed phases region while the interesting density wave arrangement of composites region gets larger. The borders obtained for this plot were collected from diagonalizations of $L = 10$ system with five composites, results for $L = 14$ at selected points show that the picture is not affected significantly by the system size.

B. Detuned case

While the studies of Ref. [20] and the results presented above concentrated on the $\Delta = 0$ case corresponding in the DW phase to the SSH Hamiltonian [12], it is interesting to see whether the full Rice-Mele model [13] for $\Delta \neq 0$ leads to similar conclusions. To that end, we have studied the phase diagram in the $\tilde{K}$-Δ plane as shown in Fig. 8. Observe that while the border of the CL phase is not sensitive to Δ, the region of DW actually increases eating up the MX phase. Therefore, the Rice-Mele model seems to be realized quite easily with the present system.

The most interesting physics of the Rice-Mele model comes from localized modes on defects on the borders between topological and trivial phases [13,40]. As discussed in Ref. [20], the present model allows for control of the number of defects by changing slightly the filling of minority fermions, i.e., of composites. For the filling $n_c < 1/2$ one creates holes in the DW, for $n_c > 1/2$ we should have extra

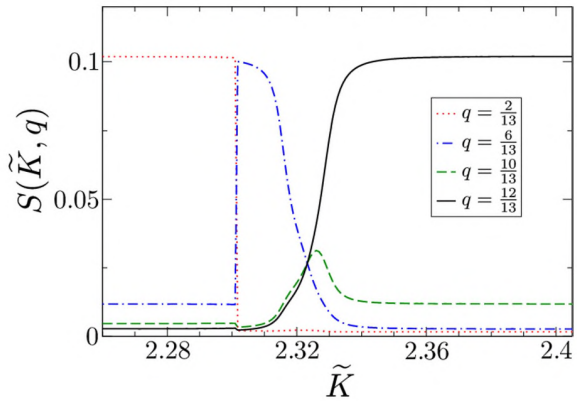

FIG. 9. Structure factor $S(\tilde{K}, q)$ for $L = 13$ and $N = 6$ composites. Such a situation results in a defect (hole) present in the system. A single hole leads to a structure factor being dominant for $q = 12/13$, the presence of a hole results in nonvanishing values of S for other q's. As before, the CL phase is characterized by the structure factor being most prominent at $q = 2/L$.

particles. Indeed, as visualized in Fig. 9 when we consider six composites in $L = 13$ sites, the DW phase (occurring for seven composites and $L = 14$ sites) is replaced by a single-hole phase (SHP). Due to the periodic boundary conditions and the translational invariance of the system, the ground state is a combination of states with a hole at different positions along the lattice as revealed by the eigenstate inspection in the Fock representation. The border between a SHP and mixed configurations is placed close to the value for the border of the DW phase in an ideal half filling of composites (taking into account finite-size effects). For $\tilde{K}$ far from $\tilde{K}_c$, we observe a sharp phase transition to clustered phase with holes and defects separated.

IV. CONCLUSIONS

Using exact diagonalization on small systems, we have addressed the problem of resonantly shaken optical lattices in which an unevenly populated mixture of two species of fermions is held. We have verified the basic model studied in Ref. [20] where, neglecting minority fermion tunnelings, density wave arrangements of composites were found in the situation when the shaking amplitude was tuned in a way enabling switching off all of the intraband tunnelings. Then, the excess majority fermions move in an emergent lattice (formed by composites) with direction-dependent tunnelings realizing the topological Rice-Mele model. In the simplified approach [20], it was found that apart from the density wave (for switched off intraband tunnelings) the composites and empty sites may separate forming two clusters—when the intraband tunnelings are important. That has also been confirmed by the present calculation. In addition to these two phases, the middle region separating these ideal cases is revealed by an exact diagonalization. In this mixed-phase region, the ground state contains superposition of many different composite arrangements. This phase may show quasi-long-range order, which is absent in the density wave phase.

We have also shown that the density wave phase in the vicinity of shaking parameters combination switching off intraband tunnelings ($K/\omega \approx 2.405$, the zero of zero-order Bessel function) persists even when the shaking frequency is not adapted precisely to the s-p orbital resonance condition, thus it is quite robust. We have explicitly shown that the deviations from the ideal half filling of the minority fermions (and thus the composites) leads directly to defects (holes or extra particle) that, if occurring on the edge of the topologically nontrivial phase, lead to localized modes.

ACKNOWLEDGMENTS

This work was realized under National Science Centre (Poland) Project No. DEC-2012/04/A/ST2/00088. The support of EU Grant QUIC (H2020-FETPROACT-2014 No. 641122) is also acknowledged.

[1] M. Z. Hasan and C. L. Kane, Rev. Mod. Phys. **82**, 3045 (2010).
[2] X.-L. Qi and S.-C. Zhang, Rev. Mod. Phys. **83**, 1057 (2011).
[3] C. Nayak, S. H. Simon, A. Stern, M. Freedman, and S. Das Sarma, Rev. Mod. Phys. **80**, 1083 (2008).
[4] J. E. Moore, Nature (London) **464**, 194 (2010).
[5] D. Pesin and A. H. MacDonald, Nat. Mater. **11**, 409 (2012).
[6] L. Tarruell, D. Greif, T. Uehlinger, G. Jotzu, and T. Esslinger, Nature (London) **483**, 302 (2012).
[7] P. Hauke, O. Tieleman, A. Celi, C. Ölschläger, J. Simonet, J. Struck, M. Weinberg, P. Windpassinger, K. Sengstock, M. Lewenstein, and A. Eckardt, Phys. Rev. Lett. **109**, 145301 (2012).
[8] C.-Z. Chang, J. Zhang, X. Feng, J. Shen, Z. Zhang, M. Guo, K. Li, Y. Ou, P. Wei, L.-L. Wang, Z.-Q. Ji, Y. Feng, S. Ji, X. Chen, J. Jia, X. Dai, Z. Fang, S.-C. Zhang, K. He, Y. Wang, L. Lu, X.-C. Ma, and Q.-K. Xue, Science **340**, 167 (2013).
[9] M. Aidelsburger, M. Atala, M. Lohse, J. T. Barreiro, B. Paredes, and I. Bloch, Phys. Rev. Lett. **111**, 185301 (2013).
[10] G. Jotzu, M. Messer, R. Desbuquois, M. Lebrat, T. Uehlinger, D. Greif, and T. Esslinger, Nature (London) **515**, 237 (2014).
[11] M. Aidelsburger, M. Lohse, C. Schweizer, M. Atala, J. T. Barreiro, S. Nascimbène, N. R. Cooper, I. Bloch, and N. Goldman, Nat. Phys. **11**, 162 (2015).
[12] W. P. Su, J. R. Schrieffer, and A. J. Heeger, Phys. Rev. Lett. **42**, 1698 (1979).
[13] M. J. Rice and E. J. Mele, Phys. Rev. Lett. **49**, 1455 (1982).
[14] M. Atala, M. Aidelsburger, J. T. Barreiro, D. Abanin, T. Kitagawa, E. Demler, and I. Bloch, Nat. Phys. **9**, 795 (2013).
[15] M. Lohse, C. Schweizer, O. Zilberberg, M. Aidelsburger, and I. Bloch, Nat. Phys. (2015), doi:10.1038/nphys3584.
[16] S. Nakajima, T. Tomita, S. Taie, T. Ichinose, H. Ozawa, L. Wang, M. Troyer, and Y. Takahashi, Nat. Phys. (2016), doi:10.1038/nphys3622.
[17] E. Schonbrun and R. Piestun, Opt. Eng. **45**, 028001 (2006).
[18] Y. V. Kartashov and L. Torner, Phys. Rev. A **74**, 043617 (2006).
[19] O. Dutta, A. Przysiężna, and M. Lewenstein, Phys. Rev. A **89**, 043602 (2014).
[20] A. Przysiężna, O. Dutta, and J. Zakrzewski, New J. Phys. **17**, 013018 (2015).
[21] A. Mering and M. Fleischhauer, Phys. Rev. A **83**, 063630 (2011).
[22] D.-S. Lühmann, O. Jürgensen, and K. Sengstock, New J. Phys. **14**, 033021 (2012).
[23] O. Dutta, M. Gajda, P. Hauke, M. Lewenstein, D.-S. Lühmann, B. A. Malomed, T. Sowiński, and J. Zakrzewski, Rep. Prog. Phys. **78**, 066001 (2015).
[24] O. Dutta, A. Przysiężna, and J. Zakrzewski, Sci. Rep. **5**, 11060 (2015).
[25] Z. Cai, Y. Wang, and C. Wu, Phys. Rev. A **83**, 063621 (2011).
[26] E. Zhao and W. V. Liu, Phys. Rev. Lett. **100**, 160403 (2008).
[27] Z. Zhang, X. Li, and W. V. Liu, Phys. Rev. A **85**, 053606 (2012).
[28] X. Li and W. V. Liu, arXiv:1508.06285.
[29] A. Eckardt, C. Weiss, and M. Holthaus, Phys. Rev. Lett. **95**, 260404 (2005).
[30] E. Arimondo, D. Ciampini, A. Eckardt, N. Holthaus, and O. Morsch, Adv. At. Mol. Opt. Phys. **61**, 515 (2012).

[31] H. Lignier, C. Sias, D. Ciampini, Y. Singh, A. Zenesini, O. Morsch, and E. Arimondo, Phys. Rev. Lett. **99**, 220403 (2007).
[32] A. Zenesini, H. Lignier, D. Ciampini, O. Morsch, and E. Arimondo, Phys. Rev. Lett. **102**, 100403 (2009).
[33] J. Struck, C. Ölschläger, R. Le Targat, P. Soltan-Panahi, A. Eckardt, M. Lewenstein, P. Windpassinger, and K. Sengstock, Science **333**, 996 (2011).
[34] A. W. Sandvik, AIP Conf. Proc. **1297**, 135 (2010).
[35] J. M. Zhang and R. X. Dong, Eur. J. Phys. **31**, 591 (2010).
[36] P. Zanardi and N. Paunković, Phys. Rev. E **74**, 031123 (2006).
[37] W.-L. You, Y.-W. Li, and S.-J. Gu, Phys. Rev. E **76**, 022101 (2007).
[38] B. Damski, Phys. Rev. E **87**, 052131 (2013).
[39] R. Lemański, J. K. Freericks, and G. Banach, Phys. Rev. Lett. **89**, 196403 (2002).
[40] A. J. Heeger, S. Kivelson, J. R. Schrieffer, and W. P. Su, Rev. Mod. Phys. **60**, 781 (1988).

PHYSICAL REVIEW B **95**, 085102 (2017)

Fibonacci anyon excitations of one-dimensional dipolar lattice bosons

Tanja Đurić,[1] Krzysztof Biedroń,[1] and Jakub Zakrzewski[1,2]
[1]*Instytut Fizyki im. M. Smoluchowskiego, Uniwersytet Jagielloński, Łojasiewicza 11, 30-348 Kraków, Poland*
[2]*Mark Kac Complex Systems Research Center, Jagiellonian University, Łojasiewicza 11, 30-348 Kraków, Poland*
(Received 22 April 2016; revised manuscript received 15 December 2016; published 1 February 2017)

We study a system of dipolar bosons in a one-dimensional optical lattice using exact diagonalization and density matrix renormalization group methods. In particular, we analyze low energy properties of the system at an average filling of 3/2 atoms per lattice site. We identify the region of the parameter space where the system has non-Abelian Fibonacci anyon excitations that correspond to fractional domain walls between different charge-density waves. When such one-dimensional systems are combined into a two-dimensional network, braiding of Fibonacci anyon excitations has potential application for fault tolerant, universal, topological quantum computation. Contrary to previous calculations, our results also demonstrate that super-solid phases are not present in the phase diagram for the discussed 3/2 average filling. Instead, decreasing the value of the nearest-neighbor tunneling strength leads to a direct, Berezinskii-Kosterlitz-Thouless, superfluid to charge-density-wave quantum phase transition.

DOI: 10.1103/PhysRevB.95.085102

I. INTRODUCTION

The large recent interest in non-Abelian topological phases of matter is strongly motivated by the possibility of a fault-tolerant topological quantum computation [1–6] based upon non-Abelian anyons [7–10] that appear as quasiparticle excitations for such exotic quantum phases of matter. The errors caused by local interactions with the environment are a basic obstacle for quantum computation. The main idea behind topological quantum computation is that non-Abelian anyonic quasiparticles can be used to encode and manipulate information in a way that is resistant to errors, and therefore to perform fault-tolerant quantum computation without loss of information (decoherence).

The understanding of the origin and properties of non-Abelian states of matter is also of fundamental importance and is at the frontier of current theoretical and experimental research [11–15]. The main objective is the investigation of new models that have non-Abelian quasiparticle excitations, or support non-Abelian defects, as a result of complex interplay between topology and quantum mechanics [16,17]. The robustness against small local perturbations is due to the topological nature of these states of matter, that therefore can be used as building blocks for topological quantum computation.

In this paper we study a system of ultracold dipolar bosons trapped in a one-dimensional (1D) optical lattice and at an average filling of 3/2 atoms per lattice site. The system can be well described by an extended Bose-Hubbard Hamiltonian with the on-site and nearest-neighbor interactions [18]. We study the ground states and low energy elementary excitations of the system in the regime of small tunneling between lattice sites and identify the region of the parameter space where the system supports non-Abelian, $SU(2)_3$ Fibonacci anyon excitations.

In 1D quantum statistics is not well defined. The interchange of two quasiparticles in one spatial dimension is impossible without one particle going through another. Therefore the adiabatic exchange (braiding) of these quasiparticles is not possible in the strictly 1D system that we have considered. However, braiding can be achieved by connecting these 1D systems with T junctions into a two-dimensional (2D) network as suggested previously in the case of Majorana quantum wires [19].

Our results show that the system supports Fibonacci anyon excitations in the regime where (quasi)degenerate manifolds of energy states are well defined, without crossings between the energy levels within different manifolds. This regime corresponds only to a part of the charge-density-wave (CDW) region in the phase diagram of the system, while the system has nontrivially (quasi)degenerate ground states in the whole CDW region. As indicated in previous studies [18,20], Fibonacci anyon excitations correspond to fractional domain walls between different CDWs.

Also, contrary to previous calculations based on Gutzwiller wave-function approach [18], our results demonstrate that the supersolid (SS) phases are not present between the superfluid (SF) and CDW regions of the phase diagram of the system for the specific average filling of 3/2 atoms per lattice site considered throughout this paper. The system for arbitrary fillings has also been considered by Batrouni *et al.* [21] where the SS phases were observed at other higher fillings. Still at the particular value of $\nu = 3/2$ the authors of [21] were unable to verify the presence of the SS phases. We claim that instead, decreasing the tunneling strength between the neighboring sites leads to a direct, Berezinskii-Kosterlitz-Thouless (BKT), superfluid (SF) to charge-density-wave (CDW) quantum phase transition.

The anyonic quasiparticles, which are neither fermions nor bosons, are associated to systems in two spacial dimensions. Namely, when two quasiparticles are exchanged in two dimensions, the wave function of the system can gain any phase factor $e^{i\alpha}$, which motivated the name anyons. On the other hand in three spacial dimensions the only possible phase factors are $e^{i\alpha} = +1$ or -1, which corresponds to bosons or fermions.

If in addition there are m degenerate states ψ_i $(i = 1,...,m)$ for n quasiparticles at positions $x_1,...,x_n$, the result of the quasiparticle exchanges is more than just a change of the phase of the wave function. In that case an exchange of two quasiparticles can rotate one of the degenerate states, ψ_i, into a different degenerate state ψ_j within a m-dimensional

degenerate Hilbert space for n quasiparticles, $\psi_i \to A_{ij}\psi_j$. In general, exchange of other two quasiparticles will be described by a different rotation matrix, $\psi_i \to B_{ij}\psi_j$. For two consecutive exchanges of the quasiparticles, the final state of the system will depend upon the order in which these exchanges were performed, since the matrices A and B do not commute, that is $AB \neq BA$. Such states and their quasiparticle excitations are therefore called non-Abelian or noncommutative.

This exotic non-Abelian statistical behavior allows fault-tolerant manipulation of the quantum information stored in m-dimensional Hilbert space of n non-Abelian quasiparticles. Quantum computation is a process of initializing a controllable quantum system to some known initial state $|\psi_i\rangle$, evolving the system by a unitary transformation $U(t)$ to some final state $|\psi_f\rangle$, and finally measuring the state $|\psi_f\rangle$ at the end of the computation. The quantum computational code is defined by the unitary transformations, which can be engineered to be any unitary transformations if there is sufficient control over the underlying Hamiltonian of the system.

For a large class of non-Abelian states any unitary transformation can be generated only by braiding quasiparticles [2,3], which consequently allows universal topological quantum computation through braiding. An example of such non-Abelian states are the states that support $SU(2)_3$ Fibonacci anyon quasiparticle excitations [2–4]. The final result of the computation, that is the final state of the system after evolution by a unitary transformation, can be obtained by a topological measurement based on a non-Abelian generalization of the Aharonov-Bohm effect [2–4].

Non-Abelian states were initially predicted in fractional quantum Hall (FQH) systems [7,22–27] that are constrained to two spacial dimensions, and subsequently in various similar FQH-like systems in 2D [4,26,28–39]. However, analogous states were also found to appear in various one-dimensional (1D) models [40–50].

Whether in 1D or 2D, non-Abelian states of matter have a global hidden order with constituent particles following a global pattern that is not associated with breaking of any symmetry. This hidden order is associated with organization of particles in indistinguishable clusters [27,44,45,49,51]. Each cluster corresponds to an underlying Abelian copy, and $SU(2)_k$ non-Abelian states can be obtained from k such Abelian copies by symmetrizing over the coordinates of the clusters [27,44,45,49,51]. This symmetrization (indistinguishability) can be achieved by applying a projection operator to a direct product of the wave functions for k copies, which introduces the possibility of topological degeneracy and non-Abelian statistics in the space of quasiparticles.

The projection operator projects k local degrees of freedom corresponding to k copies onto a new degree of freedom that is symmetric under exchange of any of the k components and leads to a topological degeneracy not related to simple symmetry considerations. This topological degeneracy is robust against perturbations and interactions with the environment.

In our calculations we use exact diagonalization (ED) and density matrix renormalization group (DMRG) [52–54] methods to study low energy properties of the system for system sizes up to 124 lattice sites and with periodic boundary conditions.

The region of the parameter space where the system supports non-Abelian Fibonacci anyon excitations is determined by calculating the overlaps between the exact wave functions for the low-energy states of the Hamiltonian describing the system at average filling of $\nu = 3/2$ atoms per lattice site and the corresponding ansatz wave functions which have $SU(2)_3$ non-Abelian order by construction.

The ansatz states are constructed by applying a symmetrization projection operator to a direct product of the corresponding wave functions for three Abelian copies at filling fraction $\nu = 1/2$ atoms per lattice site. The projection operator introduces indistinguishability between the copies (symmetrization over the coordinates of the clusters) which leads to $SU(2)_3$ non-Abelian order.

The paper is organized as follows. In Sec. II we consider exactly solvable points in the parameter space of the underlying extended Bose-Hubbard Hamiltonian and demonstrate that Fibonacci anyon excitations correspond to fractional domain walls between different degenerate CDW ground states of the system. In Sec. III we present ED and DMRG results away from the exactly solvable points. In Sec. IV we further characterize the SF to CDW quantum phase transition. Protocol for braiding fractional domain walls within a 2D T-junction network is described in Sec. V. We draw our conclusions in the final section, Sec. VI.

II. FIBONACCI ANYON EXCITATIONS AS FRACTIONAL DOMAIN WALLS

The system of ultracold dipolar bosons in a 1D optical lattice can be well described by an extended Bose-Hubbard Hamiltonian of the form [18]

$$H = -t\sum_i (a_i^\dagger a_{i+1} + a_{i+1}^\dagger a_i) + \frac{U}{2}\sum_i n_i(n_i - 1) + V\sum_i n_i n_{i+1}, \quad (1)$$

where t is the tunneling amplitude between the neighboring sites, U is the on-site interaction, V is the nearest-neighbor interaction, and the bosonic operators $a_i^\dagger/a_i$ create/annihilate a boson on site i. The operator $n_i = a_i^\dagger a_i$ denotes the number of bosons on site i.

Previous studies showed that the Hamiltonian (1) near the lattice filling $\nu = k/2$ supports $SU(2)_k$ anyonic excitations in the parameter regions where the system has nontrivially degenerate CDW ground states [18,20]. In particular, at average filling $\nu = 3/2$ that we consider, the low energy excitations are $SU(2)_3$ Fibonacci anyons. To demonstrate that the low-energy $SU(2)_k$ anyonic excitations correspond to domain walls between different degenerate CDW ground states we first consider exactly solvable points in the parameter space, that is, the ground states and the low energy excitations of the Hamiltonian (1) at $t = 0$ and $U = 2V$.

In general, for the filling fraction $\nu = k/2$ at $t = 0$ and $U = 2V$, the ground state has nontrivial degeneracy. The ground states are all CDW states with unit cells $[l, k-l]$, where $l = 0, 1, \ldots, k$ [18,20]. For $\nu = 3/2$ there are four degenerate CDW

ground states:

$$\begin{aligned} |030303...\rangle &\equiv [03] \\ |121212...\rangle &\equiv [12] \\ |212121...\rangle &\equiv [21] \\ |303030...\rangle &\equiv [30]. \end{aligned} \tag{2}$$

The low energy quasiparticle/quasihole excitations correspond to domain walls between degenerate CDWs with unit cells $[l,k-l]$ and $[l\pm 1,k-l\mp 1]$ [18,20]. More precisely, following domain walls correspond to elementary excitations [20]

$$\begin{aligned} &[k-l,l][k-l-1,l+1] \ \text{ for } \ 0<l<k, \\ &[k-l,l][k-l+1,l-1] \ \text{ for } \ 0<l<k, \\ &[k,0][k-1,1], \\ &[0,k][1,k-1], \end{aligned} \tag{3}$$

where $[a,b][c,d]\equiv|...ababcdcd...\rangle$. For the filling fraction $\nu=3/2$ elementary quasihole and quasiparticle excitations are [20]

$$\begin{aligned} |...21211212...\rangle &\equiv [21][12], \\ |...12122121...\rangle &\equiv [12][21], \\ |...12120303...\rangle &\equiv [12][03], \\ |...21213030...\rangle &\equiv [21][30]. \end{aligned} \tag{4}$$

If the lattice bosons have a charge q, than the quasiparticle/quasihole excitations have a fractional charge $\pm q/2$ [18,20]. In other words, the states (4) have one boson more or less at two sites where a domain wall is formed. Since the states (4) have one particle more or less than the ground states, for a system with a fixed number of particles the elementary excitations are quasiparticle-quasihole pairs.

We further demonstrate that these fractional domain walls are non-Abelian $SU(2)_3$ Fibonacci anyons [10], similar to the elementary excitations of the $\nu=12/5$ Read-Rezayi fractional quantum Hall (FQH) state [24,25]. If a fractional domain wall is a Fibonacci anyon then its quantum dimension is the golden ratio $d_F=(1+\sqrt{5})/2$ [10,55,56]. The Fibonacci sequence is a sequence with the property that each number in the sequence is the sum of the previous two numbers in the sequence. The non-Abelian anyons with quantum dimension equal to golden ratio are named Fibonacci anyons because the ratio of any number in the Fibonacci sequence to the previous number in the sequence is approximately the golden ratio.

The quantum dimension for these fractional domain walls can be found by considering an adjacency matrix for the elementary excitations [55]. We first note that here charge $q/2$ and charge $-q/2$ elementary excitations are topologically equivalent excitations because they differ by a local operator [55]. The adjacency matrix can then be obtained by considering which pairs of ground states create a $\pm q/2$ fractional domain wall and is given by

$$A=\begin{pmatrix} 0 & 1 & 1 & 0 \\ 1 & 0 & 0 & 1 \\ 1 & 0 & 0 & 0 \\ 0 & 1 & 0 & 0 \end{pmatrix}, \tag{5}$$

where the rows/columns 1,2,3, and 4 refer to the [21],[12],[30], and [03] ground states, respectively.

The adjacency matrix (5) encodes fusion rules for the elementary excitations [55,56]

$$i\times j=\sum_k (A_i)_{jk}k, \tag{6}$$

where A_i is the adjacency matrix of the quasiparticle i. These fusion rules determine the number of ways that quasiparticles i and j can fuse into quasiparticle k. For the Fibonacci anyons τ the fusion rule is

$$\tau\times\tau=1+\tau. \tag{7}$$

Due to the Fibonacci anyon algebra (7) the ground-state degeneracy in the presence of n Fibonacci anyon excitations satisfies the Fibonacci recursion relation [56]

$$G(n)=G(n-1)+G(n-2). \tag{8}$$

In the large n limit the ground-state degeneracy grows as [55,56]

$$\log G(n)\sim n\log d_F... \tag{9}$$

with d_F being the Fibonacci anyon quantum dimension that corresponds to the maximum eigenvalue of the adjacency matrix (5) [55].

For a m-fold degenerate ground-state manifold the statistics of anyons can be described by $m\times m$ unitary matrices that act on the ground-state manifold. Since $m\times m$ unitary matrices form a non-Abelian group (matrices A and B generally do not commute, $AB\neq BA$), these anyons are called non-Abelian anyons.

In the parameter region where the system supports non-Abelian elementary excitations the ground-state degeneracy depends on the topology of the manifold on which the system is defined. For the lattice filling $\nu=k/2$ the ground state will be $k+1$-fold degenerate for periodic boundary condition and nondegenerate for open boundary condition. In other words, the system has nontrivial non-Abelian topological order reflected in topological ground-state degeneracy [57,58]. We also note that in general a topologically ordered state has a quasidegenerate ground state manifold for a finite system size that becomes exactly degenerate in the thermodynamic limit. That will be the case away from the exactly solvable points ($U=2V$, $t=0$) as described in the following section.

III. NUMERICAL RESULTS

To study properties of the system away from the exactly solvable points ($U=2V$, $t=0$) we use ED and DMRG [52–54] methods. Validity of our DMRG results is confirmed by comparison with the ED results for smaller system sizes ($L\leqslant 14$ lattice sites).

We primarily study the ground states and low-lying excitations of the system with periodic boundary conditions for $U,V\gg t$ and for a fixed number of atoms, $N=3L/2$. For such states large occupation of a single site is improbable. This allows the local Hilbert space truncation to single site Fock states $|n_i\rangle$ containing at most $n=n_{\max}$ atoms. For the lattice filling $\nu=N/L=3/2$ it is sufficient to take $n_{\max}=3$, that is,

the local Hilbert space of dimension four with $n_i = 0,1,2,3$.

We first demonstrate that there is a parameter region where the system supports non-Abelian excitations. For those parameter values all (quasi)degenerate lowest energy states have a high overlap ($\simeq 1$) with the corresponding manifold of four ansatz states that have SU(2)$_3$ non-Abelian topological order by construction. We also show that elementary excitations above such states exhibit non-Abelian statistics.

The four non-Abelian ansatz states for the lowest energy, (quasi)degenerate manifold at filling fraction $\nu = 3/2$ can be constructed from the two lowest energy, (quasi)degenerate, Abelian states at filling fraction $\nu = 1/2$, $|\phi_\sigma^{(k)}\rangle_{\bar{t}}$ $(k = 1,2)$, by orthonormalization of the following wave-functions subspace [44,45,49,51]:

$$|\psi^{(l,m,n)}\rangle_{(\bar{t},\bar{U})} = \mathcal{P}(|\phi_\uparrow^{(l)}\rangle_{\bar{t}} \otimes |\phi_\downarrow^{(m)}\rangle_{\bar{t}} \otimes |\phi_\circ^{(n)}\rangle_{\bar{t}}), \tag{10}$$

where $l,m,n = 1,2$ and $\sigma = \uparrow, \downarrow, \circ$ denotes three $\nu = 1/2$ copies. The tunneling parameter and the on-site interaction strength are denoted by $\bar{t} = t/V$ and $\bar{U} = U/V$, respectively.

Here the wave functions $|\phi_\sigma^{(k)}\rangle_{\bar{t}}$ $(k = 1,2)$ correspond to the two lowest energy (quasi)degenerate states of the Hamiltonian

$$H_\sigma = -t\sum_i (a_{\sigma,i}^\dagger a_{\sigma,i+1} + a_{\sigma,i+1}^\dagger a_{i,\sigma}) + V\sum_i n_{\sigma,i}n_{\sigma,i+1}, \tag{11}$$

at average filling $\nu = 1/2$ atoms per lattice site and with periodic boundary conditions, $n_{\sigma,i} = a_{\sigma,i}^\dagger a_{\sigma,i}$ and $a_{\sigma,i}^\dagger/a_{\sigma,i}$ are hard-core boson creation/annihilation operators at site i satisfying $(a_{\sigma,i}^\dagger)^2 = 0$ (that is, only allowed occupation numbers are $n_i^\sigma = 0$ or 1 bosons per site).

At $t = 0$ the wave functions $|\phi_\sigma^{(k)}\rangle_{\bar{t}=0}$ $(k = 1,2)$ are two degenerate CDW states with unit cells [0,1] and [1,0] and the low energy excitations of the Hamiltonian (11) are $\pm q/2$ fractional domain walls that are Abelian anyons similar to the quasiparticle and quasihole excitations of the $\nu = 1/2$ Laughlin FQH state [59]. As illustrated in Fig. 1, the states $|\phi_\sigma^{(k)}\rangle_{\bar{t}}$ $(k = 1,2)$ at some finite value of the parameter $\bar{t} = t/V$ are adiabatically connected to the states at $t = 0$, and therefore have Abelian topological order.

The projection operator $\mathcal{P}$ has the form

$$\mathcal{P} = \mathcal{P}_i^{\otimes L}, \tag{12}$$

with L being the number of lattice sites. Here $\mathcal{P}_i$ is the local projection operator at a lattice site i,

$$\mathcal{P}_i = \begin{pmatrix} 1 & 0 & 0 & 0 & 0 & 0 & 0 & 0 \\ 0 & 1 & 1 & 1 & 0 & 0 & 0 & 0 \\ 0 & 0 & 0 & 0 & \sqrt{2} & \sqrt{2} & \sqrt{2} & 0 \\ 0 & 0 & 0 & 0 & 0 & 0 & 0 & \sqrt{6} \end{pmatrix}, \tag{13}$$

$\mathcal{P}_i$ maps eight-dimensional Hilbert space of three species of hard-core bosons, $\uparrow$, $\downarrow$, and $\circ$, to the single-site four-dimensional Hilbert space of four-hardcore bosons that obey generalized exclusion principle—less than four bosons at any site i, as illustrated in Fig. 2.

After orthonormalization of the wave-functions subspace (10) we find four linearly independent ansatz states, denoted here by $|\psi_{\text{Ansatz}}^{(k)}\rangle_{(\bar{t},\bar{U})}$. The number of linearly independent ansatz states corresponds to the number of lowest energy, (quasi)degenerate states of the Hamiltonian (1) that form the ground state manifold of the Hamiltonian (1).

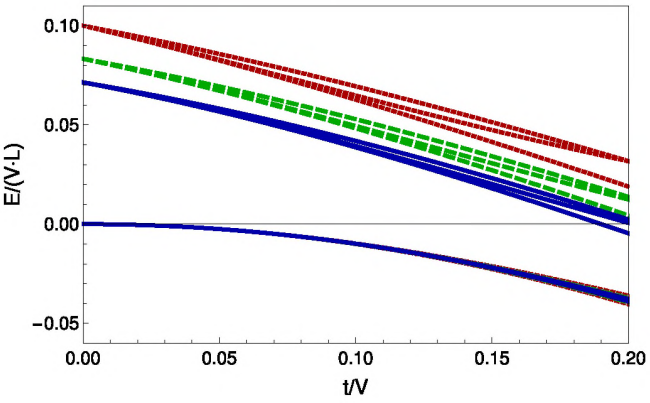

FIG. 1. The ED results for the first five energy levels of the Hamiltonian (11) at filling fraction $\nu = 1/2$ and with periodic boundary conditions, as functions of the tunneling parameter t/V (with V being the nearest-neighbor interaction) and for the system sizes $L = 10$ (red dotted lines), 12 (green dashed lines), and 14 (blue solid lines) lattice sites. Here the energy values (per lattice site) are in units of V.

The states $|\psi_{\text{Ansatz}}^{(k)}\rangle_{(\bar{t},\bar{U})}$, $(k = 1,2,3,4)$ form an orthonormal basis within (quasi)degenerate manifold, which leads to the following expression for the total overlap with the exact lowest energy (quasi)degenerate states of the Hamiltonian (1):

$$O_{i,(\bar{t},\bar{U})} = \sqrt{\sum_{k=1}^{4} \left|{}_{(\bar{t},\bar{U})}\langle\psi_{\text{Exact}}^{(i)}|\psi_{\text{Ansatz}}^{(k)}\rangle_{(\bar{t},\bar{U})}\right|^2}, \tag{14}$$

where $i = 1,...,4$. The ED results for the overlaps (14) for the system sizes $L = 10,12$, and 14 lattice sites are shown in Fig. 3 and Fig. 4. The figures show overlaps for the four lowest (quasi)degenerate states (ground state manifold) of the Hamiltonian (1) for a range of values of the tunneling parameter t/V and for two values of the on-site interaction strength, $U/V = 2$ and $U/V = 1.99$.

For $U = 2V$ and $t = 0$ (exactly solvable points) these states are four degenerate CDWs with unit cells [03], [30], [12], and [21], and the overlaps are exactly 1. This reflects non-Abelian

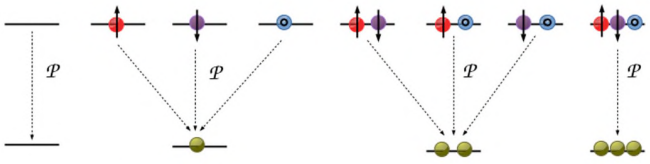

FIG. 2. Schematic of the local projection operator $\mathcal{P}_i$ at a lattice site i. The operator $\mathcal{P}_i$ projects the three local degrees of freedom $\uparrow$, $\downarrow$, and $\circ$, onto a new degree of freedom that is symmetric under exchange of any of the three components. In other words, $\mathcal{P}_i$ maps the single site 8-dimensional Hilbert space of three species of hard-core bosons $\uparrow$ (red spheres), $\downarrow$ (purple spheres), and $\circ$ (blue spheres) to the single-site four-dimensional Hilbert space of four-hard-core bosons (green spheres). These four-hard-core bosons obey generalized exclusion principle—less than four bosons at any lattice site i.

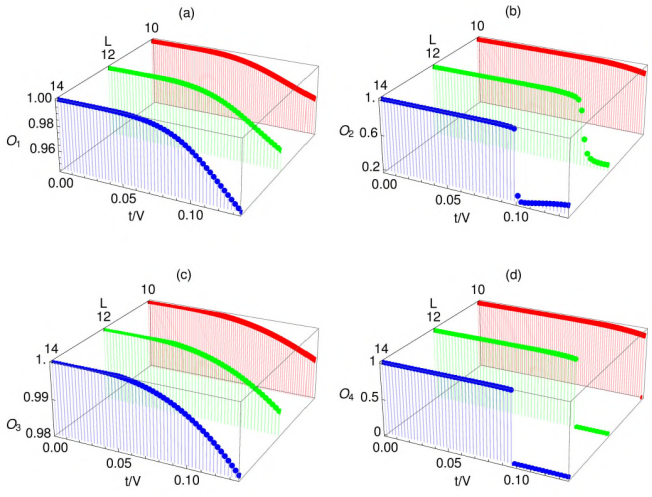

FIG. 3. The ED results for the total overlaps (14) of the four lowest energy, (quasi)degenerate, exact ground states of the Hamiltonian (1) at average filling of $\nu = 3/2$ atoms per lattice site and with periodic boundary conditions [(a)–(d)], with the corresponding orthonormalized ansatz states. Here t/V is the tunneling parameter with V being the nearest-neighbor interaction, and the on-site interaction strength is $U/V = 2$. The system sizes are $L = 10$, 12, and 14 sites (red, green, and blue symbols, respectively).

nature of these states since the ansatz wave functions have non-Abelian topological order by construction, and is in agreement with the results discussed in the previous section. However, the overlaps for all four states are $\simeq 1$ for a range of values of the tunneling parameter t/V, both at $U = 2V$ (Fig. 3) and slightly away from $U = 2V$ (for example for $U = 1.99V$, Fig. 4). This indicates non-Abelian nature of the states away from the exactly solvable points.

Sudden decrease of the overlap, from $\simeq 1$ to zero, for the states (b) and (d) in Fig. 3 and Fig. 4, is related to a crossing between the energy levels within the (quasi)degenerate, ground state manifold, and the energy levels within the (quasi)degenerate first excited manifold. That can be clearly

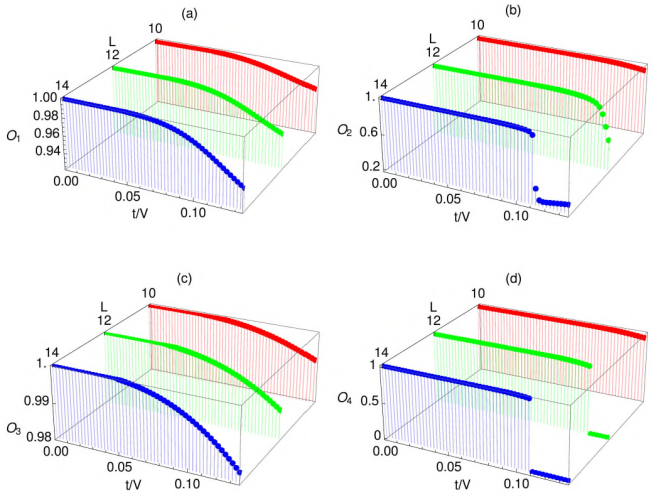

FIG. 4. Same as Fig. 3 for the on-site interaction strength $U/V = 1.99$.

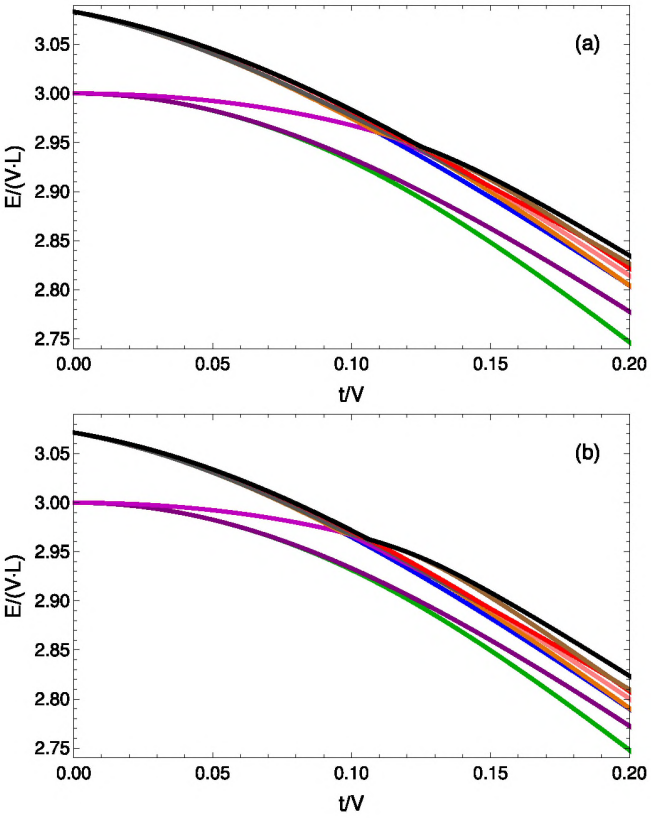

FIG. 5. The ED results for the first ten energy levels of the Hamiltonian (1) at filling fraction $\nu = 3/2$ and with periodic boundary conditions, as functions of the tunneling parameter t/V and for the system sizes (a) $L = 12$ and (b) $L = 14$ lattice sites. Here the on-site interaction strength is $U/V = 2$, with V being the nearest-neighbor interaction.

seen in Fig. 5 and Fig. 6. For the states (a) and (c) in Fig. 3 and Fig. 4 the overlaps start deceasing away from $\simeq 1$ at some value of $t/V = \bar{t}_c(L)$. The value $\bar{t}_c$ is characterized by a crossing between the energy levels within the (quasi)degenerate, first excited states manifold, and the energy levels within the (quasi)degenerate, second excited states manifold. These level crossings for the system sizes $L = 10$ and 12 are shown in Fig. 7.

To confirm the non-Abelian nature of the states for $(t/V) < \bar{t}_c$, we further study elementary excitations above the (quasi)degenerate ground state manifold. By construction, the ansatz states (10) have a hidden global order associated with the organization of the particles in three copies of $\nu = 1/2$ states $(\uparrow, \downarrow, \circ)$. The elementary excitations can be constructed by considering the elementary excitations of the three $\nu = 1/2$ copies and symmetrizing [49,51]. Non-Abelian statistics appears as a consequence of the symmetrization (introduced with projection operator $\mathcal{P}$) which leads to a topological degeneracy in the subspace of elementary excitations and non-Abelian algebra of exchanges of elementary excitations (domain walls) [51].

The ansatz states for the first excited states manifold can be constructed by orthonormalization of the following wave-

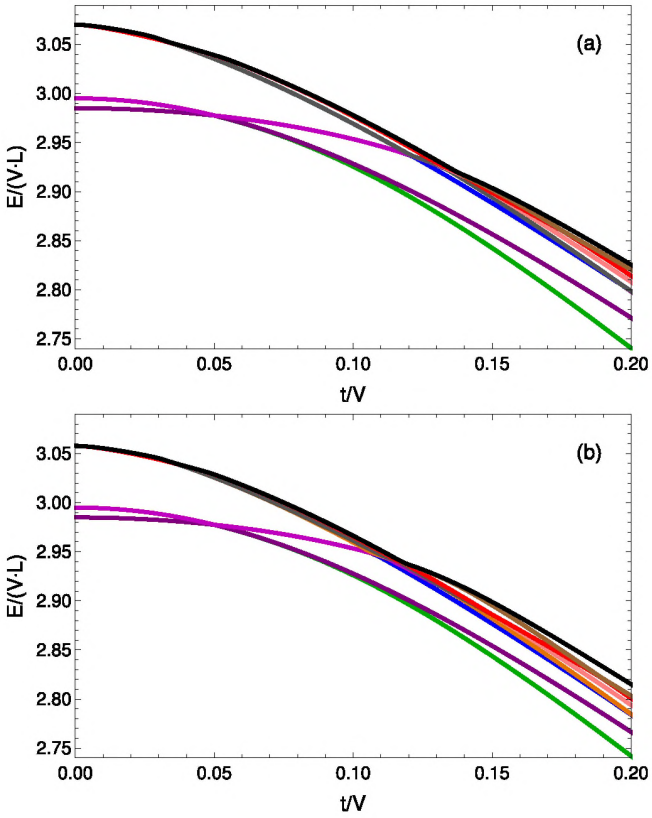

FIG. 6. Same as Fig. 5 for the on-site interaction strength $U/V = 1.99$.

functions subspace [49,51]

$$|\bar{\psi}^{(l,m,n)}\rangle_{(\bar{t},\bar{U})} = \mathcal{P}(|\phi_{\uparrow}^{(l)}\rangle_{\bar{t}} \otimes |\phi_{\downarrow}^{(m)}\rangle_{\bar{t}} \otimes |\bar{\phi}_{\circ}^{(n)}\rangle_{\bar{t}}), \tag{15}$$

where $l,m = 1,2$ and $n = L(L/2-1)$ with L being the number of lattice sites. Here the wave functions $|\phi_{\sigma}^{(k)}\rangle_{\bar{t}}$ $(k = 1,2)$ correspond to the two lowest energy (quasi)degenerate states of the Hamiltonian (11) at average filling $\nu = 1/2$, and the wave functions $|\bar{\phi}_{\sigma}^{(n)}\rangle_{\bar{t}}$ correspond to the states within the (quasi)degenerate, first excited states manifold of the Hamiltonian (11) at $\nu = 1/2$.

The elementary excitations of the Hamiltonian (11) at $\nu = 1/2$ and for a fixed number of particles are $\pm q/2$ domain wall pairs (quasiparticle-quasihole pairs) of the type [01][10]-[10][01]. The number of states in the first excited manifold at $\nu = 1/2$, $\bar{N} = L(L/2-1)$ corresponds to the number of different pairs of sites (i,j) where the domain walls can be created. In addition, there are three possible choices of the two ground states in the ansatz (15): $(l = 1, m = 1)$, $(l = 1, m = 2)$, and $(l = 2, m = 2)$, which gives in total $\bar{N}_L = 3L(L/2-1)$ linearly independent ansatz states for the first excited states manifold at $\nu = 3/2$. These ansatz states, denoted by $|\bar{\psi}_{\text{Ansatz}}^{(k)}\rangle_{(\bar{t},\bar{U})}$ $(k = 1,2,...,\bar{N}_L)$, are obtained after orthonormalization of the wave-function subspace (15).

The total overlap with the exact states within the first excited, (quasi)degenerate manifold of the Hamiltonian (1) is

$$\bar{O}_{\bar{t},(\bar{t},\bar{U})} = \sqrt{\sum_{k=1}^{\bar{N}_L} \left|{}_{(\bar{t},\bar{U})}\langle\bar{\psi}_{\text{Exact}}^{(\bar{t})}|\bar{\psi}_{\text{Ansatz}}^{(k)}\rangle_{(\bar{t},\bar{U})}\right|^2}, \tag{16}$$

where $\bar{t} = 1,...,\bar{N}_L$ denotes the states $|\bar{\psi}_{\text{Exact}}^{(\bar{t})}\rangle_{(\bar{t},\bar{U})}$ within the first excited states manifold.

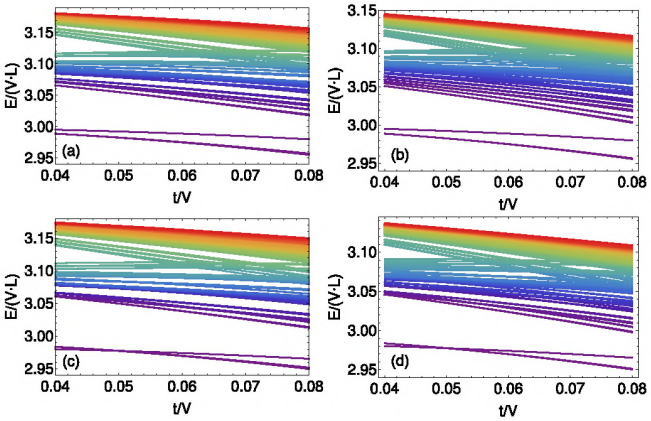

FIG. 7. The energy levels of the Hamiltonian (1) at average filling of $\nu = 3/2$ atoms per lattice site, obtained by ED method for the system sizes $L = 10$ [(a) and (c)] and $L = 12$ [(b) and (d)] lattice sites and with periodic boundary conditions. Here on-site interaction strength $\bar{U} = U/V = 2$ [(a) and (b)] and $\bar{U} = U/V = 1.99$ [(c) and (d)], with V being the nearest-neighbor interaction. As explained in the text the system supports Fibonacci anyon excitations in the regime $(t/V) \lesssim 0.05$ where (quasi)degenerate energy manifolds are well defined and there is no level crossing between the states within different manifolds.

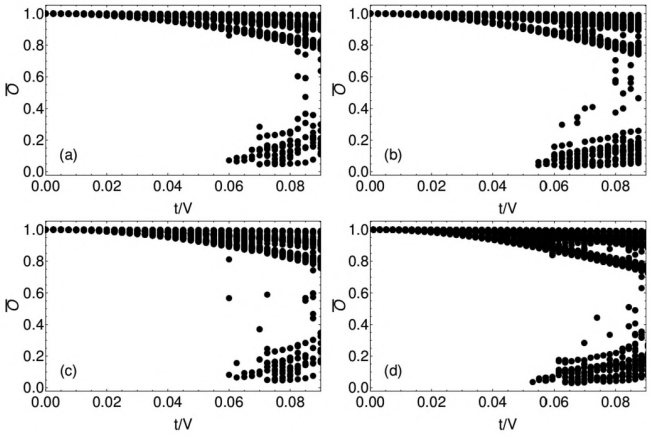

FIG. 8. The ED results for the total overlaps (16) of the $3L(L/2-1)$ exact, (quasi)degenerate states within the first excited states manifold of the Hamiltonian (1) at average filling of $\nu = 3/2$ and with periodic boundary conditions, with the corresponding orthonormalized ansatz states. Here t/V is the tunneling parameter with V being the nearest-neighbor interaction, and the on-site interaction strength is $U/V = 2$ [(a) and (b)] and $U/V = 1.99$ [(c)and (d)]. The system sizes are $L = 10$ [(a) and (c)] and $L = 12$ [(b) and (d)] lattice sites.

The ED results for the overlaps (16) are shown in Fig. 8 for the system sizes $L = 10$ and 12. For the values of the tunneling parameter $t/V < \bar{t}_c(L,\bar{U})$ the overlaps for all states within the first excited states manifold are $\simeq 1$. In other words, away from the degeneracy point at $U = 2V$ and $t = 0$, the nature and fractional charge of the domain walls do not change if $t/V < \bar{t}_c(L,\bar{U})$. This is of importance for actual experiments, where there is always some finite possibility for atoms tunneling between the lattice sites, and where the values of the on-site and nearest-neighbor interaction strengths can be tuned away from $U = 2V$.

Sudden decrease of the overlap for some of the excited states at $t/V = \bar{t}_c(\bar{U},L)$ is related to the energy level crossings between the states within the first and second excited states manifolds (Fig. 7). Namely, as pointed out in Ref. [18], moving away from the degeneracy point, where domain walls do not interact, introduces interaction between domain walls via a linear potential. The strength and sign of the potential depends on the energy splitting between the CDW states that are degenerate at $U = 2V$ and $t = 0$. For $t/V > \bar{t}_c(L,\bar{U})$, some states with two $\pm q/2$ domain wall pairs are more energetically favorable than some of the states with one $\pm q/2$ domain wall pair due to an attractive linear potential between the domain walls which results in energy level crossings and sudden decrease of the overlap for some of the states within the first excited states manifold.

We also note that the overlaps (16) for $|\bar{\psi}^{(\bar{i})}_{\text{Exact}}\rangle_{\bar{t},\bar{U}}$ ($\bar{i} = 1,...,\bar{N}_L$) taken to be the states adiabatically connected to the states within the first excited states manifold at $t = 0$ (the states with one domain wall pair), also decrease significantly for some of these states when $t/V > \bar{t}_c(\bar{U},L)$, as shown in Fig. 9. In other words, the fractional domain walls do not have non-Abelian statistics for $t/V > \bar{t}_c(\bar{U},L)$, after the crossing between the states within different (quasi)degenerate manifolds.

In addition, for $U < 2V$ increasing the tunneling strength t/V induces the first order phase transition from [30] ([03]) to [21] ([12]) CDW state, as demonstrated previously using the Gutzwiller ansatz wave function [18]. This first order transition, characterized by an energy level crossing, can be clearly seen in the fidelity metric [60–70]. If $|\psi_0(\bar{t})\rangle$ and $|\psi_0(\bar{t}+\delta\bar{t})\rangle$ are two ground states corresponding to slightly different values of the relevant parameter $\bar{t} = t/V$, the fidelity between these two ground states is defined as the modulus of the overlap between the two states:

$$F(\bar{t},\bar{t}+\delta\bar{t}) = |\langle\psi_0(\bar{t}+\delta\bar{t})|\psi_0(\bar{t})\rangle|. \tag{17}$$

The fidelity (17) can further be rewritten as

$$F(\bar{t},\bar{t}+\delta\bar{t}) = 1 - \frac{(\delta\bar{t})^2}{2}\chi_F(\bar{t}) + ..., \tag{18}$$

where $\chi_F(\bar{t})$ is the fidelity susceptibility,

$$\chi_F(\bar{t}) = -\lim_{\delta\bar{t}\to 0}\frac{2\ln F(\bar{t}+\delta\bar{t})}{(\delta\bar{t})^2} = -\frac{\partial^2 F(\bar{t}+\delta\bar{t})}{\partial(\delta\bar{t})^2}. \tag{19}$$

The first order transition between two different CDW states is characterized by a singular peak in the fidelity susceptibility. Namely, since the overlap measures similarity between two states, it equals to one if two states are the same and zero if the states are orthogonal. Consequently, the fidelity shows a very sharp decrease at points where there is a level crossing between two orthogonal states, and decrease in the fidelity corresponds to a singular peak in the fidelity susceptibility. This singular peak can be clearly seen in Fig. 10 at $t/V = \bar{t}_{CDW-CDW}(\bar{U},L)$ corresponding to the value of the tunneling parameter t/V where there is an energy level crossing within the (quasi)degenerate ground-state manifold (Fig. 6).

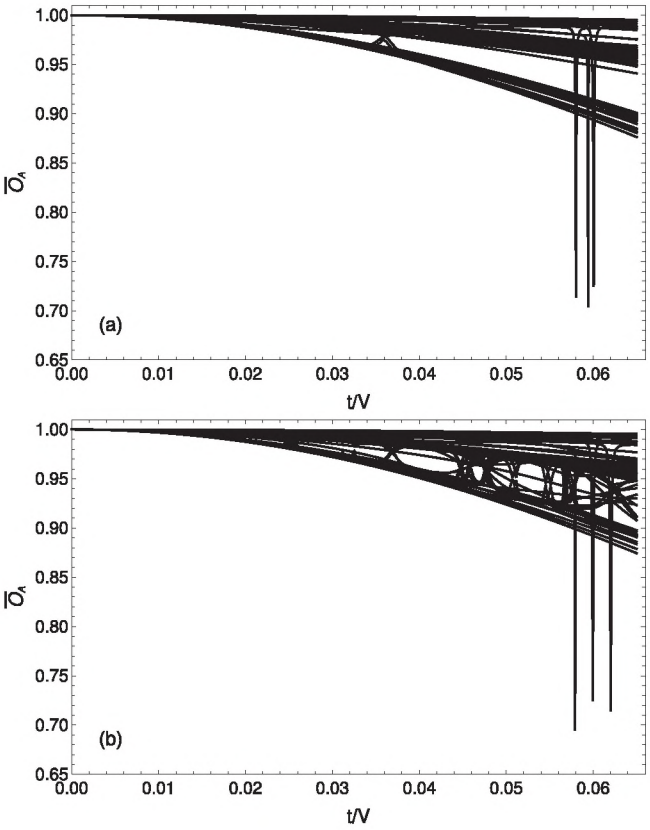

FIG. 9. The overlaps (16) for $|\bar{\psi}^{(\bar{i})}_{\text{Exact}}\rangle_{\bar{t},\bar{U}}$ ($\bar{i} = 1,...,\bar{N}_L$) taken to be the states adiabatically connected to the states within the first excited states manifold at $t = 0$ (the states with one domain wall pair) and for the system size $L = 10$ lattice sites with periodic boundary conditions. Here the on-site interaction strength is (a) $U/V = 2$ and (b) $U/V = 1.99$, with V being the nearest-neighbor interaction.

Further increase of the value of the tunneling strength t/V leads to a CDW to SF quantum phase transition of the BKT type, as will be described in more details in the following section. This phase transition is characterized by a broader peak in the fidelity susceptibility which becomes sharper and sharper as the system size increases. This is clearly visible in Figs. 10, 11, and 12.

The transition is related to a level crossing between the states in the lowest energy, (quasi)degenerate manifold and the states within the first excited, (quasi)degenerate manifold at $t/V = \bar{t}_{CDW-SF}(\bar{U},L)$. The level crossings can be clearly seen in Fig. 5 and Fig. 6 at values of t/V which coincide with the positions of the broader peaks in the fidelity susceptibility.

Our results thus demonstrate that the system undergoes a direct, BKT, CDW to SF quantum phase transition without intermediate SS phases between the CDW and SF regions of the phase diagram. This is in contrast with the results

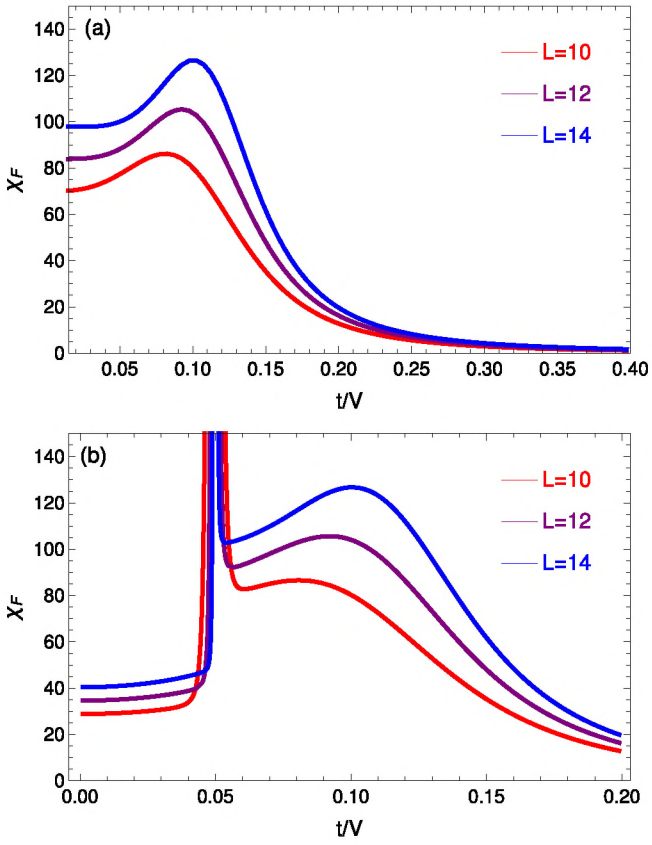

FIG. 10. The fidelity susceptibility χ_F (19) as a function of the tunneling parameter t/V, obtained by ED method for the system sizes $L = 10$, 12, and 14 lattice sites and with periodic boundary conditions. Here the average filling is $\nu = 3/2$ atoms per lattice site and the on-site interaction strength is (a) $U/V = 2$ and (b) $U/V = 1.99$, with V being the nearest-neighbor interaction.

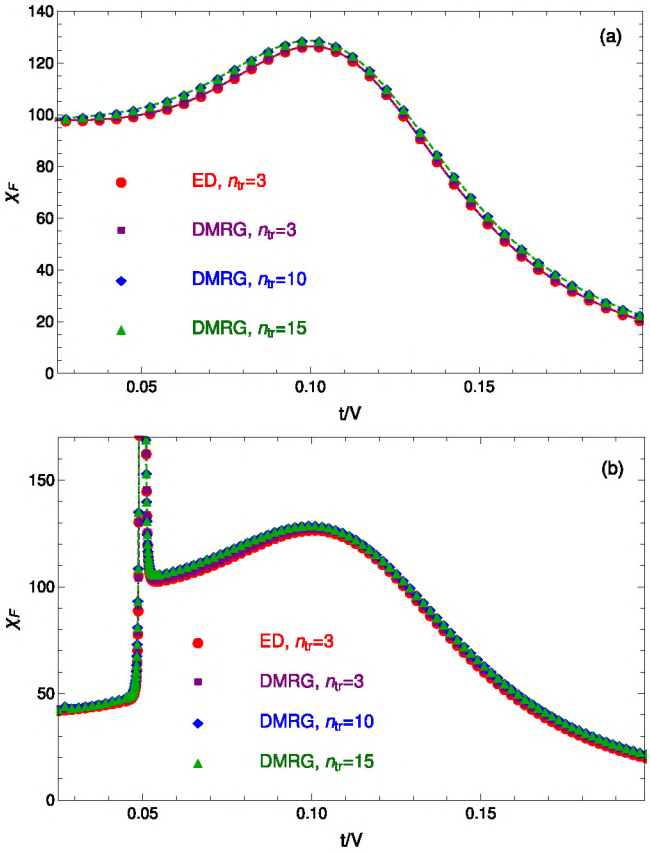

FIG. 11. The ED and DMRG results for the fidelity susceptibility χ_F (19) as a function of the tunneling parameter t/V, for the system size $L = 14$ lattice sites and with periodic boundary conditions, the average filling $\nu = 3/2$ atoms per lattice site, and with the local Hilbert space truncation to single site Fock states with at most $n_{tr} = 3$, 10, and 15 atoms at each lattice site. Here the on-site interaction strength is (a) $U/V = 2$ and (b) $U/V = 1.99$, with V being the nearest neighbor interaction.

obtained previously within the Gutzwiller-ansatz wave function approach [18]. Namely, previous results predicted two different SS phases, SS1 and SS2, separating CDW and SS regions of the phase diagram for $U = 1.99V$. These SS phases are partially melted CDW phases, with SS1 and SS2 having different underlying CDW orders. The Gutzwiller-ansatz wave function calculations [18] also predict CDW to SS1 and SS1 to SS2 transitions to be first order transitions, and SS2 to SF transition to be a second order transition. If SS phases were present in the phase diagram, these transitions would be clearly visible in the fidelity susceptibility. However, we do not find any signatures of such transitions and SS phases in our ED and DMRG results.

We also note that the Gutzwiller-ansatz wave function calculations were performed with the local Hilbert space truncation to single site Fock states $|n_i\rangle$ with at most $n_{tr} = 30$ atoms at each lattice site ($0 \leqslant n_i \leqslant n_{tr}$), while our ED and DMRG calculations were performed with $n_{tr} = 3$. To check that increasing the truncation number n_{tr} does not change qualitatively our results close to the CDW to SF transition, we have performed additional calculations with $n_{tr} = 10$ and $n_{tr} = 15$. The results, shown in Fig. 11 clearly demonstrate that increasing the truncation number n_{tr} introduces only minor changes in the numerical values for the fidelity susceptibility

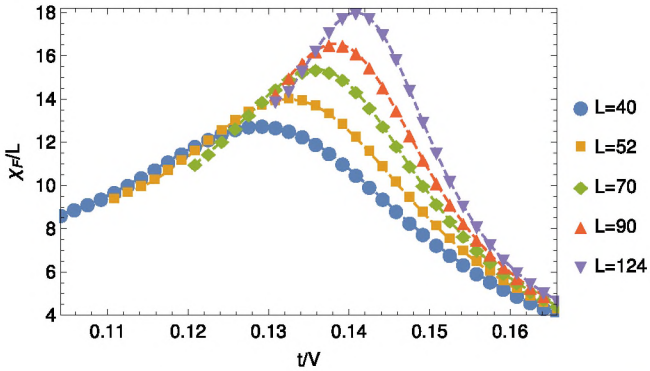

FIG. 12. The DMRG results for the fidelity susceptibility χ_F (19) as a function of the tunneling parameter t/V, for the system sizes $L = 40$–124 lattice sites and with periodic boundary conditions, the average filling $\nu = 3/2$ atoms per lattice site, and with the local Hilbert space truncation to single site Fock states with at most $n_{tr} = 4$ atoms at each lattice site. Here the on-site interaction strength is $U/V = 2$ with V being the nearest-neighbor interaction.

and does not change our results qualitatively. We have also additionally verified that increasing the truncation number $n_{\rm tr}$ to $n_{\rm tr} \leqslant 10$ introduces only minor changes in our DMRG results for larger system sizes.

IV. SUPERFLUID TO CHARGE-DENSITY-WAVE QUANTUM PHASE TRANSITION

To further describe the SF to CDW quantum phase transition we calculate the density-density structure factor at wave number $k = \pi$

$$S_\pi = \frac{1}{N^2} \sum_{i,j=1}^{L} e^{i\pi(i-j)} \langle n_i n_j \rangle, \tag{20}$$

the single particle correlation function

$$\Gamma(|i-j|) = \langle a_i^\dagger a_j \rangle, \tag{21}$$

and the associated system-size-dependent correlation length

$$\xi_L = \sqrt{\frac{\sum_{i,j=1}^{L/2} (i-j)^2 \langle a_i^\dagger a_j \rangle}{\sum_{i,j=1}^{L/2} \langle a_i^\dagger a_j \rangle}}, \tag{22}$$

for the system with L sites and N bosons and with periodic boundary conditions.

We also calculate the von-Neumann block entanglement entropy

$$S_L(l) = -\mathrm{Tr}[\rho_l \ln \rho_l], \tag{23}$$

where ρ_l is the reduced density matrix for the block of length l. From $1+1$ dimensional conformal field theory [71,72] it follows that the von Neumann entanglement entropy at a critical point has the form

$$S_L(l) = \frac{c}{3} \ln \left[\frac{L}{\pi} \sin \left(\frac{\pi l}{L} \right) \right] + s_1 \tag{24}$$

for a system with periodic boundary conditions, with s_1 being a nonuniversal constant and c the central charge of the associated conformal field theory (CFT). Since DMRG calculations give the most precise data for $S_L(l)$ when $l = L/2$ [72,73], the most suited relation to determine the central charge is

$$c^*(L) \equiv \frac{3[S_L(L/2-1) - S_L(L/2)]}{\ln[\cos(\pi/L)]}, \tag{25}$$

where $c^* = c$ when the system is critical. The central charge provides definitive information about the universality class of a $(1+1)$-dimensional system [74]. Our results show that $c = 1$ in the SF regime, where the low energy effective theory for the system, obtained by the Abelian bosonization [75], is the Tomonaga-Luttinger-liquid (TLL) Hamiltonian [76]. Within the non-Abelian bosonization [77] the low energy theory of the SF phase is the Wess-Zumino-Witten (WZW) theory with topological coupling $k = 1$ ($SU(2)_1$ WZW theory) [78] and the conformal anomaly parameter (central charge) $c = 3k/(2+k) = 1$ [78].

The central charge can also be used to determine the critical point between TLL and gapped (or ordered) phases [73]. Namely the critical point corresponds to the maximum of c^* (25) as a function of t/V [73]. The position of the maximum point, $(t/V)_c$, is independent of the system size

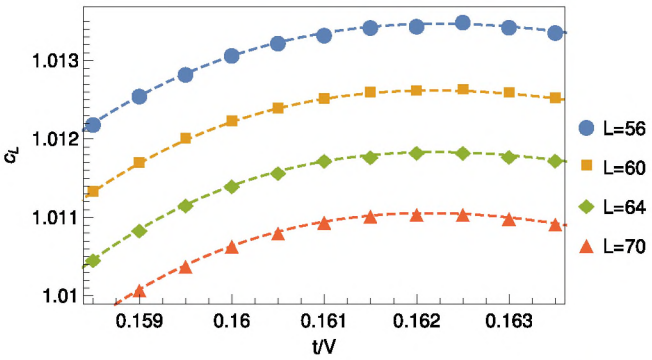

FIG. 13. The DMRG results for the central charge c^* (25) as a function of the tunneling parameter t/V for several system sizes L and with periodic boundary conditions. Here the on-site interaction strength is $U/V = 2$ with V being the nearest-neighbor interaction.

for the model that we have considered (Fig. 13). A similar result was obtained for 1D half-filled spinless fermions with nearest-neighbor repulsion [73].

Our DMRG [54] results show that $(t/V)_c \approx 0.162$ (Fig. 13) for $U/V = 2$. On the right-hand side of the maximum point c^* approaches the value $c = 1$ with increasing system size, and $c^* \to 0$ for the CDW gapped phase. In the DMRG calculations of the central charge dimensions of the matrices in the matrix product state (MPS) wave function were taken to be up to 2200 and $n_{\rm tr} = 4$.

To further characterize the nature of the SF to CDW quantum phase transition we consider the finite-size scaling of the fidelity susceptibility. Within the non-Abelian bosonization approach it was shown that the fidelity susceptibility in the vicinity of a BKT transition has the following logarithmic finite-size scaling [79]

$$\chi_L \simeq \chi_0 - \frac{\chi_1}{\ln(L/a)} + O\left[\frac{1}{\ln^2(L/a)}\right], \tag{26}$$

where a is the lattice cutoff. Also, the finite-size dependence of the peak position in the fidelity susceptibility, that signals the BKT transition, has the following form

$$\bar{t}_c \simeq A + B/\ln^2(L/a) + \cdots, \tag{27}$$

which can be obtained using scaling arguments on the gapped side of the BKT transition [79]. Here $\bar{t} = t/V$. We fit our DMRG data for the fidelity susceptibility to these predicted finite size-scaling behaviors, and the results of these fits demonstrate good agreement with the theory (Fig. 14). This confirms that the SF to CDW quantum phase transition is of the BKT type.

We also point out that $\bar{t}_c(L \to \infty) = A = 0.158 \pm 0.004$ which is consistent (within the error bars) with the value of $\bar{t}_c \approx 0.162$ obtained from the central charge. We have also studied the scaling of the energy gap in the vicinity of the transition [80]. The estimated transition point is then $\bar{t}_c(L \to \infty) = 0.16 \pm 0.004$ in agreement with $\bar{t}_c$ obtained from the fidelity susceptibility studies.

We finally calculate the structure factor (20) close to the SF to CDW quantum phase transition to show that there is a direct phase transition from the SF to CDW phase. The nonzero structure factor characterizes the crystalline order,

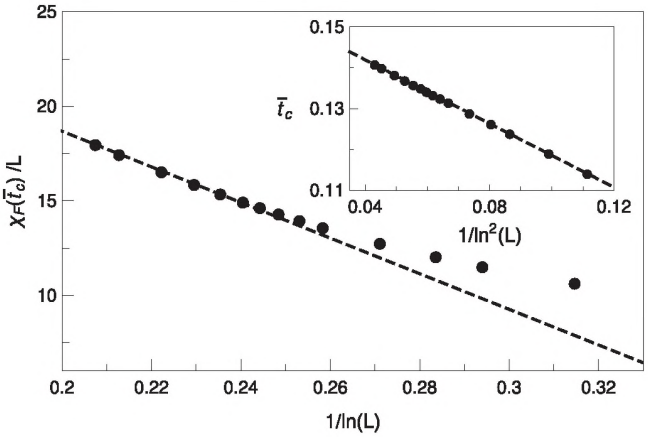

FIG. 14. The finite-size scaling of the peak position $\bar{t}_c$ and amplitude $\chi_L(\bar{t}_c)$ of the fidelity susceptibility. The lines correspond to fits (26) and (27), where $A \approx 0.158$, $B \approx -0.39$, $\chi_0 \approx 37.5$, and $\chi_1 \approx -94.2$. The data are for the system sizes $L = 20$–124 lattice sites and with periodic boundary conditions. Here the on-site interaction strength is $U/V = 2$ with V being the nearest-neighbor interaction.

and in the case of direct transition from the SF phase has the form $S_\pi \sim \xi^{\gamma/\nu}\Phi(\xi/L)$ close to the transition [81,82], where Φ is a scaling function. For the case of a direct transition the structure factor is governed by the correlation length ξ that characterizes SF order and diverges in the SF phase [81,82], which results in the mentioned form of the structure factor close to the transition.

Also, the functional form of the structure factor cannot be transformed to a power law behavior depending on t/V since the correlation length diverges like $\xi \propto \exp(const./\sqrt{(t/V)_c - (t/V)})$ at BKT type transition. Our results for the structure factor are shown in Fig. 15 and confirm that there is a direct SF to CDW transition without

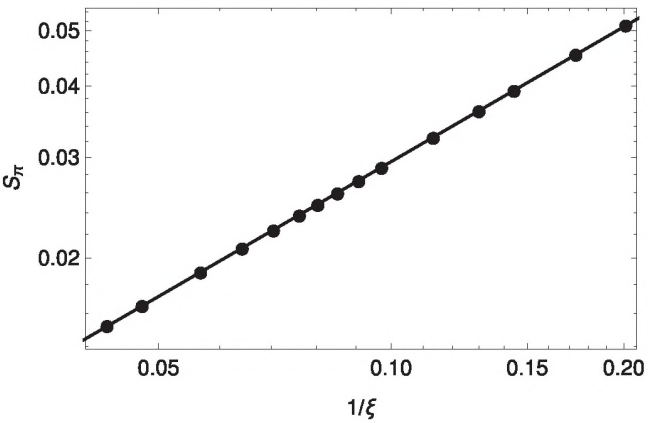

FIG. 15. The structure factor S_π as a function $1/\xi$, where ξ is the correlation length, at the BKT transition of the CDW phase ($t/V \approx 0.158$). The slope is ≈ -0.78 and $S_\pi \propto \xi^{-0.78}$. The data are for the system sizes $L = 20$–124 lattice sites and with periodic boundary conditions. Here the on-site interaction strength is $U/V = 2$ with V being the nearest-neighbor interaction.

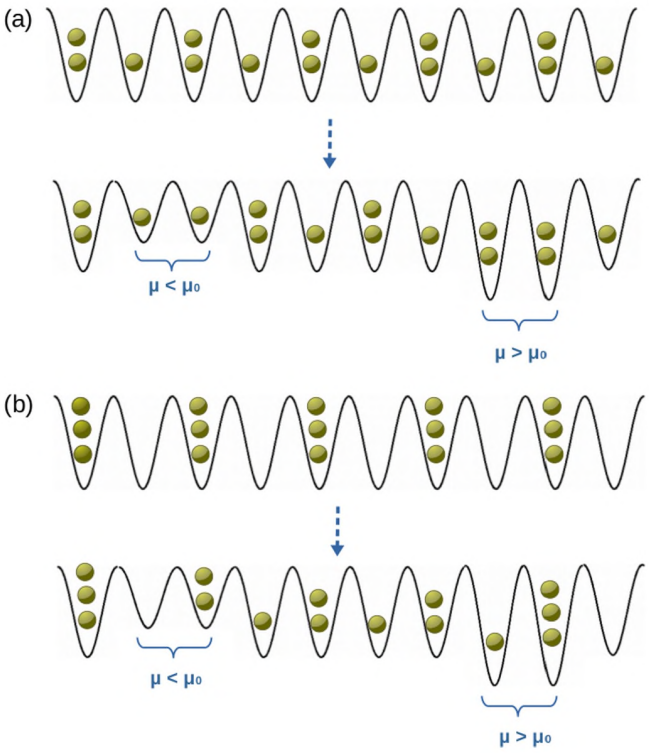

FIG. 16. Schematic demonstration how local changes in the chemical potential can create robust $SU(2)_3$ Fibonacci anyon fractional domain walls which appear in a ground state configuration of the system, as suggested previously in Ref. [18].

intermediate normal or supersolid phases. This is in agreement with previous results found by other authors [21].

V. PROTOCOL FOR BRAIDING FRACTIONAL DOMAIN WALLS

In order to use described fractional domain walls for quantum computation, that is to realize topological quantum gates, one needs to engineer states with robust fractional domain walls in a geometry where these domain walls can be interchanged in a controlled way (braided). To have robust fractional domain walls it is necessary to achieve that these domain walls appear in a ground state configuration of the system. For a fixed filling fraction this can be achieved by locally varying the chemical potential [18] as illustrated in Fig. 16.

Namely, starting from the unperturbed initial configuration, increasing/decreasing the chemical potential on two neighboring sites creates $+q/2/-q/2$ fractional domain walls [18]. The domain walls illustrated in Fig. 16 are $SU(2)_3$ Fibonacci anyons similar to elementary excitations of the bosonic Read-Rezayi state [18,25,27]

$$\psi_{RR} = \mathcal{S}\left(\prod_{i_1<j_1}^{N/k}(z_{i_1}-z_{j_1})^2 \ldots \prod_{i_k<j_k}^{N/k}(z_{i_k}-z_{j_k})^2\right) \prod_{i<j}^{N}(z_i - z_j)^M e^{-(1/4)\sum_i |z_i|^2}, \quad (28)$$

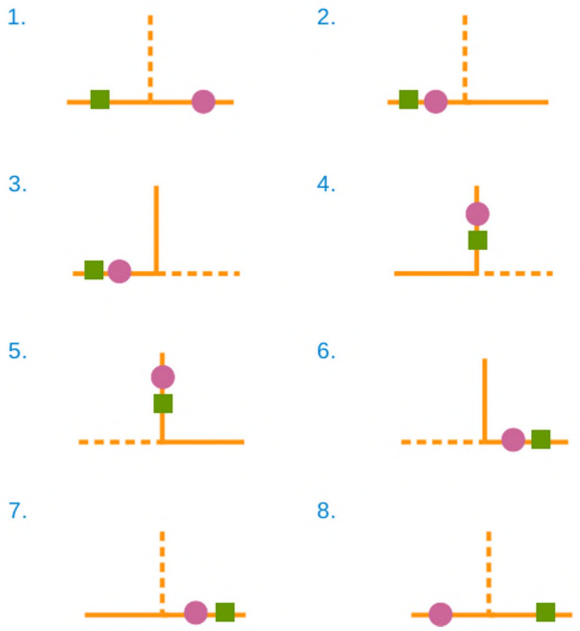

FIG. 17. A T junction which allows adiabatic exchange of two fractional domain walls. In each step of adiabatic exchange a dashed line represents a part of the junction which is disconnected from the part of the junction represented by a solid line. Position of a domain wall on a 1D lattice represented by a solid line can be changed by an adiabatic change of the local chemical potential at corresponding sites of the initial and final positions of the domain wall (Fig. 16).

with $k = 3$ and $M = 0$ and where $\mathcal{S}$ denotes symmetrization over possible divisions of the atoms into k clusters of the same size.

The adiabatic exchange (braiding) of the fractional domain walls is not possible in the strictly 1D system that we have considered. Therefore, to achieve controlled interchange of these non-Abelian defects, and realize topological quantum gates, several such 1D atomic quantum wires need to be combined into a 2D network where 1D wires are connected with T junctions, as proposed previously for Majorana quantum wires [19]. A T junction which allows adiabatic exchange of two fractional domain walls is illustrated in Fig. 17. A part of the T junction which does not contain domain walls can be connected to or disconnected from the part of the junction with two domain walls by adiabatically switching on or off the tunneling between the neighboring sites of the two parts of the junction.

In Fig. 17 a part of the junction that is disconnected from the rest of the junction in each step of the adiabatic exchange of two fractional domain walls is represented by a dashed line. A part of the junction which contains two domain walls is represented in each step by a solid line. Position of a domain wall on a 1D lattice represented by a solid line can be changed by an adiabatic change of the local chemical potential at corresponding sites of the initial and final positions of the domain wall (for example in the step from 1 to 2 in Fig. 17).

We also point out that braiding of fractional domain walls in a T-junction network requires only a few local operations on relevant sites where the local chemical potential and the tunneling strength between the two nearest-neighboring sites needs to be adiabatically changed in each step of the adiabatic exchange of these non-Abelian defects.

These adiabatic changes of the local chemical potential and the tunneling strength between the two nearest-neighboring sites can be achieved experimentally by using local site addressing tools available in current experiments with cold atoms and molecules [83–85]. In cold atom experiments these local operations can be realized in a controllable way by changing the intensity of tightly focused laser fields on the corresponding site or link [83–85].

VI. CONCLUSIONS

We have studied low energy properties of a system of dipolar lattice bosons trapped in a 1D optical lattice and at average filling $\nu = 3/2$ atoms per lattice site. The system can be described by an extended Bose-Hubbard Hamiltonian with the on-site and nearest-neighbor interactions. Using ED and DMRG methods we have identified a region of the phase diagram where the system supports $SU(2)_3$ Fibonacci anyon excitations. The $SU(2)_3$ non-Abelian topological order of the exact wave functions of the Hamiltonian was demonstrated by calculating the overlaps with the ansatz wave functions which have $SU(2)_3$ topological order by construction.

Contrary to previous results obtained within the Gutzwiller ansatz wave-function approach [18], our ED and DMRG results demonstrated that for an average filling of 3/2 the system undergoes a direct, BKT, CDW to SF quantum phase transition when the tunneling strength between the nearest-neighboring sites of the lattice is increased above a certain critical value. We do not find any signatures of the SS phases in the phase diagram of the system, found in Ref. [18] to appear between CDW and SF regions in the parameter space. However, the SS phases are predicted to appear at higher filling fractions [21].

We have also discussed a protocol which would allow creation of robust $SU(2)_3$ fractional domain walls in a ground state configuration of the system and their controlled adiabatic interchange (braiding), with potential application for fault tolerant, universal, topological quantum computation. The domain walls can be introduced in a ground state of the system by changing the local chemical potential on certain lattice sites [18], and braiding can be achieved by combining 1D atomic quantum wires into a 2D network where the 1D wires are connected with T junctions, as previously proposed in the context of Majorana quantum wires [19]. Both creation and braiding of such domain walls are achievable with local site addressing tools available in current cold atom experiments [83–85].

ACKNOWLEDGMENTS

We thank Nicholas Chancellor, Omjyoti Dutta, Bogdan Damski, Benoit Grémaud, and Dominique Delande for very helpful suggestions and discussions. This work was realized under National Science Centre (Poland) Project No. 2015/19/B/ST2/01208 and was supported in part by PL-Grid Infrastructure. We also acknowledge support from the EU Grant QUIC (H2020-FETPROACT-2014, Grant No. 641122).

[1] A. Y. Kitaev, Ann. Phys. (NY) **303**, 2 (2003).
[2] M. H. Freedman, M. Larsen, and Z. Wang, Commun. Math. Phys. **227**, 605 (2002).
[3] S. Das Sarma, M. Freedman, and C. Nayak, Phys. Today **59**(7), 32 (2006).
[4] C. Nayak, S. H. Simon, A. Stern, M. Freedman, and S. Das Sarma, Rev. Mod. Phys. **80**, 1083 (2008).
[5] J. K. Pachos, *Introduction to Topological Quantum Computation* (Cambridge University Press, Cambridge, UK, 2012).
[6] J. K. Pachos and S. H. Simon, New J. Phys. **16**, 065003 (2014).
[7] G. Moore and N. Read, Nucl. Phys. B **360**, 362 (1991).
[8] A. Stern, Ann. Phys. **323**, 204 (2008).
[9] A. Stern, Nature (London) **464**, 187 (2010).
[10] S. Trebst, M. Troyer, Z. Wang, and A. W. W. Ludwig, Prog. Theor. Phys. Supp. **176**, 384 (2008).
[11] S. Das Sarma, M. Freedman, and C. Nayak, Phys. Rev. Lett. **94**, 166802 (2005).
[12] A. Stern and B. I. Halperin, Phys. Rev. Lett. **96**, 016802 (2006).
[13] P. Bonderson, A. Kitaev, and K. Shtengel, Phys. Rev. Lett. **96**, 016803 (2006).
[14] W. Zhu, S. S. Gong, F. D. M. Haldane, and D. N. Sheng, Phys. Rev. Lett. **112**, 096803 (2014).
[15] W. Zhu, S. S. Gong, F. D. M. Haldane, and D. N. Sheng, Phys. Rev. Lett. **115**, 126805 (2015).
[16] A. Y. Kitaev, Ann. Phys. **321**, 2 (2006).
[17] J. C. Y. Teo and C. L. Kane, Phys. Rev. B **89**, 085101 (2014).
[18] E. Wikberg, J. Larson, E. J. Bergholtz, and A. Karlhede, Phys. Rev. A **85**, 033607 (2012).
[19] J. Alicea, Y. Oreg, G. Refael, F. von Oppen, and M. P. A. Fisher, Nat. Phys. **7**, 412 (2011).
[20] E. Ardonne, E. J. Bergholtz, J. Kailasvuori, and E. Wikberg, J. Stat. Mech. (2008) P04016.
[21] G. G. Batrouni, V. G. Rousseau, R. T. Scalettar, and B. Grémaud, Phys. Rev. B **90**, 205123 (2014).
[22] M. Greiter, X. G. Wen, and F. Wilczek, Nucl. Phys. B **374**, 567 (1992).
[23] C. Nayak and F. Wilczek, Nucl. Phys. B **479**, 529 (1996).
[24] N. Read and E. Rezayi, Phys. Rev. B **54**, 16864 (1996).
[25] N. Read and E. Rezayi, Phys. Rev. B **59**, 8084 (1999).
[26] N. K. Wilkin and J. M. F. Gunn, Phys. Rev. Lett. **84**, 6 (2000).
[27] A. Cappelli, L. S. Georgiev, and I. T. Todorov, Nucl. Phys. B **599**, 499 (2001).
[28] N. R. Cooper, N. K. Wilkin, and J. M. F. Gunn, Phys. Rev. Lett. **87**, 120405 (2001).
[29] V. Gurarie and L. Radzihovsky, Ann. Phys. **322**, 2 (2007).
[30] G. Möller and N. R. Cooper, Phys. Rev. Lett. **103**, 105303 (2009).
[31] T. Đurić, and A. Lazarides, Phys. Rev. B **86**, 115135 (2012).
[32] Y.-H. Wu and J. K. Jain, Phys. Rev. B **87**, 245123 (2013).
[33] A. Sterdyniak, B. A. Bernevig, N. R. Cooper, and N. Regnault, Phys. Rev. B **91**, 035115 (2015).
[34] L. Fu and C. L. Kane, Phys. Rev. Lett. **100**, 096407 (2008).
[35] L. Fu and C. L. Kane, Phys. Rev. Lett. **102**, 216403 (2009).
[36] J. Nilsson, A. R. Akhmerov, and C. W. J. Beenakker, Phys. Rev. Lett. **101**, 120403 (2008).
[37] P. Nikolić, T. Đurić, and Z. Tešanović, Phys. Rev. Lett. **110**, 176804 (2013).
[38] J. D. Sau, R. M. Lutchyn, S. Tewari, and S. Das Sarma, Phys. Rev. Lett. **104**, 040502 (2010).
[39] M. A. Levin and X. G. Wen, Phys. Rev. B **71**, 045110 (2005).
[40] A. M. Tsvelik, Sov. J. Nucl. Phys. **47**, 172 (1988) [Yad. Fiz. **47**, 272 (1988)].
[41] A. M. Tsvelik, Phys. Rev. Lett. **113**, 066401 (2014).
[42] P. Fendley and H. Saleur, Phys. Rev. D **65**, 025001 (2001).
[43] H.-H. Tu, Phys. Rev. B **87**, 041103(R) (2013).
[44] B. Paredes, T. Keilmann, and J. I. Cirac, Phys. Rev. A **75**, 053611 (2007).
[45] B. Paredes, Phys. Rev. B **85**, 195150 (2012).
[46] A. E. B. Nielsen, J. I. Cirac, and G. Sierra, J. Stat. Mech. (2011) P11014.
[47] M. Greiter, *Mapping of Parent Hamiltonians: From Abelian and Non-Abelian Quantum Hall States to Exact Models of Critical Spin Chains. Springer Tracts in Modern Physics, Vol. 244* (Springer-Verlag, Berlin, 2011).
[48] R. Thomale, S. Rachel, P. Schmitteckert, and M. Greiter, Phys. Rev. B **85**, 195149 (2012).
[49] T. Đurić, N. Chancellor, P. J. D. Crowley, P. Di Cintio, and A. G. Green, Phys. Rev. B **93**, 085143 (2016)
[50] J. Alicea and P. Fendley, Annu. Rev. Condens. Matter Phys. **7**, 119 (2016).
[51] B. Paredes, arXiv:1402.3567.
[52] S. R. White, Phys. Rev. Lett. **69**, 2863 (1992).
[53] U. Schollwöck, Rev. Mod. Phys. **77**, 259 (2005).
[54] DMRG calculations were performed using ITensor library, http://itensor.org/.
[55] A. Vaezi, Phys. Rev. X **4**, 031009 (2014).
[56] A. Vaezi and M. Barkeshli, Phys. Rev. Lett. **113**, 236804 (2014).
[57] M. Oshikawa and T. Senthil, Phys. Rev. Lett. **96**, 060601 (2006).
[58] M. Oshikawa, Y. B. Kim, K. Shtengel, C. Nayak, and S. Tewari, Ann. Phys. **322**, 1477 (2007).
[59] R. B. Laughlin, Phys. Rev. Lett. **50**, 1395 (1983).
[60] C. N. Varney, K. Sun, M. Rigol, and V. Galitski, Phys. Rev. B **84**, 241105(R) (2011).
[61] T. Đurić, N. Chancellor, and I. F. Herbut, Phys. Rev. B **89**, 165123 (2014).
[62] Z. Wang, Q.-F. Liang, and D.-X. Yao, Phys. Lett. A **377**, 2653 (2013).
[63] S.-J. Gu, Int. J. Mod. Phys. B **24**, 4371 (2010).
[64] D. F. Abasto, A. Hamma, and P. Zanardi, Phys. Rev. A **78**, 010301(R) (2008).
[65] E. Eriksson and H. Johannesson, Phys. Rev. A **79**, 060301(R) (2009).
[66] C. N. Varney, K. Sun, M. Rigol, and V. Galitski, Phys. Rev. B **82**, 115125 (2010).
[67] P. Zanardi and N. Paunković, Phys. Rev. E **74**, 031123 (2006).
[68] L. Campos Venuti and P. Zanardi, Phys. Rev. Lett. **99**, 095701 (2007).
[69] M. Rigol, B. S. Shastry, and S. Haas, Phys. Rev. B **80**, 094529 (2009).
[70] C. N. Varney, K. Sun, V. Galitski, and M. Rigol, Phys. Rev. Lett. **107**, 077201 (2011).
[71] P. Calabrese and J. Cardy, J. Stat. Mech. (2004) P06002.
[72] S. Ejima and H. Fehske, Phys. Rev. B **91**, 045121 (2015).
[73] S. Nishimoto, Phys. Rev. B **84**, 195108 (2011).
[74] J. Cardy, *Scaling and Renormalization in Statistical Physics* (Cambridge University Press, Cambridge, 1996).
[75] T. Giamarchi, *Quantum Physics in One Dimension* (Oxford University Press, Oxford, 2003).

[76] F. D. M. Haldane, J. Phys. C: Solid State Phys. **14**, 2585 (1981).
[77] I. Affleck, Phys. Rev. Lett. **55**, 1355 (1985).
[78] I. Affleck and F. D. M. Haldane, Phys. Rev. B **36**, 5291 (1987).
[79] G. Sun, A. K. Kolezhuk, and T. Vekua, Phys. Rev. B **91**, 014418 (2015).
[80] J. Carrasquilla, S. R. Manmana, and M. Rigol, Phys. Rev. A **87**, 043606 (2013).
[81] T. D. Kühner and H. Monien, Phys. Rev. B **58**, R14741(R) (1998).
[82] T. D. Kühner, S. R. White, and H. Monien, Phys. Rev. B **61**, 12474 (2000).
[83] C. Weitenberg, M. Endres, J. F. Sherson, M. Cheneau, P. Schauß, T. Fukuhara, I. Bloch, and S. Kuhr, Nature (London) **471**, 319 (2011).
[84] T. Fukuhara, A. Kantian, M. Endres, M. Cheneau, P. Schauß, S. Hild, D. Bellem, U. Schollwöck, T. Giamarchi, C. Gross, I. Bloch, and S. Kuhr, Nat. Phys. **9**, 235 (2013).
[85] C. V. Kraus, P. Zoller, and M. A. Baranov, Phys. Rev. Lett. **111**, 203001 (2013).

Extended Bose-Hubbard model with dipolar and contact interactions

Krzysztof Biedroń,[1] Mateusz Łącki,[1] and Jakub Zakrzewski[1,2]
[1]*Instytut Fizyki imienia Mariana Smoluchowskiego, Uniwersytet Jagielloński, Łojasiewicza 11, 30-048 Kraków, Poland*
[2]*Mark Kac Complex Systems Research Center, Jagiellonian University, Łojasiewicza 11, 30-348 Kraków, Poland*

(Received 2 March 2018; revised manuscript received 23 May 2018; published 5 June 2018)

We study the phase diagram of the one-dimensional boson gas trapped inside an optical lattice with contact and dipolar interaction, taking into account next-nearest terms for both tunneling and interaction. Using the density-matrix renormalization group, we calculate how the locations of phase transitions change with increasing dipolar interaction strength for average density $\rho = 1$. Furthermore, we show the emergence of pair-correlated phases for a large dipolar interaction strength and $\rho \geqslant 2$, including a supersolid phase with an incommensurate density wave ordering manifesting the corresponding spontaneous breaking of the translational symmetry.

DOI: 10.1103/PhysRevB.97.245102

I. INTRODUCTION

Ultracold gases loaded in optical lattices enable simulation of a broad range of lattice gas models, most prominently the Bose-Hubbard (BH) model [1] with Mott insulator (MI) to superfluid (SF) quantum phase transition [2]. Precise control of model parameters is achieved by optical potential manipulation or by advanced techniques such as Feshbach resonances [3,4]. Long-range dipolar interparticle interactions are often taken into account by adding a simple nearest-neighbor interaction term resulting in the extended Bose-Hubbard (EBH) model, which has been the topic of numerous theoretical [5–16] and experimental [17] works.

A feature of ultracold gases is the ability to control the geometry of the underlying optical lattice potential or even the possibility of implementation of a more complex unit cell. The boundary conditions of the potentials can be set by an external harmonic or a box trap, leading to the open boundary conditions (OBCs) [18,19], or by arranging a system into a ringlike or cylinderlike geometry [20,21], thus implementing periodic boundary conditions (PBCs). Notably, one-dimensional systems offer the possibility of efficient many-body numerical simulations of the resulting lattice models by a family of methods related to the density-matrix renormalization group (DMRG) [22,23].

For one-dimensional lattices the EBH model features not only MI and SF phases but also an isolator density wave (DW) characterized by infinite-range spatial order, a topologically protected Haldane insulator (HI) with a nonzero value of the string order parameter, and supersolid (SS) phases which show both spatial ordering and superfluid behavior [24–26]. It has also been suggested that at the mean density $\rho = 3/2$ the EBH model features Fibonacci anyon excitations [27,28] corresponding to fractional domain walls between different DW phases. In this context, the mean-field analysis [27] predicted the existence of the SS phase between DW and SF phases, in contrast to the DMRG calculation [28].

The necessary strength of the dipole-dipole interactions is achieved for isotopes of dysprosium and erbium [29,30], Feshbach molecules [31], and polar molecules [32–34]. More exotic phases such as checkerboard and stripe-ordered phases are possible for higher-dimensional lattices [35–40] (for a review see [13]).

The BH and EBH models are motivated by an expansion of the field operators in the discrete basis defined by Wannier functions [1,41] for the optical potential, followed by truncating the physics to the lowest Bloch band and neglecting hopping beyond the nearest neighbors. The BH model includes only on-site interactions, while the EBH also contains density-density interactions on the nearest-neighbor sites. The rigor of this procedure has been the topic of extended research in the presence of fast-time dependence [42,43] and strong interatom interactions manifesting as so-called density-dependent tunnelings [13,32,44] and even as a renormalization of model parameters due to a virtual population of higher bands [45–47]. Moreover, the coupling beyond the nearest neighbor has been included in studies which treated shallow optical lattices [48,49] and for strongly interacting dipolar systems [50]. In the latter case the extra couplings led to the appearance of spatially ordered phases [35].

Extensive studies of the EBH-like models mentioned in this section were mostly done by scanning the parameter space of the constructed Hamiltonians at a chosen mean density or possibly under other constraints such as a ratio between parameters. In this study we take a more systematic approach to obtain the Hamiltonian for a dipolar gas of ultracold atoms in the optical lattice and study its phase diagram. First, our intent is to modify only experimentally accessible parameters such as the optical lattice potential depth, the scattering length for contact interactions, the dipole-dipole interaction strength, and the mean density of the gas. Second, we chose to keep all the relevant tight-binding terms describing tunneling and interactions. In this way the parameters of the obtained EBH-like Hamiltonians yield a realizable physical model. In other words we get natural constraint values of the parameters. This saves us from considering parameter ranges unaccessible experimentally. In the phase diagram defined by the experimentlike control knobs, we predict modifications of up-to-date theoretical results going beyond a simple readjustment of phase boundaries. In particular we provide evidence for the

emergence of a new phase: a pair superfluid phase with an incommensurate density wave order.

In Sec. II we derive the model from the microscopic principles identifying the realistic parameter set relevant for ultracold dipolar atoms and ultracold dipolar molecules. The phase diagrams for the system are presented in Sec. III (for the case of unit density in the lattice) and Sec. IV (for the case of other densities). In Sec. V we provide the final conclusions and outlook. We finish with three Appendixes describing in detail the computational methods used throughout the paper: in Appendix A we present our method of calculating the terms present in the Hamiltonian, Appendix B contains the parameters used in our DMRG runs, and in Appendix C we describe the DMRG method used in Sec. IV.

II. MODEL

The realistic Hamiltonian that models ultracold bosonic gas in the one-dimensional optical lattice potential considered in this work has the form

$$\begin{aligned} H =& -t\sum_{i=1}^{L-1}(b_i^\dagger b_{i+1}+\text{H.c.}) - t_{\text{nnn}}\sum_{i=1}^{L-2}(b_i^\dagger b_{i+2}+\text{H.c.}) \\ &+\frac{U}{2}\sum_{i=1}^{L} n_i(n_i-1) + V\sum_{i=1}^{L-1} n_i n_{i+1} + V_{\text{nnn}}\sum_{i=1}^{L-2} n_i n_{i+2} \\ &- T\sum_{i=1}^{L-1}[b_i^\dagger(n_i+n_{i+1})b_{i+1}+\text{H.c.}], \end{aligned} \tag{1}$$

where t, T, and V denote the amplitude for standard, nearest-neighbor tunnelings, the amplitude of density-dependent tunnelings resulting from interactions, and the strength of interactions between nearest-neighbor sites, respectively. The terms proportional to t_{nnn} and V_{nnn} are, respectively, the tunneling and strength of interaction between next-nearest-neighbor lattice sites.

The Hamiltonian (1) in its full glory is a result of a realistic tight-binding approximation to the many-body formulation continuous in space, as given by the second quantization. We consider an ultracold gas of atoms or molecules of mass m in the separable optical potential created by three pairs of standing waves of lasers with a wavelength λ_L which takes the form $V_{\text{opt}}(\mathbf{r}) = V_x\cos^2(k_L x) + V_y\cos^2(k_L y) + V_z\cos^2(k_L z)$, with $k_L = 2\pi/\lambda_L$. The recoil energy $E_R = \hbar^2 k_L^2/2m$ defines a natural energy scale for the single-particle physics. We take $V_y = V_z = 50E_R$ and $V_x \ll V_y, V_z$, which freezes the motion in directions y and z and leaves an effectively one-dimensional motion along the x axis. We can recover the parameters of (1) from (for more details see Appendix A)

$$\begin{aligned} H =& \int \psi^\dagger(r)\left[-\frac{\hbar^2\nabla^2}{2m} + V_{\text{opt}}(\mathbf{r})\right]\psi(r) \\ &+ \int \psi^\dagger(\mathbf{r})\psi^\dagger(\mathbf{r}')V(\mathbf{r}'-\mathbf{r})\psi(\mathbf{r}')\psi(\mathbf{r})d^3\mathbf{r}d^3\mathbf{r}'. \end{aligned} \tag{2}$$

The function $V(\mathbf{r})$ represents the sum of contact (V_c) and dipolar (V_d) interactions, $V(\mathbf{r}) = V_c(\mathbf{r}) + V_d(\mathbf{r})$, where

$$V_c(\mathbf{r}) = \frac{4\pi\hbar^2 a_s}{m}\delta(\mathbf{r}), \quad V_d(\mathbf{r}) = \frac{C_{dd}}{4\pi}\frac{1-3\cos^2\theta}{r^3}, \tag{3}$$

with θ being the angle between the direction of polarization and $\mathbf{r}$ and a_s being the scattering length for effective contact interactions [6].

The value of C_{dd} depends on the strength of dipolar interactions and has the form

$$C_{dd} = \begin{cases} \mu_0\mu_m^2, & \text{for magnetic dipole moment } \mu_m, \\ \mu_e^2/\epsilon_0, & \text{for electric dipole moment } \mu_e. \end{cases} \tag{4}$$

Later we will use a representation of the dipolar interaction strength by a dimensionless quantity:

$$d = \frac{mC_{dd}}{2\pi^3\hbar^2 a}. \tag{5}$$

In effect, we have two parameters, V_x and a_s, that can be controlled in the experiment (using the previously mentioned Feshbach resonance) and d, which depends on the kind of particles used in an experiment (we can, however, modify the strength of dipolar interactions by changing the direction of polarization). In the case of molecules, d can be controlled by the external electric field inducing the dipole moment. In this work, we set the dipole direction to be perpendicular to that of the lattice, so that dipolar interactions are maximally repulsive. Then, for given values of U/t and V/t, the appropriate values of V_x and a_s can be found, which in turn determines the values of t_{nnn}/t, V_{nnn}/t, and T/t.

Let us remark that one can, in principle, employ a transverse harmonic confinement of the boson gas [32] to change the relative values of the parameters of dipolar interactions. We have found that while it does provide more control over the values of T/t, ultimately, they have a magnitude similar to what we obtain solely with V_{opt}, and so we refrain from including that method in our considerations.

We denote the values of V and U restricted to only contact (dipolar) interactions as V_c (V_d) and U_c (U_d). In the most common parameter range used in this paper, V/U is of the order of 1. For the optical lattice that we consider (Appendix A), both V_c/U_c and V_d/U_d are smaller than 10^{-1} (see the inset in Fig. 1). Consequently, for a given positive value of d, the value of a_s has to be negative in order to lower the value of U to achieve the desired V/U.

We now take a closer look at how changes in the dipolar interaction strength influence the validity of using (1) for a fixed phase diagram point $(U/t, V/t)$. V_d and U_d increase linearly with d, and so must $|a_s|$ if we want to maintain the desired ratio of V/U. To keep V/t (which is approximately V_d/t) and U/t unchanged, the lattice must be made shallower (as t depends solely on V_x). Since the tight-binding approximation is no longer correct for shallow lattices, this provides an effective upper limit for t, which gets stricter as d increases. The maximum value of d we consider in this paper is 0.1, which corresponds to V_x being roughly equal to $2.5E_R$ for the exemplary values of $U/t = 2$ and $V/t = 1.5$ (see Fig. 1, where we also plot the resulting values of V_{nnn}/t, T/t, and t_{nnn}/t).

To give an example of the magnitude of d for real atoms and molecules, we first assume the lattice constant is $a = 532\,\text{nm}$. Single atoms have weak dipole moments (for ^{52}Cr, $d \approx 9.7\times10^{-4}$; for ^{168}Er, $d \approx 4.3\times10^{-3}$; and for ^{164}Dy, $d \approx 8.5\times10^{-3}$) [29,30,40]. The values for molecules can be a few orders of magnitude greater (for $^{168}\text{Er}_2$, $d \approx 0.1$) [4]. It is worth noting that multiple experimental methods of decreasing

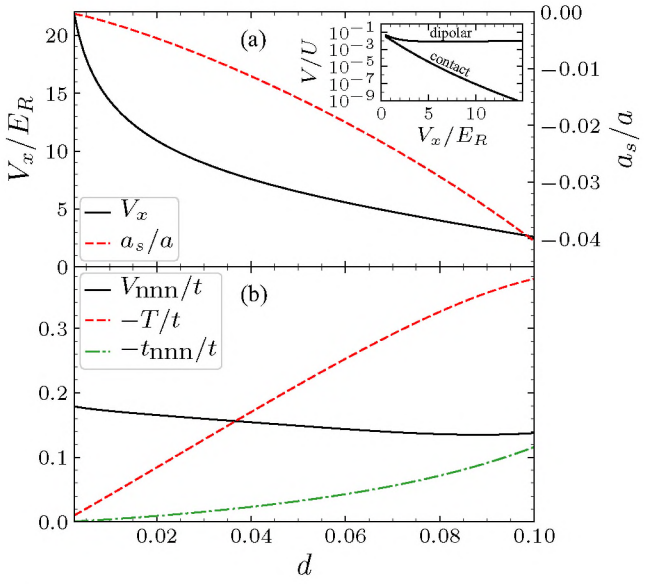

FIG. 1. (a) Values of V_x and a_s/a necessary to get $U/t = 2$ and $V/t = 1.5$ for different values of d. (b) Values of parameters in Hamiltonian (1) in such a case. The inset shows the values of V/U for dipolar-only and contact-only terms.

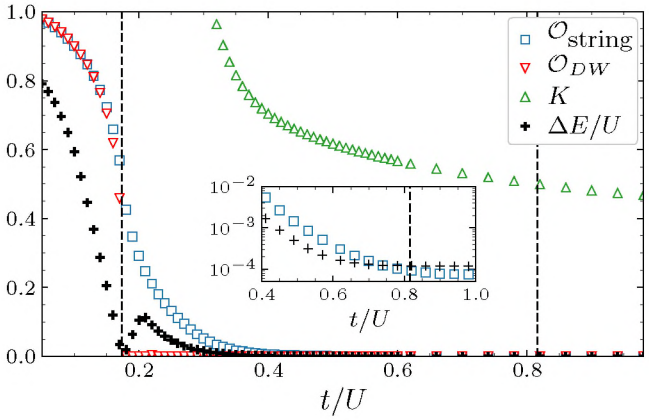

FIG. 2. The values of the string and DW order parameters, critical exponent K, and energy gap ΔE for $V/U = 3/4$, $d = 0.02$. The positions of black dashed vertical lines correspond to the critical values of t/U for DW-HI and HI-SF transitions ($t_c^{\rm DW-HI}/U \approx 0.175$ and $t_c^{\rm HI-SF} \approx 0.82$). The inset shows a logarithmic plot of $\mathcal{O}_{\rm string}$ and ΔE near the HI-SF transition.

a in optical lattices [which would increase d; see Eq. (5)] by a factor of 2 or 3 (with the prospect for a larger value) have been developed and tested [51–54].

III. THE PHASE TRANSITIONS AT $\rho = 1$

The full phase diagram calculated numerically for the EBH model with t, U, and V as the only parameters and a unit mean density $\rho = 1$ has been studied in detail already [24,25], and here we will only briefly sum up the possible phases observed in the $(V/t, U/t)$ plane. For large values of t, the system is in the SF phase, whereas large values of U/t with small V/t drive the system into the MI. Large enough values of V/t for a sufficient U/t put the system in the DW phase. The HI is present on the phase diagram in between the three previously mentioned phases, that is, for intermediate values of both V/t and U/t.

In this section we will calculate how the locations of the transitions between these phases change for the Hamiltonian (1), depending on dipolar interaction strength d. We will not, however, recover a full phase diagram, and instead, we focus on two lines, given by the constraints $V/U = 0.75$ and $U/t = 3$. The first of these values is chosen because it covers three of the phases achievable in the EBH model (DW, HI, and SF) and has already been extensively analyzed [25,26], while the second one allows us to examine the MI phase (in addition to DW and HI, which are also present in that case).

In order to determine the boundaries between different phases, we define their characteristic properties: (1) for DW, $\mathcal{O}_{\rm DW} \neq 0$, $\Delta E \neq 0$, (2) for MI, $\mathcal{O}_{\rm DW} = 0$, $\mathcal{O}_{\rm string} = 0$, $\Delta E \neq 0$, (3) for HI, $\mathcal{O}_{\rm DW} = 0$, $\mathcal{O}_{\rm string} \neq 0$, $\Delta E \neq 0$, and (4) for SF, $\mathcal{O}_{\rm DW} = \mathcal{O}_{\rm string} = 0$, $\Delta E = 0$. Order parameters are defined similarly to those in [24], $\mathcal{O}_p \equiv \lim_{r\to\infty} C_p$, for the following correlators:

$$C_{\rm SF}(r) = \langle b_j^\dagger b_{j+r}\rangle\,, \tag{6}$$

$$C_{\rm DW}(r) = (-1)^r\,\langle \delta n_j \delta n_{j+r}\rangle\,, \tag{7}$$

$$C_{\rm string}(r) = \langle \delta n_j e^{i\pi\sum_{j\leqslant k\leqslant j+r}\delta n_k}\delta n_{j+r}\rangle\,, \tag{8}$$

where $\delta n_j = n_j - \rho$. The energy gap and its thermodynamic limit extrapolation are defined simply as $\Delta E(L) = E^{(1)}(L) - E^{(0)}(L)$ and $\Delta E = \lim_{L\to\infty}\Delta E(L)$, where $E^{(k)}(L)$ is the energy of the kth excited state in a lattice of length L ($k = 0$ is the ground state).

We will also be using the fact that for the superfluid phase it can be shown, using the Luttinger liquid theory, that the correlations in the system show power-law decay [55]:

$$C_{\rm SF}(r) \sim r^{-K/2}. \tag{9}$$

A. $V/U = 0.75$ constraint

We present the results of our calculations for the model (1) obtained using the DMRG method described in Appendix B. For t/U close to zero the system is in the DW phase. As the value of t/U is increased, the first transition is a DW-HI transition at $t_c^{\rm DW-HI}/U$. The transition location can be easily determined because for $t = t_c^{\rm DW-HI}$ (1) the gap ΔE closes and (2) the order parameter $\mathcal{O}_{\rm DW}$ vanishes (see Fig. 2, where the values of the order parameters are plotted for $d = 0.02$). ΔE is linear with respect to t/U on both sides of the transition, which allows us to easily determine where the gap closes. Additionally, the function $a[(t - t_c)/U]^{-b}$ can be fitted to the numerically computed $\mathcal{O}_{\rm DW}$ near the transition point for $t/U < t_c^{\rm DW-HI}/U$. The values of t_c/U obtained with these methods are in agreement with each other (with a difference of less than 5×10^{-3} for every value of d that was considered).

For even larger t, the consecutive transition occurs between the HI and SF phases, but the determination of its location, $t_c^{\rm HI-SF}/U$, proves to be more difficult. As in the earlier case,

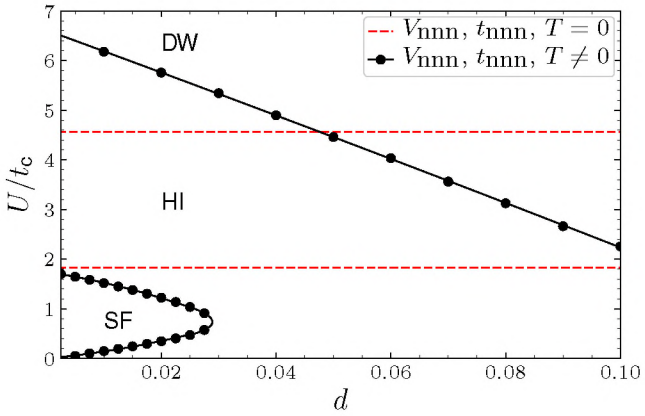

FIG. 3. Critical values of U/t for DW-HI and HI-SF transitions, $V/U = 3/4$ (black solid lines), and the same for a model with $V_{\rm nnn}$, $t_{\rm nnn}$, and T set to zero (red dashed lines).

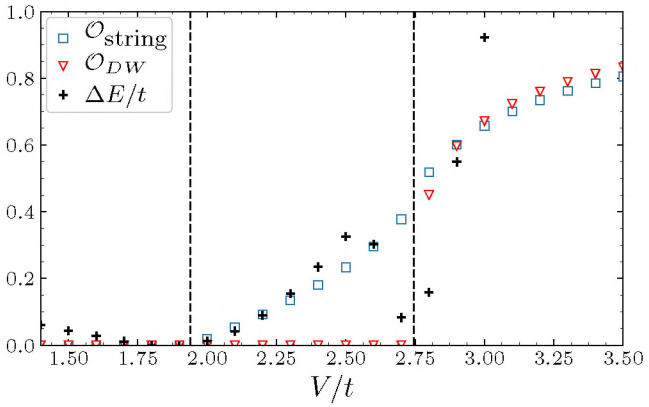

FIG. 4. The values of the order parameters (6), (7), and (8) for $U/t = 3$, $d = 0.09$. The positions of the black dashed vertical lines correspond to the critical values of V/t for DW-HI and HI-MI transitions ($V/t_c^{\rm HI-MI} \approx 1.94$ and $V/t_c^{\rm DW-HI} \approx 2.74$).

the energy gap closes, and the appropriate order parameter ($\mathcal{O}_{\rm string}$) goes to zero. However, the decay of both ΔE and $\mathcal{O}_{\rm string}$ features an exponential tail and does not provide a clear value of the transition point (see the inset of Fig. 2). In order to determine the correct value, we fit the correlations $C_{\rm SF}(r)$ for each L according to (9) and then extrapolate the obtained K to the $L \to \infty$ limit. It has been shown [56] that $K = 0.5$ for $\rho = 1$ at the transition between insulator and superfluid phases. That is the criterion we use here to determine $t_c^{\rm HI-SF}/U$.

The results of the analysis described above are shown in Fig. 3, where the dependence on the chosen d value for both DW-HI and HI-SF transitions is plotted as black solid lines. The results of similar calculations but with parameters $V_{\rm nnn}$, $t_{\rm nnn}$, and T set to zero are marked with the vertical red dashed lines. The U/t_c value for the DW-HI transition has a strong, linear dependence on d, and the transition point is moved considerably for both small and large values of d in the chosen interval ($0 < d \leqslant 0.1$). The situation is different for the HI-SF transition; while for values of d close to zero U/t_c is almost the same as for an ordinary EBH, the SF phase disappears completely around $d = 0.03$. What can also be seen for the intermediate values of d is that for small U/t_c another transition appears; in simulations we see the reemergence of the HI phase, indicated by a rise in $\mathcal{O}_{\rm string}$, ΔE, and K (the transition point is once again pinpointed by the equation $K = 0.5$). The striking substantial difference between the two models indicates that real care has to be taken when applying the tight-binding approximate Hamiltonian to a given physical system.

B. $U/t = 3$ constraint

In this case, two transitions exist between three insulating phases: DW-HI and HI-MI. The method of locating the HI-DW transition is the same as in Sec. III A (the corresponding plot of order parameters for $U/t = 3$ and $d = 0.09$ is shown in Fig. 4). For the HI-MI transition a different approach must be undertaken, as ΔE does not have a linear dependence on t near the transition point. To determine V/t_c we find the minimum of ΔE with respect to V/t for each available L, and then we extrapolate it for $L \to \infty$ using a power function $aL^{-b} + V/t_c$ (see Fig. 5).

We plot the results in Fig. 6, comparing them with the results obtained for a pure EBH model, i.e., setting $V_{\rm nnn}$, $t_{\rm nnn}$, and T in (1) to zero. While the changes are not as drastic as for fixed $V/U = 0.75$, the HI phase gets narrower with respect to V/t as d increases.

IV. THE PHASE DIAGRAM FOR $d = 0.1$

In this section, we characterize the phase diagram without constraining the density of particles ρ while setting $V/U = 0.75$ and $d = 0.1$. The results for an ordinary EBH model, obtained mostly using quantum Monte Carlo methods, can be found in [15,25]. To this end we calculate the ground-state energies using DMRG with OBCs (for technical details see Appendix B) for ρ corresponding to each of the DW phases present in the system for vanishing tunnelings. It is easy to convince oneself that the DW phase requires a commensurate relation between the number of particles and number of sites. Restricting the calculation to next-nearest-neighbor interactions, the corresponding densities are $\rho_{\rm DW} = n_{\rm DW}/4$, where $n_{\rm DW} \geqslant 2$, $n_{\rm DW} \in \mathbb{Z}$. Repeating the same calculations

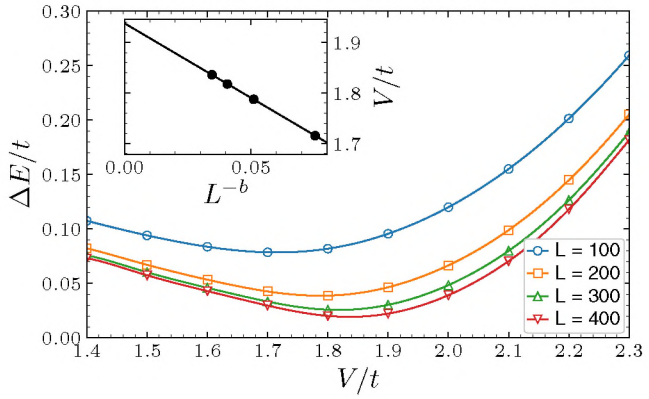

FIG. 5. The energy gap for different system sizes and $U/t = 3$, $d = 0.09$. The inset shows an extrapolation for $L \to \infty$, $b \approx 0.56151$.

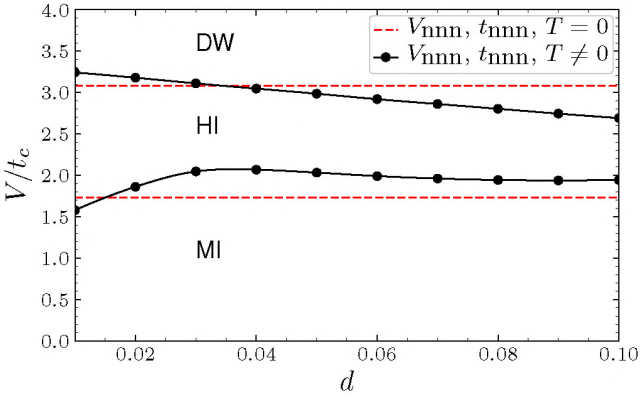

FIG. 6. Critical values of V/t for DW-HI and HI-SF transitions, $U/t = 3$ (black solid lines), and the same for a model with $V_{\rm nnn}$, $t_{\rm nnn}$, and T set to zero (red dashed lines).

with particles added or removed from the system allows us to obtain the chemical potential: $\mu(N,L) = \partial E(N,L)/\partial N$. We can then get the boundaries of DW phases as a discontinuity in $\mu(N,L)$ at $N_{\rm DW} = \rho_{\rm DW} L$. The lower boundary for the DW phase is then given by $\mu^- = \lim_{N \to N^+_{\rm DW}} \mu(N,L)$, while the upper one is given by $\mu^+ = \lim_{N \to N^-_{\rm DW}} \mu(N,L)$. By adjusting the system size we verify that systems with $L = 200$ are sufficiently large to properly determine the values of μ_L and μ_U; for most of the boundary $\mu^- = E(N,L) - E(N-1,L)$, and $\mu^+ = E(N+1,L) - E(N,L)$ [the only exception is the cusps at the rightmost edges of the DW lobes, where we take into account $E(N-2,L)$ and $E(N+2,L)$ and perform the quadratic interpolation]. The resulting phase diagram can be seen in Fig. 7. We remark that apart from the conventional $|0(2\rho)0(2\rho)0\cdots\rangle$ DW phases, with $\rho = \rho_{\rm DW}$, we observe $|0(2\rho - \frac{1}{2})0(2\rho + \frac{1}{2})\cdots\rangle$ phases for odd $n_{\rm DW}$ as an effect of introducing $V_{\rm nnn} n_i n_{i+2}$ coupling terms into the Hamiltonian. The corresponding DW regions are, fortunately, quite tiny, showing that for most parameters, the picture obtained within the EBH model is correct.

Apart from the abundant DW phases we observe either SF- or SS-like phases, as indicated by the power-law decay of the $C_{\rm SF}$ correlations (9). The difference between the two phases is a nonzero density wave order parameter value in the supersolid phase. The trivial SF phase is seen for $\rho < 1$; however, we observe the emergence of a pair superfluid (PSF) phase for large enough μ. We use the pair-tunneling correlation

$$C_p = \frac{1}{L} \sum_i \langle b_i^\dagger b_i^\dagger b_{i+1} b_{i+1} \rangle \tag{10}$$

as a measure of pair superfluidity (see Fig. 7). The phases marked SS and PSS (pair supersolid) in Fig. 7 differ from conventional supersolid phases in a simple EBH model, where $C_{\rm SF}(r)$ is always positive. $C_{\rm SF}(r)$ is negative for $r = 4n + 2$, $n \in \mathbb{Z}$ in the SS phase [Fig. 8(a)] and for odd r in the PSS phase [Fig. 8(b)]. The other difference is that $C_p > 0$ in the PSS phase. We remark that both the PSS and PSF phases have been previously observed in numerical calculations for EBH Hamiltonians with density-dependent tunneling [32,57,58].

Next, we describe the last phase present in the phase diagram, which we call an incommensurate pair supersolid

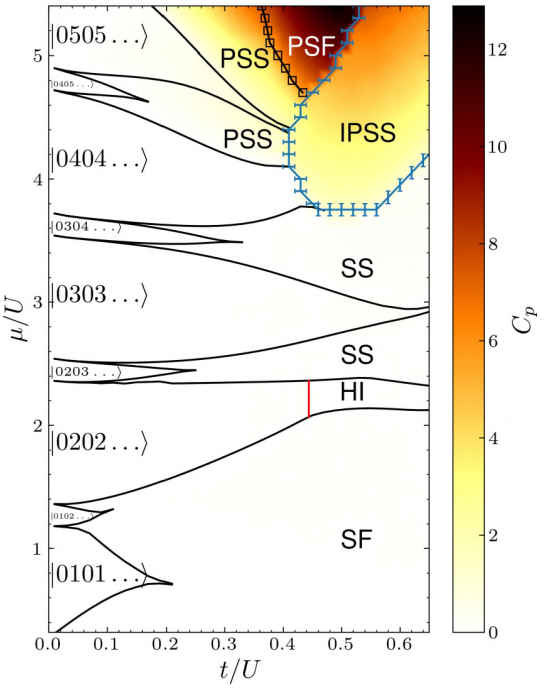

FIG. 7. The phases for the system for $d = 0.1$ at a fixed ratio $V/U = 0.75$. Black lines showing the boundaries of DW phases are the values of μ_+ and μ_- obtained from OBC DMRG ($L = 200$). The black squares come from sine-square deformation (SSD) DMRG (see Appendix C for details) for $L = 100$ and show the transition points between PSS and PSF (where $\mathcal{O}_{\rm DW}$ vanishes). Blue error bars mark the boundaries of the IPSS phase (and also SSD DMRG, $L = 100$). The value of pair-tunneling correlations C_p (10) is plotted as a color map with the scale shown on the right.

(IPSS). This phase is characterized by a finite, positive C_p and the structure factor

$$S(q) = \frac{1}{L^2} \sum_{j,k=1}^{L} \langle n_j n_k \rangle \, e^{-iq(j-k)}, \tag{11}$$

with a peak at $\pi/2 < q < \pi$, which is incommensurate with respect to lattice size and the particle density. In order to identify this phase, we use the sine-squared deformation (SSD) variant of the DMRG method which we describe in Appendix C.

In the IPSS we see periodic modulation of both density and density-density correlations [Fig. 9(a)] in the form of

$$\langle n_i \rangle = \rho_{\rm bulk} + \Delta\rho \sin(q_{\langle nn \rangle} i + \varphi_0), \tag{12}$$

$$\langle n_i n_{i+r} \rangle = C_1 + A_1 \sin(q_{\langle nn \rangle} r + \varphi_1) r^{-\alpha_1}, \tag{13}$$

where $q_{\langle nn \rangle}$ is the same wave-number value for which there is a peak in $S(q)$ [see Fig. 9(c)] The pair correlations also show the same modulation, while at the same time following a power-law decay [Fig. 9(b)],

$$\langle b_i^\dagger b_i^\dagger b_{i+r} b_{i+r} \rangle = [C_2 + A_2 \sin(q_{\langle nn \rangle} r + \varphi_2)] r^{-\alpha_2}. \tag{14}$$

Another modulation can be observed in $\langle b_i^\dagger b_{i+r} \rangle$; however, in this case the wave number differs from $q_{\langle nn \rangle}$, and the values

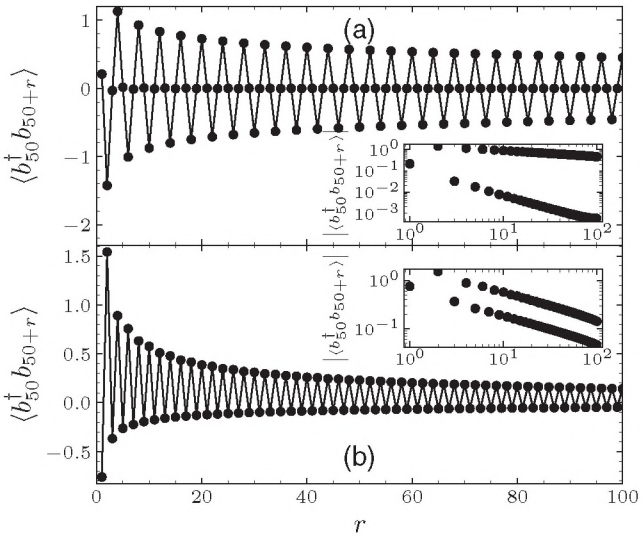

FIG. 8. OBC DMRG results of $\langle b_i^\dagger b_{i+r}\rangle$ correlations in the middle of an $L = 200$ lattice at (a) $\rho = 1.25$, $t/U = 0.59$ (SS phase) and (b) $\rho = 2.25$, $t/U = 0.37$ (PSS phase). Log-log plots of the same correlations are shown in the insets.

oscillate around zero [see Fig. 9(d)]:

$$\langle b_i^\dagger b_{i+r}\rangle = A_3 \sin(q_{\langle b^\dagger b\rangle} r + \varphi_3) r^{-\alpha_3}. \tag{15}$$

After combining the results for many different μ and t/U parameters, we can provide the relation between $q_{\langle b^\dagger b\rangle}$ and $q_{\langle nn\rangle}$ [see Fig. 10(a)]:

$$q_{\langle b^\dagger b\rangle} = \pi - 0.5 q_{\langle nn\rangle}. \tag{16}$$

We also note that is $q_{\langle nn\rangle}$ does not depend exclusively on ρ_{bulk} [which is the case in, e.g., underdoped $\rho = 0.5$ DW, where $q = 2\pi\rho$ [26]; see Fig. 10(b)].

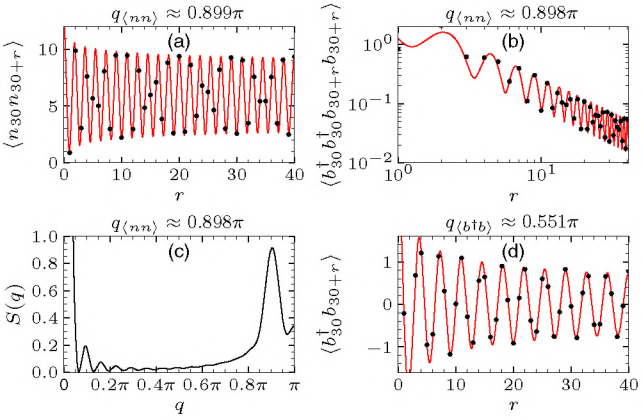

FIG. 9. Correlations and structure factor values obtained with SSD DMRG for the system in the IPSS phase ($L = 100$, $t/U = 0.48$, and $\mu = 3.7$). (a) Density correlations, (b) pair correlations, (c) structure factor (11), and (d) creation-annihilation correlations. For (a), (b), and (d), black points mark the numerical results, with red lines showing the fits of the functions in Eqs. (13) to (15). The value of the appropriate wave number q_α obtained from the fits [or from the position of the $S(q)$ peak in (c)] is written above each plot.

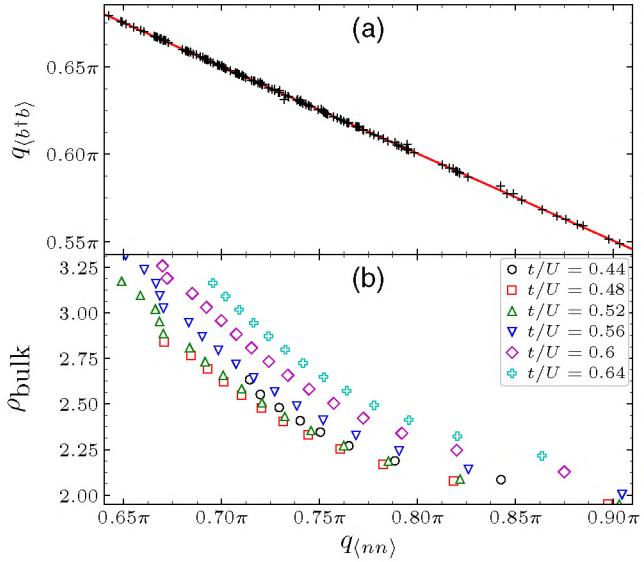

FIG. 10. The results of SSD DMRG for the IPSS phase. (a) The relation between $q_{\langle nn\rangle}$ and $q_{\langle b^\dagger b\rangle}$. The linear fit (red) is $q_{\langle b^\dagger b\rangle} = 0.9991(6)\pi - 0.4984(7) q_{\langle nn\rangle}$. (b) The relation between $q_{\langle nn\rangle}$ and ρ_{bulk} shown for different values of t/U.

V. CONCLUSIONS

In this paper we have presented an accurate Hamiltonian representation of a one-dimensional system of bosons in an optical lattice considering both the dipolar and contact interactions (the mutual strength of which may be balanced using the Feshbach resonance). We have employed the well-established DMRG method to measure the dependence of the phase transitions on often overlooked terms in the EBH model (most notably, the next-nearest-neighbor tunnelings and the density-dependent tunnelings). We have observed the suppression of the SF phase with rising dipolar interaction strength. In the case of fixed $\rho = 1$ we have also noted the stable presence of a nontrivial, highly nonlocally correlated HI phase throughout the considered parameters range, which is even more pronounced for realistic, low values of dipolar interactions. This robustness can be traced back to the fact that HI is a symmetry-protected topological state [59].

For greater dipolar interaction strength and higher densities we have observed interesting pair-correlated phases. Among those, we put a particular emphasis on characterizing a novel incommensurate pair superfluid phase, whose distinctive feature is an incommensurate density wave order. That phase is not present either in the standard EBH model or for large dipole-dipole interactions in small-diagonalization studies. We have also noticed a particular relation between wave numbers characterizing different correlations measured in this phase (16) which may provide some insight into how to construct an appropriate theoretical description. Rigorous theoretical treatment of the IPSS is, however, beyond the scope of this paper.

ACKNOWLEDGMENTS

This work was realized under National Science Centre (Poland) Projects No. 2015/19/B/ST2/01028 (K.B.), No.

2016/23/D/ST2/00721 (M.Ł.), and No. 2016/21/B/ST2/01086 (J.Z.). It was also supported in part by PL-Grid Infrastructure as well as by the EU H2020 Future and Emerging Technologies project QUIC (Grant No. 641122).

APPENDIX A: THE DETERMINATION OF HAMILTONIAN PARAMETERS

The values of the parameters in model (1) have been calculated numerically using Wannier function representation for a periodic boundary system with a standard optical lattice potential $V_{\rm opt}(\mathbf{r})$. In the numerical calculations described below we assume the lattice is in the form of a cube with N^3 sites, so that the total volume $\Omega = (Na)^3$, where $a = \pi/k_L$ is the lattice constant.

Bloch functions of the form

$$\phi_{\mathbf{k}}(\mathbf{r}) = e^{i\mathbf{k}\cdot\mathbf{r}} u_k(\mathbf{r}), \tag{A1}$$

where $u_k(\mathbf{r})$ is a function with the same periodicity as the lattice potential, are calculated for the noninteracting Hamiltonian, $H_{\rm NI} = \frac{-\hbar^2\nabla^2}{2m} + V_{\rm opt}(\mathbf{r})$, as the lowest-energy eigenvectors of the Schrödinger equation:

$$H_{\rm NI}\phi_{\mathbf{k}}(\mathbf{r}) = E_k\phi_{\mathbf{k}}(\mathbf{r}). \tag{A2}$$

Wannier functions can be calculated in the usual way [41] from the Bloch functions:

$$w_n(\mathbf{r}) = \frac{1}{\sqrt{N^3}} \sum_{\mathbf{k}\in \rm BZ} \phi_{\mathbf{k}}(\mathbf{r}) e^{-ik_x an}, \tag{A3}$$

where $\phi_{\mathbf{k}}(0)$ is real and positive, n is the number of the lattice site in the x direction (we assume $y = z = 0$), and the summation is done over $\mathbf{k} = (k_x, k_y, k_z)$ from the first Brillouin zone.

Substituting field operators of the form $\phi(\mathbf{r}) = \sum_i w_i(\mathbf{r}) b_i$ in (2), we get

$$\begin{aligned} t &= t_{i(i+1)}, \\ t_{\rm nnn} &= t_{i(i+2)}, \\ U &= V_{iiii}, \\ V &= V_{i(i+1)i(i+1)} + V_{i(i+1)(i+1)i}, \\ V_{\rm nnn} &= V_{i(i+2)i(i+2)} + V_{i(i+2)(i+2)i}, \\ T &= -0.5[V_{ii(i+1)i} + V_{iii(i+1)}], \end{aligned} \tag{A4}$$

with

$$t_{ij} = -\int_\Omega d\mathbf{r} w_i^*(\mathbf{r}) H_{\rm NI}\, w_j(\mathbf{r}), \tag{A5}$$

$$\begin{aligned} V_{ijkl} = &\int_\Omega d\mathbf{r_1} d\mathbf{r_2} w_i^*(\mathbf{r_1}) w_j^*(\mathbf{r_2}) \\ &\times V(\mathbf{r_1} - \mathbf{r_2}) w_k(\mathbf{r_1}) w_l(\mathbf{r_2}). \end{aligned} \tag{A6}$$

Integral (A5) is straightforward to calculate using (A2) and (A3). In order to calculate (A6), we use periodic extension of the interaction potential:

$$V(\mathbf{r}) = \frac{1}{\Omega} \sum_{\mathbf{k}} \widetilde{V}(\mathbf{k}) e^{i\mathbf{k}\cdot\mathbf{r}}, \tag{A7}$$

where $\mathbf{k} = \frac{2\pi}{Na}(n_1, n_2, n_3)$, $n_i \in \mathbb{N}$, and $\widetilde{V}(\mathbf{k}) = \widetilde{V}_c(\mathbf{k}) + \widetilde{V}_d(\mathbf{k})$ is the sum of the Fourier transforms of the contact and dipolar interaction potentials (3):

$$\widetilde{V}_c(\mathbf{k}) = \frac{4\pi\hbar^2 a_s}{m}, \quad \widetilde{V}_d(\mathbf{k}) = C_{dd}(\cos^2\gamma - 1/3), \tag{A8}$$

where γ is the angle between the direction of polarization and $\mathbf{k}$. For convenience, we group the Wannier functions with the same arguments $w_{ij}(\mathbf{r}) = w_i^*(\mathbf{r}) w_j(\mathbf{r})$:

$$\begin{aligned} V_{ijkl} &= \int_\Omega d\mathbf{r_1} w_{ik}(\mathbf{r_1}) \int_\Omega d\mathbf{r_2} V(\mathbf{r_1} - \mathbf{r_2}) w_{jl}(\mathbf{r_2}) \\ &= \int_\Omega d\mathbf{r_1} w_{ik}(\mathbf{r_1}) (V * w_{jl})(\mathbf{r_1}) \\ &= \frac{1}{\Omega} \int_\Omega d\mathbf{r_1} w_{ik}(\mathbf{r_1}) \sum_{\mathbf{k_2}} \widetilde{(V * w_{jl})}(\mathbf{k_2}) e^{i\mathbf{k_2}\cdot\mathbf{r}}. \end{aligned} \tag{A9}$$

We use the convolution theorem for the Fourier series to obtain

$$\begin{aligned} V_{ijkl} &= \frac{1}{\Omega} \int_\Omega d\mathbf{r}\, w_{ik}(\mathbf{r}) \sum_{\mathbf{k_2}} \widetilde{V}(\mathbf{k_2}) \widetilde{w_{jl}}(\mathbf{k_2}) e^{i\mathbf{k_2}\cdot\mathbf{r}} \\ &= \frac{1}{\Omega^2} \int_\Omega d\mathbf{r} \sum_{\mathbf{k_1}} \widetilde{w_{ik}}(\mathbf{k_1}) e^{i\mathbf{k_1}\cdot\mathbf{r}} \sum_{\mathbf{k_2}} \widetilde{V}(\mathbf{k_2}) \widetilde{w_{jl}}(\mathbf{k_2}) e^{i\mathbf{k_2}\cdot\mathbf{r}} \\ &= \frac{1}{\Omega^2} \sum_{\mathbf{k_1},\mathbf{k_2}} \widetilde{w_{ik}}(\mathbf{k_1}) \widetilde{V}(\mathbf{k_2}) \widetilde{w_{jl}}(\mathbf{k_2}) \int_\Omega d\mathbf{r}\, e^{i(\mathbf{k_1}+\mathbf{k_2})\cdot\mathbf{r}} \\ &= \frac{1}{\Omega} \sum_{\mathbf{k}} \widetilde{w_{ik}}(-\mathbf{k}) \widetilde{V}(\mathbf{k}) \widetilde{w_{jl}}(\mathbf{k}). \end{aligned} \tag{A10}$$

APPENDIX B: DMRG PARAMETERS

All of the numerical calculations reported in this paper were done using density-matrix renormalization group (DMRG) implementation found in the ITENSOR library [23]. For most of the work OBCs were used, with sizes from $L = 100$ to $L = 400$ and a maximum bond dimension $\chi = 600$. The cutoff ϵ was set to 10^{-12} [ϵ determines the number of singular values discarded after each singular-value decomposition step in the ITENSOR algorithm: $(\sum_{n\in\text{discarded}} \lambda_n^2)/(\sum_n \lambda_n^2) < \epsilon$]. In Sec. III, we limit the maximum number of particles on each lattice site $N_{\rm cut}$ to 5, while for the OBCs and the SSD DMRG used in Sec. IV the number is, respectively, up to 10 and 12.

Unless stated otherwise, a boundary term equal to $2\rho(n_1 V + n_2 V_{\rm nnn} + n_L V_{\rm nnn})$ was added to break the degeneracy of the DW state (the added term simulates a situation where we have four additional sites at the boundaries, with fixed $n_{-1} = 0$, $n_0 = 2\rho$, $n_{L+1} = 0$, and $n_{L+2} = 2\rho$, as expected in one of the DW ground states). Another motivation for adding these terms is to remove excitations on the edges in the HI phase.

APPENDIX C: THE DESCRIPTION OF SINE-SQUARED DEFORMATION DMRG

Some of the calculations (determination of boundaries of the IPSS phase in Sec. IV) were performed using a smooth-boundary DMRG method, referred to as a sine-squared deformation (SSD) DMRG. In this approach the Hamiltonian

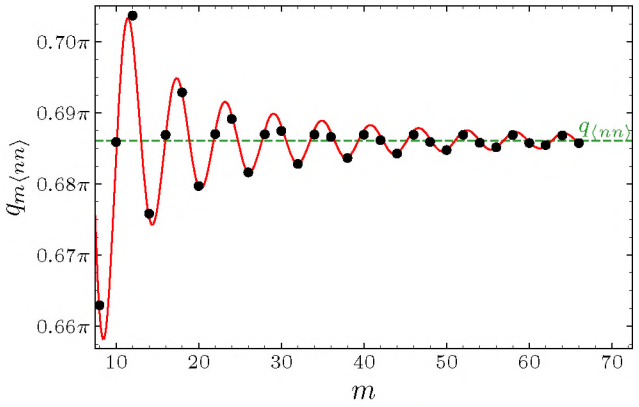

FIG. 11. Position of the peak in $S(q)$ (11) computed using m middle sites (black points). The red solid line shows a fit of the form $C + A\,m^{-B}\cos(Km + \phi)$. Here $K \approx 0.342\pi$, which is roughly half of $q_{\langle nn\rangle} = C \approx 0.686\pi$ (shown as a green dashed line). At most 2/3 of all lattice sites have been considered. Data are calculated for $\mu/U = 5.2$, $t/U = 0.6$, $L = 100$, and $N_{\text{cut}} = 12$. The damped oscillation amplitude $S(q)$ position is approximately an order of magnitude smaller than the FWHM of the $S(q)$ function, which for maximal m is $\approx 0.03\pi$.

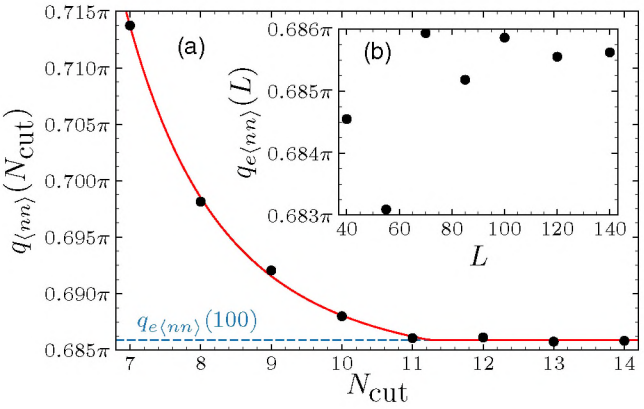

FIG. 12. (a) Position of the $S(q)$ peak $q_{\langle nn\rangle}$ (see Fig. 11) calculated for different values of maximum particles per site cutoff N_{cut} for $L = 100$. The red solid line shows a power-law decay to a constant value $q_{e\langle nn\rangle}$ (reached for a finite N_{cut}, here approximately 11.24; shown as a blue dashed line). (b) Values of $q_{e\langle nn\rangle}$ calculated for different system sizes L. Data for (a) and (b) were calculated for $\mu/U = 5.2$ and $t/U = 0.6$. The position of the $S(q)$ peak for $N_{\text{cut}} \geqslant 10$ $S(q)$ and for $L \geqslant 40$ changes by at least one order of magnitude less than the corresponding FWHM.

is rescaled using a sine-squared deformation [60]: $H_{\text{SDD}} = \sum_{j=0}^{2}\sum_{i=1}^{L-j} f_{i,j}\,H_{i,i+j}$, where

$$f_{i,j} = \sin^2\left[\frac{\pi}{L}\left(i + \frac{j-1}{2}\right)\right], \tag{C1}$$

with $H_{i,i+j}$ acting only on sites i and $i+j$ and $H_{i,i} \equiv H_i$ acting only on a single site, i. We also add a chemical potential term to the Hamiltonian, so that now $H_i = (U/2)n_i(n_i - 1) - \mu n_i$.

In contrast to regular DMRG methods, the density of the gas of particles (as measured in the middle part of the lattice) is not fixed by the number of particles N used in the simulation, but rather by the value of μ. An excess (or a deficit) of particles stemming from the choice of N is taken care of by placing extra particles (vacancies) close to the system boundary, where the coefficient $f_{i,j}$ takes a minimal value. This makes the edges act as an effective bath for the particles (holes) in the middle of the lattice. Because of that, in determination of the physical quantities, we consider only 40% of the sites in the middle of the lattice, unless stated otherwise.

We pick N such that it does not differ much from $L\rho_{\text{bulk}}$, the number compatible with the bulk density. This ensures that fewer particles are displaced to (from) the edges, which minimizes the undesired boundary effects on the computed expectation values in the middle of the system.

In order to find the values of wave numbers $q_{\langle b^\dagger b\rangle}$ and $q_{\langle nn\rangle}$ [plotted in Fig. 10(a)] we look at the position of the peak of $S(q)$ (11) (or an analogical quantity for $\langle b^\dagger b\rangle$ correlations). To remove the boundary effects from our analysis, we consider only m lattice sites in the middle when calculating the structure factor. Depending on m, the position of the peak $q_{m\langle nn\rangle}$ oscillates with decreasing amplitude (see Fig. 11) around a value $q_{\langle nn\rangle}$, which is the one used in the main text.

As the mean densities in the IPSS phase in our calculations are quite high [with sites filled by more than six particles; Fig. 10(b)], we calculated how the cutoff on maximum particles per site N_{cut} in DMRG calculations affects the obtained value of $q_{\langle nn\rangle}$ [Fig. 12(a)], taking as an example values of $\mu/U = 5.2$ and $t/U = 0.6$, corresponding to $\rho_{\text{bulk}} \approx 3.1$. For each system size L we define $q_{e\langle nn\rangle}(L) = \lim_{N_{\text{cut}}\to\infty} q_{\langle nn\rangle}(N_{\text{cut}})$ and plot its value in Fig. 12(b). We determine that $N_{\text{cut}} = 12$ and $L = 100$ are enough to get converged values of wave numbers, and these parameters were used for SSD DMRG calculations.

[1] D. Jaksch, C. Bruder, J. I. Cirac, C. W. Gardiner, and P. Zoller, Phys. Rev. Lett. **81**, 3108 (1998).
[2] M. Greiner, O. Mandel, T. Esslinger, T. W. Hänsch, and I. Bloch, Nature (London) **415**, 39 (2002).
[3] C. Chin, R. Grimm, P. Julienne, and E. Tiesinga, Rev. Mod. Phys. **82**, 1225 (2010).
[4] A. Frisch, M. Mark, K. Aikawa, S. Baier, R. Grimm, A. Petrov, S. Kotochigova, G. Quéméner, M. Lepers, O. Dulieu, and F. Ferlaino, Phys. Rev. Lett. **115**, 203201 (2015).
[5] E. G. Dalla Torre, E. Berg, and E. Altman, Phys. Rev. Lett. **97**, 260401 (2006).
[6] S. Sinha and L. Santos, Phys. Rev. Lett. **99**, 140406 (2007).
[7] T. Lahaye, C. Menotti, L. Santos, M. Lewenstein, and T. Pfau, Rep. Prog. Phys. **72**, 126401 (2009).
[8] J. Ruhman, E. G. Dalla Torre, S. D. Huber, and E. Altman, Phys. Rev. B **85**, 125121 (2012).
[9] M. A. Baranov, M. Dalmonte, G. Pupillo, and P. Zoller, Chem. Rev. **112**, 5012 (2012).

[10] M. Wall and L. Carr, New J. Phys. **15**, 123005 (2013).
[11] A. Gallemí, M. Guilleumas, R. Mayol, and A. Sanpera, Phys. Rev. A **88**, 063645 (2013).
[12] S. Gammelmark and N. T. Zinner, Phys. Rev. B **88**, 245135 (2013).
[13] O. Dutta, M. Gajda, P. Hauke, M. Lewenstein, D.-S. Lühmann, B. A. Malomed, T. Sowiński, and J. Zakrzewski, Rep. Prog. Phys. **78**, 066001 (2015).
[14] A. Gallemí, G. Queraltó, M. Guilleumas, R. Mayol, and A. Sanpera, Phys. Rev. A **94**, 063626 (2016).
[15] K. Kawaki, Y. Kuno, and I. Ichinose, Phys. Rev. B **95**, 195101 (2017).
[16] F. Cartarius, A. Minguzzi, and G. Morigi, Phys. Rev. A **95**, 063603 (2017).
[17] S. Baier, M. J. Mark, D. Petter, K. Aikawa, L. Chomaz, Z. Cai, M. Baranov, P. Zoller, and F. Ferlaino, Science **352**, 201 (2016).
[18] D. Delande and J. Zakrzewski, Phys. Rev. Lett. **102**, 085301 (2009).
[19] A. L. Gaunt, T. F. Schmidutz, I. Gotlibovych, R. P. Smith, and Z. Hadzibabic, Phys. Rev. Lett. **110**, 200406 (2013).
[20] M. Łącki, H. Pichler, A. Sterdyniak, A. Lyras, V. E. Lembessis, O. Al-Dossary, J. C. Budich, and P. Zoller, Phys. Rev. A **93**, 013604 (2016).
[21] H. Kim, G. Zhu, J. V. Porto, and M. Hafezi, arXiv:1805.01483.
[22] U. Schollwöck, Ann. Phys. (NY) **326**, 96 (2011).
[23] ITENSOR library, http://itensor.org.
[24] D. Rossini and R. Fazio, New J. Phys. **14**, 065012 (2012).
[25] G. G. Batrouni, V. G. Rousseau, R. T. Scalettar, and B. Grémaud, Phys. Rev. B **90**, 205123 (2014).
[26] B. Grémaud and G. G. Batrouni, Phys. Rev. B **93**, 035108 (2016).
[27] E. Wikberg, J. Larson, E. J. Bergholtz, and A. Karlhede, Phys. Rev. A **85**, 033607 (2012).
[28] T. Đurić, K. Biedroń, and J. Zakrzewski, Phys. Rev. B **95**, 085102 (2017).
[29] M. Lu, N. Q. Burdick, S. H. Youn, and B. L. Lev, Phys. Rev. Lett. **107**, 190401 (2011).
[30] K. Aikawa, A. Frisch, M. Mark, S. Baier, A. Rietzler, R. Grimm, and F. Ferlaino, Phys. Rev. Lett. **108**, 210401 (2012).
[31] A. Chotia, B. Neyenhuis, S. A. Moses, B. Yan, J. P. Covey, M. Foss-Feig, A. M. Rey, D. S. Jin, and J. Ye, Phys. Rev. Lett. **108**, 080405 (2012).
[32] T. Sowiński, O. Dutta, P. Hauke, L. Tagliacozzo, and M. Lewenstein, Phys. Rev. Lett. **108**, 115301 (2012).
[33] S. A. Moses, J. P. Covey, M. T. Miecnikowski, B. Yan, B. Gadway, J. Ye, and D. S. Jin, Science **350**, 659 (2015).
[34] S. A. Moses, J. P. Covey, M. T. Miecnikowski, D. S. Jin, and J. Ye, Nat. Phys. **13**, 13 (2017).
[35] P. Sengupta, L. P. Pryadko, F. Alet, M. Troyer, and G. Schmid, Phys. Rev. Lett. **94**, 207202 (2005).
[36] G. G. Batrouni, F. Hébert, and R. T. Scalettar, Phys. Rev. Lett. **97**, 087209 (2006).
[37] T. Mishra, R. V. Pai, S. Ramanan, M. S. Luthra, and B. P. Das, Phys. Rev. A **80**, 043614 (2009).
[38] B. Capogrosso-Sansone, C. Trefzger, M. Lewenstein, P. Zoller, and G. Pupillo, Phys. Rev. Lett. **104**, 125301 (2010).
[39] M. P. Zaletel, S. A. Parameswaran, A. Rüegg, and E. Altman, Phys. Rev. B **89**, 155142 (2014).
[40] M. Lewenstein, A. Sanpera, and V. Ahufinger, *Ultracold Atoms in Optical Lattices: Simulating Quantum Many-Body Systems* (Oxford University Press, Oxford, 2012).
[41] W. Kohn, Phys. Rev. **115**, 809 (1959).
[42] M. Łącki and J. Zakrzewski, Phys. Rev. Lett. **110**, 065301 (2013).
[43] H. Pichler, J. Schachenmayer, A. J. Daley, and P. Zoller, Phys. Rev. A **87**, 033606 (2013).
[44] M. Maik, P. Hauke, O. Dutta, M. Lewenstein, and J. Zakrzewski, New J. Phys. **15**, 113041 (2013).
[45] D.-S. Lühmann, O. Jürgensen, and K. Sengstock, New J. Phys. **14**, 033021 (2012).
[46] U. Bissbort, F. Deuretzbacher, and W. Hofstetter, Phys. Rev. A **86**, 023617 (2012).
[47] M. Łącki, D. Delande, and J. Zakrzewski, New J. Phys. **15**, 013062 (2013).
[48] C. Kollath, G. Roux, G. Biroli, and A. M. Läuchli, J. Stat. Mech. (2010) P08011.
[49] S. Trotzky, Y.-A. Chen, A. Flesch, I. P. McCulloch, U. Schollwöck, J. Eisert, and I. Bloch, Nat. Phys. **8**, 325 (2012).
[50] K. Góral, L. Santos, and M. Lewenstein, Phys. Rev. Lett. **88**, 170406 (2002).
[51] T. Salger, C. Geckeler, S. Kling, and M. Weitz, Phys. Rev. Lett. **99**, 190405 (2007).
[52] W. Yi, A. J. Daley, G. Pupillo, and P. Zoller, New J. Phys. **10**, 073015 (2008).
[53] Q. Sun, J. Evers, M. Kiffner, and M. S. Zubairy, Phys. Rev. A **83**, 053412 (2011).
[54] S. Nascimbene, N. Goldman, N. R. Cooper, and J. Dalibard, Phys. Rev. Lett. **115**, 140401 (2015).
[55] T. Giamarchi, *Quantum Physics in One Dimension*, International Series of Monographs on Physics, Vol. 121 (Oxford University Press, Oxford, 2004).
[56] T. D. Kühner, S. R. White, and H. Monien, Phys. Rev. B **61**, 12474 (2000).
[57] H.-C. Jiang, L. Fu, and C. Xu, Phys. Rev. B **86**, 045129 (2012).
[58] A. Rapp, X. Deng, and L. Santos, Phys. Rev. Lett. **109**, 203005 (2012).
[59] K. Wierschem and P. Sengupta, Mod. Phys. Lett. B **28**, 1430017 (2014).
[60] T. Hikihara and T. Nishino, Phys. Rev. B **83**, 060414 (2011).